Computation-accelerated Design of Dendrite-free Li Batteries

by

Karnpiwat Tantratian

A dissertation submitted in partial fulfillment
of the requirements for the degree of
Doctor of Philosophy
(Mechanical Sciences and Engineering)
in the University of Michigan-Dearborn
2023

Doctoral Committee:

Assistant Professor Lei Chen, Chair
Elisa Harrison, Seagate Technology
Assistant Professor Youngki Kim
Associate Professor Xuan Zhou
Professor Oleg Zikanov

Karnpiwat Tantratian

karntan@umich.edu

ORCID iD: 0000-0003-3916-1998

Dedication

To Tantratian's family

Acknowledgements

I cannot thank Prof. Lei Chen enough for his tireless support throughout my PhD education. I am grateful to all committee members for their guidance and feedback during my dissertation process. I would like to extend my gratitude to my parents for their unwavering spiritual support and understanding. Thank you to all my colleagues who have been with me throughout graduate school for their kindness. Thank you to all my friends who made my time in Michigan an unforgettable experience. Thanks Atta and Donut for helping me with the dissertation format.

Table of Contents

List of Tables

List of Figures

Abstract

The main obstacle to the development of the next-generation Li-based batteries is the formation of Li dendrite on the anode surface. Li dendrite growth contributes to the reduction of coulombic efficiency, poor cycling performance, and internal short circuits. To effectively tackle the Li dendrite issue, the underlying mechanism of how Li dendrite grows in a specific environment must be properly understood. In this dissertation, a mechano-electro-chemical phase-field model is extended to predict the evolution of Li dendrite, under influences of electric fields, Li-ion distributions, as well as mechanical stresses. The model is then utilized to simulate Li dendrite growth under 3 well-known Li dendrite suppression strategies: (i) 3D host structure for anode materials, (ii) solid electrolyte, and (iii) artificial solid electrolyte interface (or the coating layer). The fundamental mechanism of how each suppression technique regulates Li dendrite growth behavior and the suggestion on material designs for each approach are discussed.

Chapter 1: Introduction

Nowadays, the global temperature is rising each year due to greenhouse gas emissions from increased consumption of fossil fuels. To combat global warming and climate change, the world must soon transition to a green energy era. The key technologies that enable such transition is electric energy storage (EES). EES allows electricity generated from intermittent renewable energy, such as solar and wind energy, to be stored and used later when needed [1]. In addition, EES facilitates the shift towards electric vehicles (EV), which would significantly reduce the use of fossil fuels. In the U.S., it is reported that 29% of greenhouse gas emissions in 2019 came from only transportation, which holds the largest share among other sources [2]. The sooner the EV revolution starts, the more livable our planet becomes. Therefore, the research area of EES, such as batteries, has received much attention from scientists globally.

The requirements for EV batteries are much more stringent than for consumers electronics [3]. For example, EV batteries must possess a high specific capacitance for a long driving range, high specific power for fast charging, extreme-temperature tolerance as well as reasonable cost and safety [3]. In 2020, United States Advanced Battery Consortium (USABC) set a target specific energy of 350 Wh/kg for EV battery cells, which equates to a driving range of 500 km, or 300 miles [4]. However, the current state-of-the-art Li-ion battery technology, with its highest reported specific energy ranging from 200 to 300 Wh/kg, falls short of meeting this requirement. Therefore, research to improve battery performance must continue.

1.1 Lithium (Li)-based Battery

A battery stores electric energy in a chemical form, and then converts the stored chemical energy back to electrical energy when needed. Rechargeable Li-based batteries are mainly composed of five components [5]:

(1) Anode: A negative electrode that oxidizes Li and releases electrons when discharging, reduces Li-ion and collects electrons during charging. The common material used is graphite.

(2) Cathode: A positive electrode that reduces Li-ion and absorbs electrons during discharging, oxidizes Li and receives electrons when charging. The common group of material used is Li transition metal oxide (LMO).

(3) Electrolyte: A medium between the electrodes that allows Li-ion transport but not electrons. The electrolytes can be an organic or inorganic liquid, as well as solid state.

(4) Separator: A barrier that physically keeps anode and cathode apart and chemically allows Li-ion diffusion but blocks electron transport.

(5) Solid electrolyte interface (SEI): A thin layer (in nanometer) naturally formed on the anode surface due to the initial reaction between reactive Li and the electrolyte. The geometry and property of the SEI play a major role in controlling the stability at the anode/electrolyte interface.

Based on a working mechanism, Li-based batteries can be categorized into two types (i) Li-ion batteries, (ii) Li metal batteries. Li-ion batteries store the energy through an intercalation reaction, which involves the insertion of Li into a compound with layered structure, such as graphite, as shown in Figure 1-1. This intercalation concepts results in excellent cyclability, making Li-ion batteries popular. However, the bulky graphite structure places a limit on the energy

content [6]. In contrast, Li metal batteries store the energy through Li electrodeposition/dissolution reaction on the Li metal anode surface. Without a host structure, the battery cells become lighter and smaller, but with poor cyclability and safety [6].

Nevertheless, both batteries technologies suffer from the possibility of non-uniform Li plating, known as "Li dendrite," which interferes with battery safety and cyclic performance. For Li-ion batteries, unwanted Li plating reactions can occur on the graphite surface under some abusive conditions, such as overcharging. In the case of Li metal batteries, which rely on plating/stripping of reactive Li metal, even under normal operating conditions, Li dendrite problem is more severe.

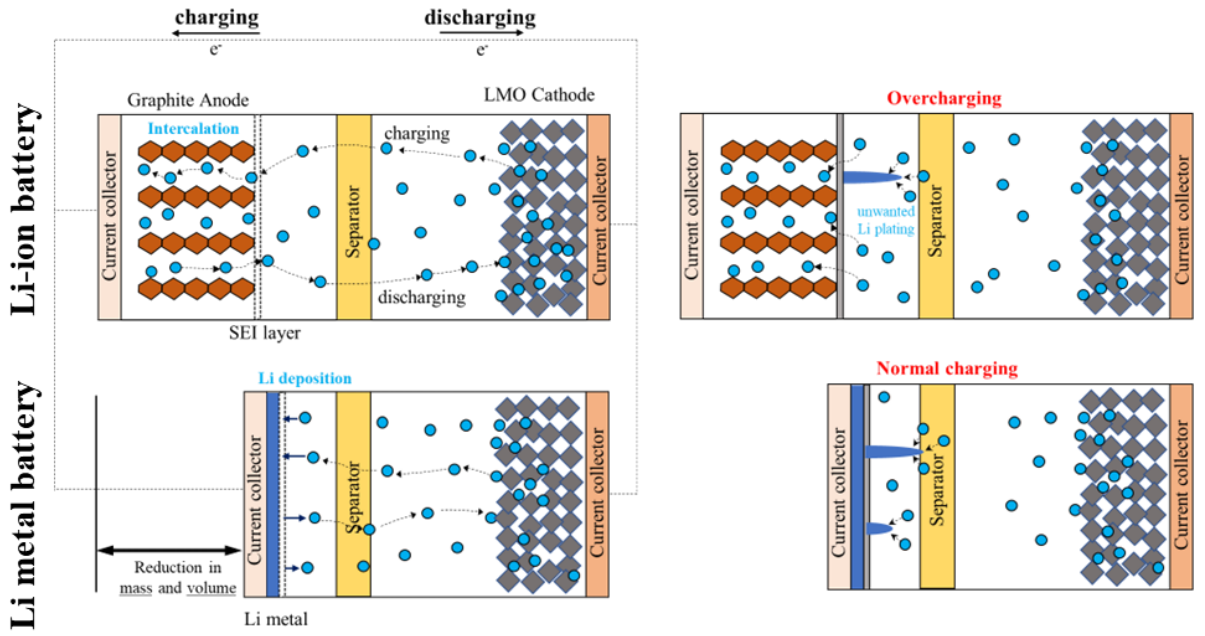

Figure 1-1 Comparison of typical Li-ion cell and Li metal cell. The progression from Li-ion intercalation to Li deposition mechanism results in the huge reduction in mass and volume due to the removal of the graphite structure; however, the Li dendrite issue exacerbates, and become critical.

1.2 Li Dendrite Formation

Among the causes of battery incidents, the failure of Samsung Galaxy Note 7 in 2016 is a notable example, where Li dendrite has been reported as one of the primary causes [7], [8]. Another instance of potential dendrite-related battery fire incidents is the recall of Chevrolet Bolt electric vehicles. In 2021, 16 confirmed cases of electric vehicles fires were reported, leading to the recall of all Chevrolet Bolt models, including the 2022 one, at a cost of approximately $2 billion to General Motors [9]. It is worth to note that these incidents were related to Li-ion battery technology. However, the Li dendrite problem is even more severe in Li metal batteries, rendering them far from commercialization. Major problems related to Li dendrite include internal short circuit and the reduction in energy efficiency [10].

1. Internal short circuit – Once the Li dendrite penetrates the separator and reaches the cathode, it creates a short circuit (Figure 1-2). This results in a rapid flow of internal current between electrodes, releasing a large amount of heat and energy, accelerating the decomposition of flammable electrolyte and eventually triggering thermal runaway [10].
2. Reduced energy efficiency – The formation of Li dendrite increases the surface area of metallic Li that can react with the electrolyte, causing the irreversible parasitic reaction that consumes the active Li and electrolyte, reducing coulombic efficiency as well as life cycle. Moreover, during stripping, the isolation of Li metal from the bulk anode, known as inactive or "dead Li" is possible, further decreasing the coulombic efficiency (Figure 2). Furthermore, the unfavorable porous nature of Li dendrite and dead Li, blocks the pathways of Li-ions to the active anode surface, increasing the internal resistance, inducing a large polarization, compromising the energy. Addressing the Li

dendrite problem is a crucial part in enabling a safer and better battery. However, to overcome this challenge is not straightforward because the physics inside the battery is very complicated [10].

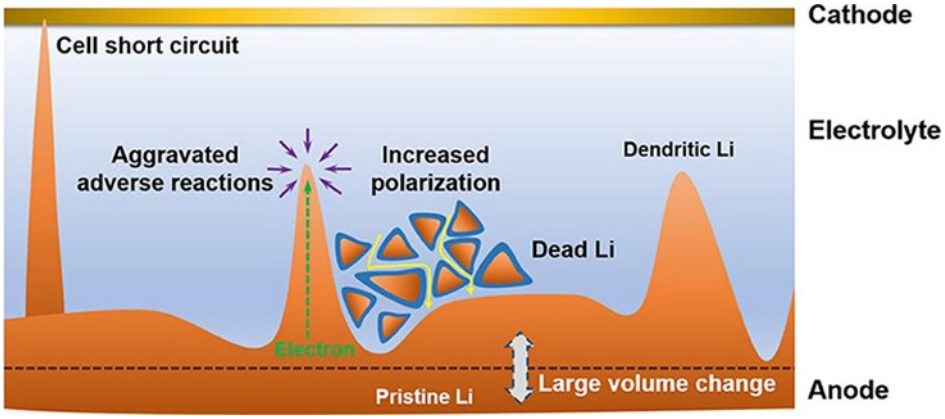

Figure 1-2. Schematic of Li dendrite problems in Li metal batteries, obtained from [10].

1.3 Motivation

To effectively address the issue of Li dendrite growth, it is essential to understand its fundamental mechanism. It is experimentally determined that the Li deposition behavior depends on several factors, such as chemical reactions, charge transfer reaction, mass transport, temperature, charge distribution, surface stress as well as the interaction between the deposited Li and the SEI layer. Despite decades of research, the mechanism of Li dendrite growth remains unclear.

Real-time information during battery operation is critical to obtaining an in-depth understanding of the Li dendrite behavior. *In situ/operando* characterization techniques, which can trace the morphological changes of the Li dendrite and associated chemical reactions, offer a valuable tool to comprehend the complex physical and electrochemical processes inside the cell. However, developing a reliable *in-situ/operando* method is challenging as the battery cell is not typically transparent to both visible light and electrons, necessitating a special design of the

electrochemical cell or state-of-the-art probing equipment to overcome this issue. Despite providing some insights, those special designed cells are still far from real-life battery cells.

Computational materials science offers an alternative solution. The rapid development of theoretical models together with advancements in computing performance allow computer simulations to capture the fundamental physics inside the battery. Molecular dynamics (MD) can provide insights into the interatomic movement and bonding formation, enabling Li deposition to be simulated at the nanoscale. Monte Carlo (MC) simulations can predict electrodeposition behavior involving hundreds to thousands of Li atoms. However, the impact of Li dendrite growth on cell performance occurs at the microscale, and scales of these methods are too small to reveal the microscale mechanism of Li dendrite. The phase-field model, which offers simulation scales from micro to the continuum level, is more suitable for predicting and understanding Li dendrite growth behavior. The Li dendrite mechanism revealed through phase-field simulation could ultimately guide the design of a safer and better battery.

1.4 Objective

This research aims to extend the existing electrochemical phase-field model for Li dendrite by incorporating the impact of mechanics. The newly developed model, known as the electro-chemo-mechanical phase-field model, will be used to predict and understand the Li dendrite growth behaviors under three mitigation strategies: (i) applying a 3D hosting structure, (ii) using a solid electrolyte (SE), and (iii) introducing an artificial SEI layer.

Chapter 2: Literature Review

This section aims to provide a concise overview of the proposed mechanisms of Li dendrite growth, which have been established through physics-based analytical models, experiments, and computational methods.

2.1 Mechanism of Li Dendrites

The existing fundamental models proposed to understand the Li dendrite mechanisms have been summarized. Although these models provide a solid foundation for understanding the Li dendrite mechanism, they are oversimplified and can only be used to evaluate the presence of Li dendrite at macroscale or suggest a design in general. However, they cannot capture the complex evolution of Li dendrites at a microscale in a real system, and thus Li dendrite have not yet successfully been addressed.

2.1.1 Spaced-charge Theory

Chazalviel's space-charge model states that, under polarization, the steady-state ionic concentration is disrupted: Li-ion and anions counterpart moves toward their counter electrodes, anode, and cathode, respectively. At the anode surface, once Li-ions are reduced into Li, the positive charges from Li-ion are instantly depleted near the electrode surface, creating a spaced-charge layer, inducing a large electric field, and thus leading to the nucleation and growth of Li

dendrite [11]. Therefore, it is reasonable to assume that the Li dendrite behavior is associated with the calculation of the Li-ion concentration gradient. By assuming dilute electrolyte solution, the concentration gradient $\frac{\partial c}{\partial x}$ is expressed as [12], [13],

$$\frac{\partial c}{\partial x}(x) = \frac{j\mu_a}{eD(\mu_a + \mu_{Li+})}, \tag{2-1}$$

where e represents the electronic charge, $\mu_a + \mu_{Li+}$ are anodic and Li-ion mobility, respectively. From Equation (2-1), one can determine the presence of Li dendrite for a symmetrical cell based on (i) the distance between electrode, L, (ii) the initial concentration, C_0, (iii) the ambipolar diffusion coefficient, D, and (iv) the current density, J. In the case that $\frac{\partial c}{\partial x} > \frac{2c_0}{L}$, the concentration gradient and potential remain constant, and thus theoretically, no dendrite formation. On the other hand, when $\frac{\partial c}{\partial x} > \frac{2c_0}{L}$, the ionic concentration decreases to zero at the electrode surface, initiating Li dendrite at a time τ, known as Sand's time, expressed as [12], [13],

$$\tau = \pi D \left(\frac{eC_o}{2jt_a}\right)^2, \tag{2-2}$$

where t_a is the anionic transference number. The longer the Sand's time, the longer the delay of Li dendrite formation. In addition, Chazalviel suggests that the speed of the dendrite growth is proportional to the rate at which anions withdraw from the deposits under the applied electric field: $v = -\mu_a E$.

According to the Sand's equation, some Li dendrite suppression strategies are suggested for example, (i) increasing the initial Li-ion concentration C_o, (ii) improving the transference

number of Li-ions t_a, (iii) reducing the applied current density j [14]. However, implementing those strategies, despite some progresses, have not completely solved the Li dendrite problem [14].

2.1.2 Mechanical Stress and Deformation Theory

Liquid electrolyte

Yamaki et al. [15] proposed that mechanical stress at the surface is the origin of Li dendrite growth. Li deposition under the SEI layer (or protective film) is subjected to mechanical stress due to the non-uniformity of the previously deposited Li layer. In order to release this stress, the protective film breaks, allowing whisker-like Li dendrite to grow. The relationship between pressure difference (ΔP) and surface tension (γ), can be expressed as,

$$\Delta P = \gamma\left(\frac{1}{r_1}+\frac{1}{r_2}\right), \tag{2-3}$$

where (r_1, r_2) is the orthogonal curvature radius. Based on this model, it is suggested that a hard film with surface tension higher than 0.2 N m^{-1} can mechanically suppress Li dendrite.

Recently, Wang et al. [16] proposed a new theory for Li dendrite growth based on stress. This theory states that compressive stress surface is induced during the Li deposition process. The formation of inorganic SEI layer, which is tightly bonded to the surface of Li metal, often prevents stress of being relieved, leading to the localized creep. This localized creep mechanically pushes Li filaments out of the surface. The theory suggests that Li dendrite will be initiated if the filament growth rate is larger than the rate of uniform plating ($v_{filament} > v_{plating}$). These growth rates can be mathematically expressed as,

$$v_{plating} = \frac{jV_{Li}}{F}, \tag{2-4}$$

$$v_{filament} = \frac{D_{Li}V_{Li}\sigma}{RTr}, \tag{2-5}$$

where j is the current density, V_{Li} is molar volume of Li, F is the Faraday's constant, D_{Li} is the effective Li diffusivity of the deposited Li, σ is the compressive stress, and r is the filament radius. The suggested design is to utilize a soft substrate to allow compressive stress relaxation during Li plating.

Solid electrolyte

To consider the interaction between Li metal and polymer electrolytes, Monroe and Newman [17] extended the surface tension theory by taking into account the elasticity of separator, deformation forces, compressive stresses, as well as electrochemical potential and current density at the surface perturbation. In their works, the famous Butler-Volmer equation was modified to explore the mechanical effects on the reaction current, expressed as

$$I = I_0 exp\left[\frac{(1-\alpha_a)\Delta\mu_e}{RT}\right]\left\{exp\left[\frac{\alpha_a F\eta}{RT}\right] - exp\left[\frac{\alpha_c F\eta}{RT}\right]\right\}, \tag{2-6}$$

where $\Delta\mu_e$ is the potential change due to the deformed surface caused by mechanical stress. When the current density at the deformed surface, referred to as "peak," is higher than that at the non-deformed surface, "valley," the surface roughness is amplified. A stability parameter is introduced,

$$\frac{\Delta\mu_e}{A\cos(\omega x)} \equiv \Delta\mu > 0. \tag{2-7}$$

However, when $\Delta\mu < 0$, the surface roughness is reduced, and a uniform surface Li deposition occurs. The critical value of $\Delta\mu$ (or when $\Delta\mu = 0$) is reached when the shear modulus

of the separator is equal to 1.8 times that of Li metal. This suggests that a polymer electrolyte with a shear modulus about twice that of Li metal could effectively suppress Li dendrites.

In contrast to Monroe and Newman model, which takes into account pre-stressed electrode conditions (initial tension on Li metal, while compression on the electrolyte), Barai et al. [18] studies a scenario without pre-stressed condition is excluded. Barai et al. proposed that Li deposition happens at the Li/electrolyte interface, pushing both the Li electrode and electrolytes backward, thereby inducing compressive stress to all components. Their results suggest that Li dendrite growth is mostly controlled by the current distribution, and mechanical forces have the potential to mitigate dendritic protrusions.

2.2 *In-situ/operando* Experimental Measurements

Imaging or monitoring different stages of the Li dendrite formation and growth can provide a comprehensive understanding of underlying physics behind the Li dendrite formation. Combining experimental observations with theoretical model, a solid understanding about Li dendrite mechanism could be established.

"*In-situ*," refers to studying the material in its original state or in a natural chemical environment, while "*operando,"* means studying the materials during their working conditions, such as observing the electrode materials during battery charging and discharging [19]. Exploring the relationship between electrode structures, cell designs and electrochemical performance under *operando* conditions can could lead to a clearer understanding about the Li dendrite mechanism

[19]. Figure 2-1 illustrates the rough configuration and design of different *in-situ/operando* imaging techniques used to study Li dendrite deposition, with respect to the spatial and temporal resolution of each technique. However, performing *in-situ/operando* characterization is challenging as it requires a special design of the electrochemical cells, integrated with probing equipment [19].

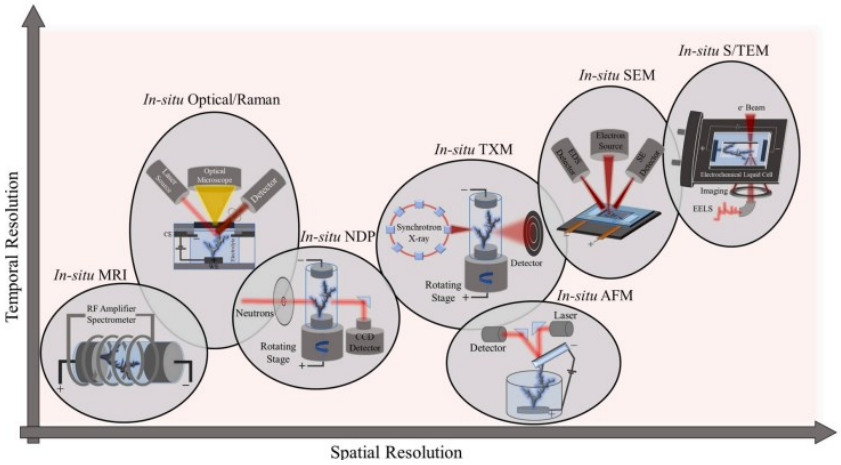

Figure 2-1. In-situ/operando imaging techniques with respect to their comparative spatial and temporal resolutions [19].

2.2.1 *In-situ/operando* Microscope

In-situ/operando optical imaging is the simplest way to study Li dendrite growth morphologies because it can be performed by using a glass vial. For example, Wood et al. [20] developed *in-situ* optical microscopy technique to study the relationship between the growth stages of Li dendrite with the cell voltage profile. As shown in Figure 2-2, their results provide detailed insight into the interplay between morphology and the dominant electrochemical processes occurring on the Li electrode surface. Moreover, *in-situ* optical microscopy was also used to

observed the formation of electrochemically insulating "dead Li," during the Li dissolution process [21]. In addition, Li dendrite growth and its resulting short-circuiting behavior can be detected and characterized through this method [22]. When a complete short circuit happens (Li dendrites connect two electrodes), the voltage drops to zero. However, a soft short-circuit (Li dendrites are regarded as contact fuses) results in a drop in voltage but not approaching to zero. The current passes through the small physically connected areas, rising temperature (Joule heating), which leads to the local melting of the short-circuited dendrite and connection breakage [22]. Furthermore, Bai et al. [23] observed the transition from mossy Li to dendritic growth to occur at the Sand's time, when Li-ion concentration at the electrode reduces to zero, supporting the hypothesis of diffusion limitation mechanism and also showed how effective the nanoporous separator can block the growth of the dendrite.

In sum, *In-situ/operando* optical microscope is the most convenient to study the Li dendrites evolution at scales that is relevant to practical battery operation. However, its spatial resolution is poor, limited by the wavelength of visible light (200 nm), and no analytical or quantitative information can be derived through this technique. Therefore, mechanism of Li dendrites cannot be fully revealed.

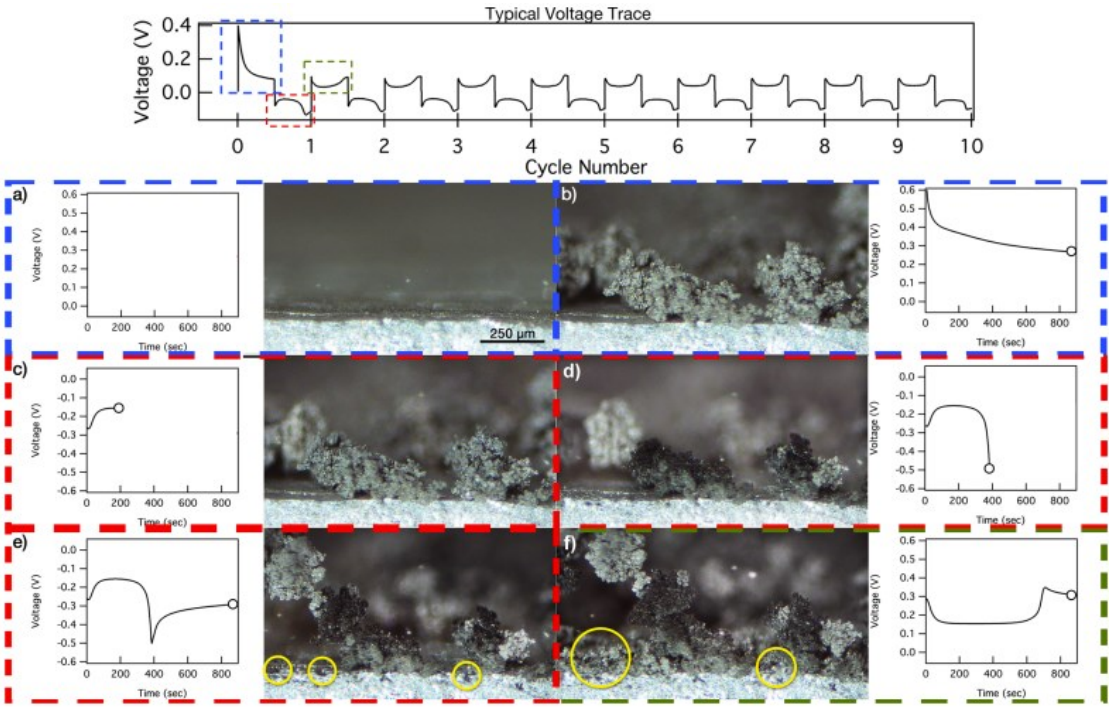

Figure 2-2. Observation of growth stages of Li dendrite and its corresponding cell voltage [20].

2.2.2 *In-situ/operando* Electron Microscope

In comparison to optical microscopy, electron microscopy has much higher spatial resolution, ranging from 2 to 10 nm for scanning electron microscopy (SEM) and 0.2 to 0.05 nm for transmission electron microscopy (TEM). This technique can be used to explore the Li dendrites evolution and the growth of SEI at early stages. For example, Mehdi et al. [24] used *In-situ/operando* TEM to investigate the nanoscale behavior of Li plating/stripping. The *In-situ* TEM setup is shown in Figure 2-3a, where the working electrodes, Platinum (Pt) rods, were immersed in 1 M $LiPF_6$ in PC electrolyte. The Li electrodeposition/dissolution process was predicted to occur near "hotspots," located at the tip. Figure 2-3b displays the images taken during Li plating/stripping cycles. Interestingly, "dead Li" around the electrode could be seen in the final

images in all three cycles [24]. The solid Li metal, SEI formation, and the electrolyte can be distinguished through dark-field imaging, where less dense materials appear brighter.

Despite high spatial resolution images and ability to detect the SEI formation behavior, electrons microscopic technique has several disadvantages, including significant beam damage, the need for an ultra-high vacuum environment and a complicated design for both liquid and solid electrolyte cells [19]. Most importantly, the designed electrochemical cell (Figure 2-3a**)** is very different from the actual battery cell. There is a long way to image the commercial batteries in *operando* conditions.

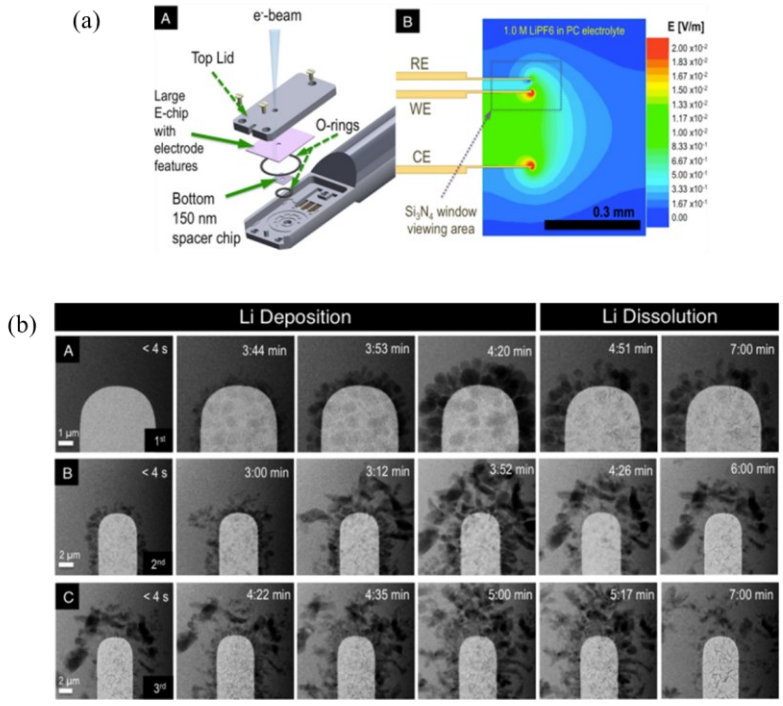

Figure 2-3. (a) Schematic illustrations of the In-situ/operando TEM settings (left), and finite element simulation of the electric field distribution in the nano-electrochemical cell (right). (b) images of Li deposition and dissolution at the interface between the Pt working electrode and the $LiPF_6$/PC electrolyte during the (A) first, (B) second, and (cC third charge/discharge cycles of the operando cell, obtained from [24].

2.3 Computational Investigation

Despite the use of advanced *in situ* characterization methods to study the dynamic behavior of Li dendrite growth, the full mechanism behind it has yet to be fully understood due to the limitations posed by the cell configuration, which differs significantly from that of a real battery system. Computer simulation can provide deeper insights into the mechanisms behind the growth of Li dendrite.

2.3.1 Molecular Dynamics Simulation

Molecular dynamics (MD) is a powerful simulation technique that has gained significant attention in the field of Li-based batteries. MD uses a mathematical model to simulate the interactions of individual atoms or molecules in a system, based on the laws of motion and intermolecular forces. By calculating the forces under various interaction potentials, MD allows researchers to gain a deeper understanding of the properties of assemblies of molecules [25]. Generally, MD simulation can be divided into 4 types: (1) classic molecular dynamics (CMD) under the Newtonian equation, (2) reactive molecular dynamics (RMD) under a reaction force field, (3) ab initio molecular dynamics (AIMD) under the Schrodinger equation and (4) coarse-grained molecular dynamics (CGMD) [25].

As an example, MD simulation has been used to prove the concept of self-heating-induced healing of Li dendrite mechanisms [26]. It was believed that the high current density was the cause of Li dendrite, but Li et al. [26] showed through the MD simulation that this was not the case. At

high rates, the amount of current passing through the electrode is large, leading to the accumulation of Joule heating at the electrode interface. The rise of temperature fundamentally enhances the diffusion of reduced Li atoms, which tends to smooth the surface. Figure 2-4 shows the MD simulation for the morphological change of Li dendrites after annealing at ~80°C for ~50 ps. For another instance, Aryanfar et al. [27] utilized ReaxFF MD to simulate Li dendrite growth under temperatures ranging from 317 to 357 K. Their results show that Li dendrite rapidly collapses at the beginning, but then a stabilized layer of 3-5 atoms thick is formed after 200 ps for most cases. This leads to the conclusion that temperature is not always harmful to Li metal batteries, but rather at the appropriate temperature, the growth of Li dendrite is suppressed. A fundamental mechanism can be revealed through the MD simulation, the length scale of MD simulation is in the nanoscale, which is smaller than the actual Li dendrite phenomenon that occurs at the microscale.

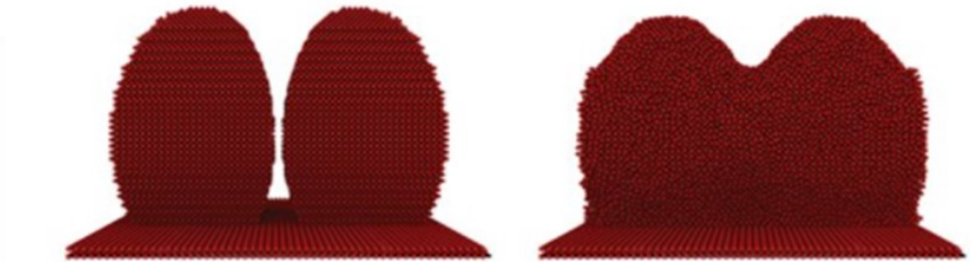

Figure 2-4. Screenshots of molecular models used in MD simulation, initial state (left) and after 50 ps at 80°C (right), obtained from [26].

2.3.2 Monte Carlo Simulation

Monte Carlo (MC) is one of most widely used computational tools, which employs a statistical technique in a random sampling manner to predict the motion of atomic particles due to

the physiochemical behavior. MC simulation can be utilized in Li electrodeposition applications [28]. It has the advantage of considering the movement of ions through diffusion and migration, atomic surface diffusion, and structural heterogeneities of the Li metal surface to predict Li dendrite behavior. However, the simulation scale is still too small to address the actual dendrite growth problem in reality. The important findings from MC simulation are summarized below.

MC simulation has been used to explore the impact of the electric field on the Li dendrite growth mechanism. Aryanfar et al. [28] showed that high-curvature dendrite tips significantly intensify the electric field, which accelerates the movement of Li ions toward the surface, thus promoting Li deposition on the dendrite tip, as illustrated in Figure 2-5. Pulse charging with an appropriate frequency range can be employed to suppress Li dendrites, as during pauses the electric field is generally reduced, alleviating the accumulation of the electric field at the dendrite tip.

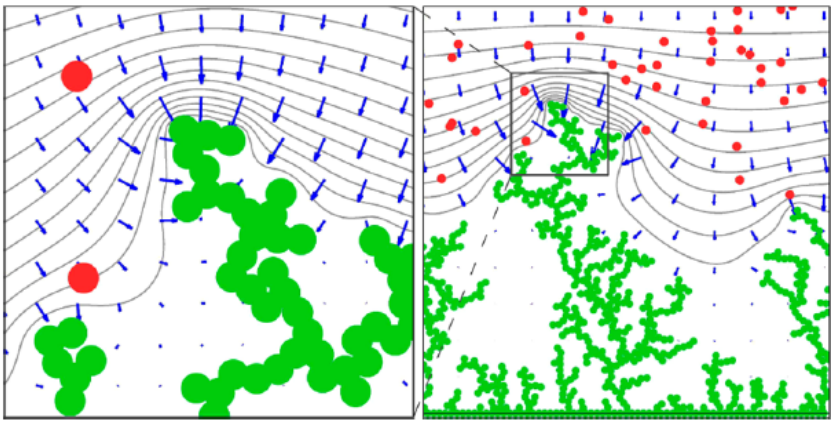

Figure 2-5. Zooming on the tip of Li dendrite showing intensified electric field that powerfully attracts Li-ion (left). Li dendrite structure with the simulation size scale of 16.7 nm x 16.7 nm (right) [29].

In addition, Aryanfar et al. [27], [30] extended their MC model to investigate the behavior of Li dendrites by considering temperature-dependent surface diffusion. The simulation reveals an

interesting finding that Li dendrite can be suppressed at high temperatures, which contradicts the common belief about the temperature effect on the Li dendrite mechanism. At high temperatures, Li-atom surface diffusion and Li-ion diffusion increases. However, the surface morphologies are likely controlled by the rate of Li-atom diffusion. This is because, Li-ion transport toward the electrode surface is strongly due to migration under the local electric field (not the Li-ion diffusion rate), which depends on the surface curvature. Thus, enhancing Li-atom diffusion not only directly decreases surface roughness, but further promotes the uniform Li-ions transport to the electrode surface. B. Sabarish et al. [31] recently showed similar findings that high temperature can help suppressing Li dendrite even at a high charging rate Figure 2-6. However, their results additionally indicate that both the Li-atom and Li-ion diffusion rates must be high to effectively suppress Li dendrite.

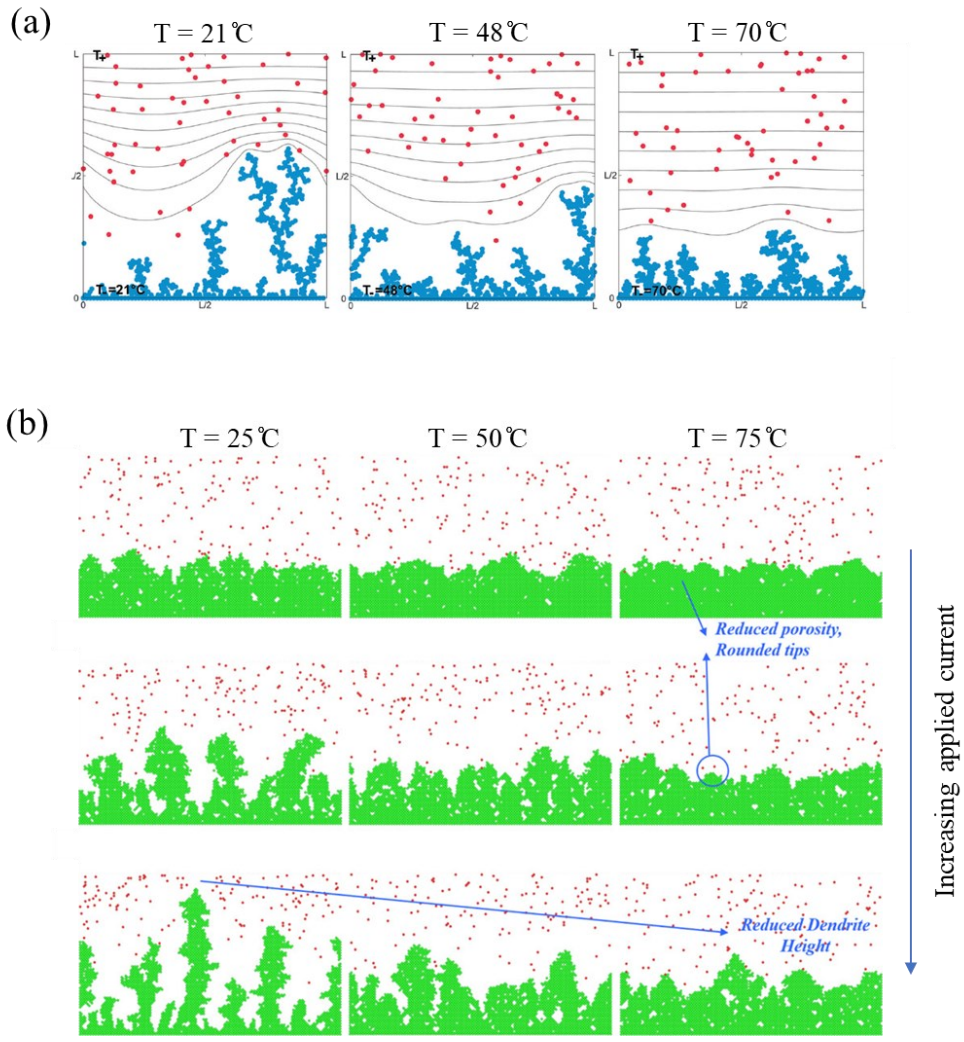

Figure 2-6. (a) MC simulation results, considering the temperature-dependent Li atom and Li-ion diffusion rate, retrieved from [30]. (b) MC simulation results showing Li electrodeposition behavior under different charging rate and operating temperature, obtained from [31].

2.3.3 Phase-field Simulation

The phase-field model offers a wider spatiotemporal span, from microscale to continuum framework, compared to the MD and MC simulations, making it suitable for predicting realistic Li dendrite behavior. Originally, the phase-field model has been used extensively to simulate microstructure evolutions such as solidification, solid phase transformation and grain growth.

Later, the model has been extended to predict the phase transformation due to electrodeposition. To model Li dendrite growth, the phase-field theory introduces a phase-field order parameter ξ, which describes two distinct phases: ξ equals 0 in the electrolyte phase and 1 in Li metal, while continuously varying from 0 to 1 in the diffused interface (electrode/electrolyte interface in this context). The dynamic phase evolution of Li dendrites with a moving diffused interface can be numerically solved using finite element or finite difference methods.

Guyer et al. [32] first attempted to model electrodeposition processes via the phase-field method in 1D. In Guyer's model, the Poisson equation is introduced to govern electrostatics; meanwhile, the electrode/electrolyte interface evolution is described by the Allen–Cahn kinetics equation, which employs a linear electrochemical reaction kinetics. Later, Liang et al. [33] proposed a nonlinear phase field model to predict the interface evolution that is far from the equilibrium state. The model assumes that the phase evolution exponentially varies with the electrochemical overpotential, which is depending on the electrostatic potential and ion concentration, resembling with the Butler–Volmer electrochemical reaction kinetics. Soon after, Chen et al. [34] extended this nonlinear phase-field model by introducing a current source term that describes the asymmetry of the charge generation and depletion at the electrode/electrolyte interface. Figure 2-7 shows the evolution of Li dendrite, Li-ion concentration, as well as the electric potential distribution. This nonlinear phase-field model provides a robust computation tool for Li dendrite studies.

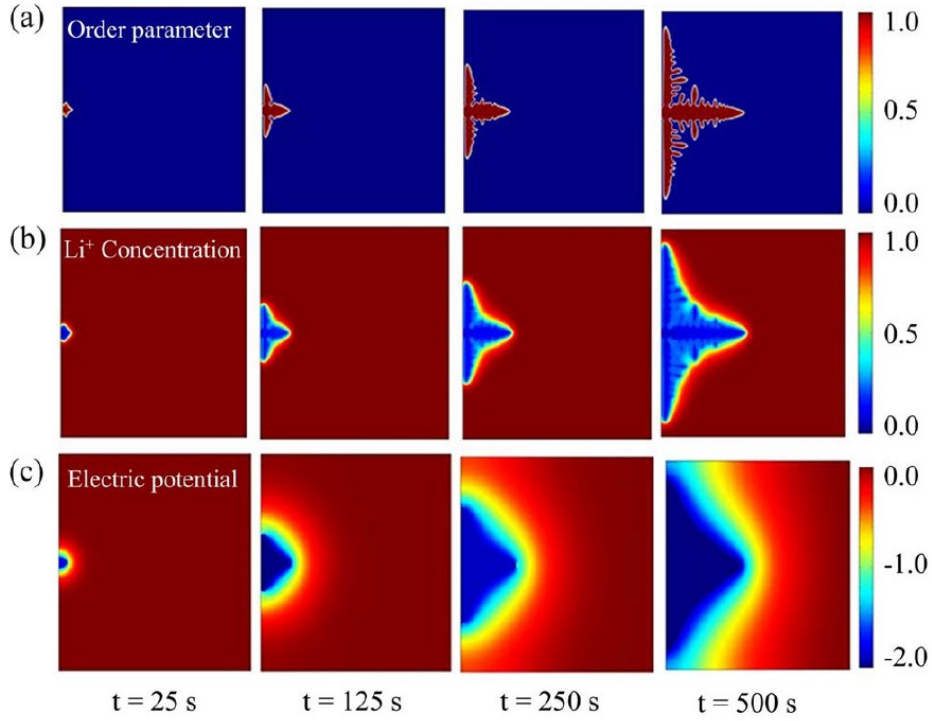

Figure 2-7. A snapshot of (a) order parameter, (b) normalized Li-ion concentration, and (c) electric potential (in V) at various simulation times, from [34].

This non-linear phase-field model has been extended and used by several groups to study the impact of external and internal driving forces on the Li dendrite. Chen et al. [34] predicted Li dendrite formation and growth under varying applied current density and surface roughness (Figure 2-8a). Later, Yurkiv et al. [35] extended this model to consider the non-uniform nature of the SEI layer by introducing a noise term into the Gibb's free energy and stress equilibrium equation. Different structures of Li dendrites such as moss-like and needle-like structures were observed, and each dendrite structure was dominated by different factors (Figure 2-8b). In addition, Yan et al. [36] extended the model to investigate the impact of temperature by considering temperature-dependent parameters such as Li-ion diffusion coefficient, as illustrated

in Figure 2-8c. The results indicate that the higher the temperature, the faster the Li-ion diffusion and the less severe the formation of Li dendrite. Hong et al. [37] developed thermal coupled electrodeposition phase-field model, and found that the formation of dendrite depends on the interplay between two temperature-dependent thermodynamic parameters: electrodeposition reaction barrier and ionic diffusion barrier. Furthermore, Mu et al. [38] conducted extensive investigations of the parametric study, studying the parameters such as anisotropic strength, applied voltage, and also porous structure of the SEI. Zhang et al. [39] studied dendrite growth in different 3D structured lithium metal anodes. They also studied the dissolution process of dendrite during discharging and revealed the critical factors that influences the formation of dead Li [40].

In summary, the non-linear phase-field model has proved to be a robust and powerful computation tool in predicting the evolution of Li dendrite under multiple influences [41]. Previous research has demonstrated the impact of applied current, geometry of initial perturbation, Li-ion diffusivity, non-uniformity nature of the SEI layer, and temperature on the growth behavior of Li dendrite. However, the fundamental knowledge of solid-solid contact between Li metal and SEI or solid electrolyte as well as mechanical influences have not yet been well established. Since the SEI layer or solid electrolyte is usually in mechanical contact with Li metal, the mechanical influences must heavily impact the Li electrodeposition behavior. Therefore, an electrochemical phase-field model that couples the mechanical contribution must be developed to reveal how Li deposition behavior responds to mechanical influences.

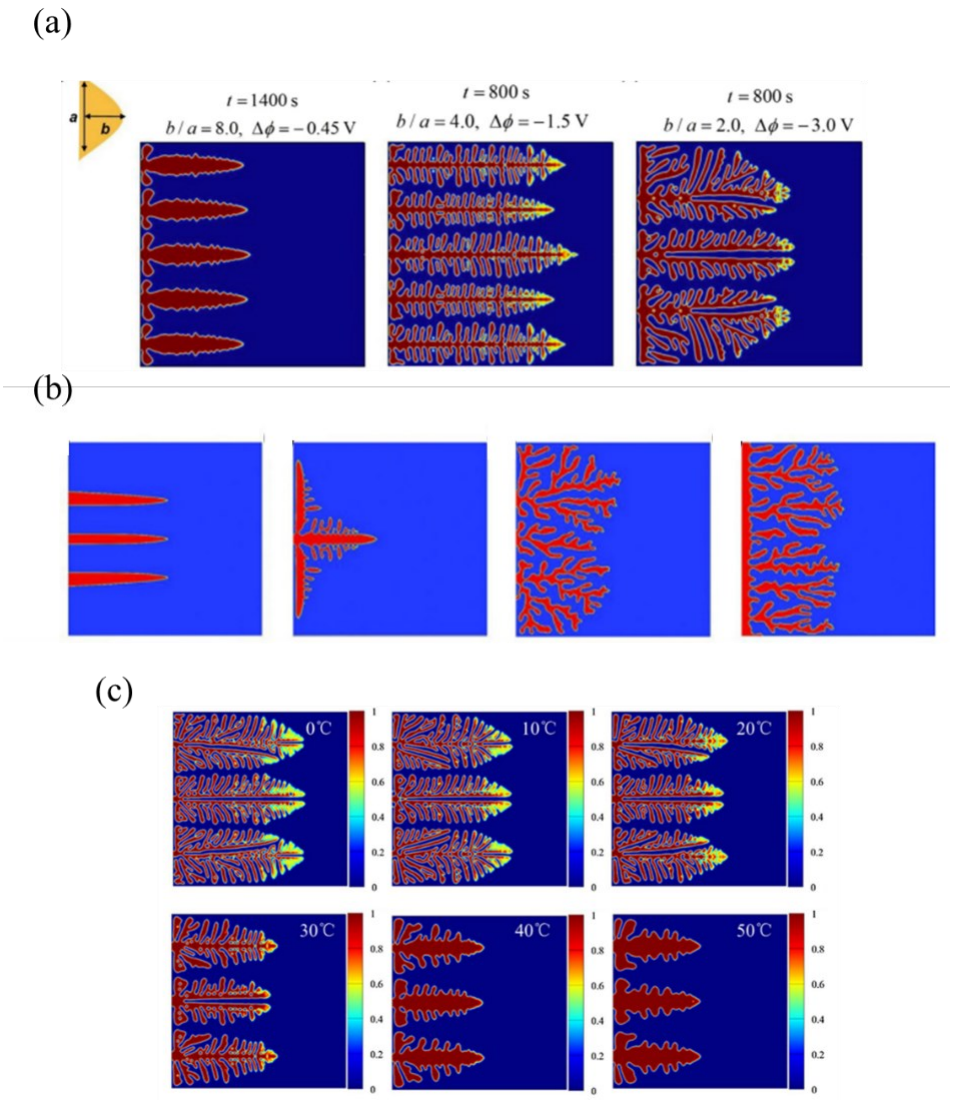

Figure 2-8. (a) Li dendrite morphologies as a function of applied current and initial surface roughness, obtained from [34]. (b) Several types of Li dendrite structures under varying conditions, obtained from [35]. (c) the temperature influences on the Li dendrite growth morphologies [36].

Chapter 3: An Electro-Chemo-Mechanical Phase-Field Model

The electrochemical non-linear phase-field model for Li dendrite growth has been previously developed by Chen et al. [34]. Here, in this dissertation, this electrochemical phase-field is extended to incorporate the impact of mechanics, in order to study the interaction between electrochemistry and mechanics in Li battery system. This chapter aims to illustrate the derivation of the electro-chemo-mechanical phase-field model and discuss the model in general. The modeling details and implementation for each specific application is provided in their Chapter 4, 5, and 6.

3.1 Mechanical Overpotential

The effect of mechanical stress on the chemical potential is derived from the classical Gibbs-Duhem Equation:

$$Nd\mu = VdP - SdT \tag{3-1}$$

where μ is the chemical potential, N is the mole of substance, S is entropy, V is volume, P is hydrostatic pressure, and T is temperature. For solids, the following assumptions are made: (i) N = 1, (ii) the stress is uniform over the molar volume, V_m, (iii) the metal behaves linearly elastic, and (iv) the process is isothermal (dT = 0) [42]. Due to the low compressibility of the solids, the

volume V can be described as $V = V_m \exp\left(-\frac{P}{K}\right)$ [43], where K is the bulk modulus. By integrating pressure from the initial to the final state, the equation is expressed as

$$\Delta\mu = \int_{P_1}^{P_2} V(P)dP = \int_{P_1}^{P_2} V_m \exp\left(-\frac{P}{K}\right) dP \approx V_m\Delta P - \frac{\Delta P^2 V_m}{2K}. \quad (3\text{-}2)$$

$V_m\Delta P$ represents the stress energy, and $\Delta P^2 V_m/2K$ is associated with the strain energy. As K is usually large for solid, the contribution from the strain energy can be negligible (For Li, K = 11 x 10^9 N/m^2, and V_m = 1.3 x 10^{-5} mol/m^3). Consequently, under the mechanical stress, the change of chemical potential of materials is described as

$$\Delta\mu = V_m\Delta P. \quad (3\text{-}3)$$

3.2 The Modified Butler-Volmer Equation

The reaction at the interface of the Li anode, $Li^+ + e \leftrightharpoons Li$, involves the competing influences of forward and backward reactions. When the forward reaction is dominant, the electrodeposition occurs. In contrast, if the backward reaction is more favorable, the Li metal is dissolved. The net of kinetic reaction can be written in the form of

$$R_t = -k_0 \left\{ \exp\left[\frac{-(\mu_t^{ex} - \mu_1)}{RT}\right] - \exp\left[\frac{-(\mu_t^{ex} - \mu_2)}{RT}\right] \right\}, \quad (3\text{-}4)$$

where k_0 is the reaction rate constant. μ_t^{ex} is the excess potential at the transition state. μ_1 and μ_2 are the electrochemical potential at the states of Li metal and Li-ion, respectively. To derive the expression for μ_1 and μ_2, it is convenient to write the potential for each component in chemical reaction equation:

$$\overline{\mu_{Li}} = RTlna_{Li} + \mu_{Li}^{0} + Pv_{Li} \tag{3-5}$$

$$\overline{\mu_{+}} = RTlna_{+} + \mu_{+}^{0} + F\emptyset_{s}, \tag{3-6}$$

$$\overline{\mu_{-}} = RTlna_{-} + \mu_{-}^{0} - F\emptyset_{e}, \tag{3-7}$$

where $\emptyset_s$ and $\emptyset_e$ are the electrostatic potential in the solid electrolyte and Li metal electrode, respectively. Pv_{Li} refers to the mechanical contribution that shifts the electrochemical potential of the electrode, where P is the hydrostatic pressure acting on the reaction front and v_{Li} is the molar volume of Li metal. μ_1 and μ_2 can be expressed as follows:

$$\mu_1 = \overline{\mu_{+}} + n\overline{\mu_{-}} = RTlna_{+}a_{-} + \mu_{+}^{0} + \mu_{-}^{0} - F(\Delta\emptyset), \tag{3-8}$$

$$\mu_2 = \overline{\mu_{Li}} = RTlna_{Li} + \mu_{Li}^{0} + Pv_{Li} \tag{3-9}$$

where $\Delta\emptyset = \emptyset_e - \emptyset_s$ represents the electric potential difference at the Li/SE interface. Next, to define μ_T^{ex}, it is assumed that the electrostatic potential varies linearly across the Li/SE interface. In addition, due to the nature of a solid-state system, the mechanical stress is intensified at the contact areas of the Li/SE interface where the reaction takes place. Thus, we assume that the mechanical action also contributes to the excess energy of the transition state, described as

$$\mu_T^{ex} = RTln\gamma_T + \alpha_a(F\emptyset_s - F\emptyset_e + \mu_{+}^{0} + \mu_{-}^{0}) + \alpha_c(\mu_M^{0}) + Pv_{Li}, \tag{3-10}$$

where γ_T is the non-ideal activity coefficient of the transition state. The anodic and cathodic charge transfer coefficients yield $\alpha_a = 1 - \alpha$ and $\alpha_c = \alpha$, respectively, where α is an asymmetric factor varying from 0 to 1. The equilibrium state is reached when $\Delta\mu = \mu_1 - \mu_2 = 0$, or

$$\Delta\mu = \frac{RT}{F} ln\frac{a_{+}a_{-}}{a_{Li}} + E^{o} - \Delta\emptyset^{eq} - \frac{Pv_{Li}}{F} = 0. \tag{3-11}$$

Thus, we have the equilibrium potential of the reaction under the excess pressure, P, expressed as

$$\Delta\emptyset^{eq} = \left(E^o - \frac{Pv_{m,Li}}{F}\right) + \frac{RT}{F} ln \frac{a_+ a_-}{a_{Li}}, \tag{3-12}$$

where

$$E^o = \frac{\mu_+^0 + \mu_-^0 - \mu_{Li}^0}{F} \tag{3-13}$$

is the standard potential difference between the reactants and products. Without pressure acting on the interface (P = 0), Equation (3-12) yields the classical Nernst equation. On the contrary, the presence of the mechanical action at the Li/SE interface shifts the standard potential difference E^o, resulting in a new equilibrium potential and thus a new exchange reaction rate or current density. In addition, the sign of P, is dependent on the state of stress at the interface: $P > 0$ refers to compression and $P < 0$ refers to tension. When the system is out of equilibrium, $\Delta\mu \neq 0$, the electrochemical reaction rate is regulated by the overpotential, which is defined as

$$\eta = \Delta\emptyset - \Delta\emptyset^{eq} = \Delta\emptyset - E^o - \frac{RT}{F} ln \frac{a_+ a_-}{a_{Li}} + \frac{Pv_{Li}}{F}. \tag{3-14}$$

The total overpotential (η) is comprised of (i) the activation overpotential, $\eta_a = \Delta\emptyset - E^o$, (ii) concentration overpotential, $\eta_c = -\frac{RT}{F} ln \frac{a_+ a_-}{a_{Li}}$, and (iii) the change of total overpotential due to the mechanical action or the mechanical overpotential, $\eta_m = \frac{Pv_{Li}}{F}$. By plugging in Equation (3-5), (3-6) and (3-7) into (3-4), the net reaction rate is expressed as

$$R_t = -k_0 \left\{ \exp\left[\frac{RT ln \frac{a_{Li}}{\gamma_T} + (1-\alpha)F(\Delta\emptyset - E^o)}{RT}\right] - exp\left[\frac{RT ln \frac{a_+ a_-}{\gamma_T} - \alpha F(\Delta\emptyset - E^o) - Pv_{Li}}{RT}\right]\right\}. \tag{3-15}$$

We assume that $a_+ = c_+$ and $a_- = c_-$, where c_+ and c_- are the normalized concentrations of Li-ion and electrons, respectively. With the definition of the overpotential in Equation (3-14) can be written in the form of

$$R_t = -R_{00}\left\{\exp\left[\frac{(1-\alpha)F(\eta_a+\eta_c)}{RT}\right] - \exp\left[\frac{-\alpha F(\eta_a+\eta_c)-F\eta_m}{RT}\right]\right\}, \quad (3\text{-}16)$$

or

$$I = -I_{00}\left\{\exp\left[\frac{(1-\alpha)F(\eta_a+\eta_c)}{RT}\right] - \exp\left[\frac{-\alpha F(\eta_a+\eta_c)-F\eta_m}{RT}\right]\right\}, \quad (3\text{-}17)$$

where $R_{00} = k_0(c_+c_-)^{1-\alpha}{a_{Li}}^{\alpha}{\gamma_T}^{-1}$ and $I_{00} = ek_0(c_+c_-)^{1-\alpha}{a_{Li}}^{\alpha}{\gamma_T}^{-1}$ are the exchange reaction rate and current density, respectively. By assuming that the electrons are abundant on the Li metal surface (c_- = 1), a_{Li} = 1, and plugging in $\eta_c = -\frac{RT}{F} ln \frac{c_+c_-}{a_{Li}}$, Equation (3-17) can be rearranged as,

$$I = -I_0\left\{\exp\left[\frac{(1-\alpha)F\eta_a}{RT}\right] - c_+\exp\left[\frac{-\alpha F\eta_a - F\eta_m}{RT}\right]\right\}, \quad (3\text{-}18)$$

where or $I_0 = ek_0a_{Li}{\gamma_T}^{-1}$. When $\eta_a < 0$ is applied, the energy landscape of $<Li^+ + e^->$ is shifted upward, thus the cathodic reaction is dominated ($I > 0$). However, the compressive stress ($\eta_m > 0$) moves down the energy landscape of $<Li^+ + e^->$, leading to a decrease of the deposition rate. On the contrary, the tensile stress ($\eta_m < 0$) further shifts the energy landscape of $<Li^+ + e^->$ upward, adding an additional driving force for the cathodic reaction rate. Furthermore, Equation (3-18) can be rearranged as

$$I = -I_0 exp\left[\frac{-(1-\alpha)F\eta_m}{RT}\right]\left\{exp\left[\frac{(1-\alpha)F\eta}{RT}\right] - c_+ exp\left[\frac{-\alpha F\eta}{RT}\right]\right\}, \quad (3\text{-}19)$$

where η is the overpotential across the deformed surface $\eta = \eta_a + \eta_m$. Therefore, alternatively, it can be thought that the surface stress impacts the magnitude of the exchange current density, $I_0^* = I_0 \exp\left[\frac{-(1-\alpha)F\eta_m}{RT}\right]$. Specifically, if the interfacial stress is compressive, $\eta_m > 0$, the exchange current density is diminished, resulting in a reduced reaction rate. Note that the formulation of this modified Butler-Volmer equation is different from the one proposed by Monroe and Newman [17], which implies that the mechanical action shifts the rate of anodic reaction. Nevertheless, the impact of the mechanical stress at the reaction interface from both formulations are the same: compressive stress diminishes the electrodeposition rate, while it is the opposite for the tensile stress, associated with the energy landscape shown in Figure 3-1.

Since the impact of stress on the electrochemical overpotential tends to vary from one to another material. A constant, C, is introduced to correct the mechanical contribution. This value can be obtained through experiment calibration.

$$\eta_m = C\,\frac{P v_{m,Li}}{F}. \tag{3-20}$$

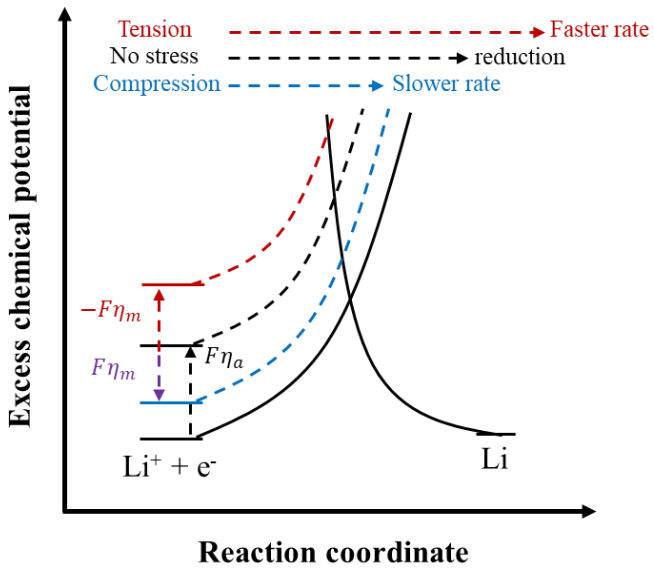

Figure 3-1 the plot of energy barrier against the reaction coordinate for the electrodeposition reaction, Li++ e ⇋ Li, under the influence of mechanical stress at the electrode interface [44].

3.3 The Electro-chemo-mechanical Phase-field Model

Previously, the Butler-Volmer equation has been modified to incorporate the effect of mechanical stress. This section aims to illustrate how this modified Butler-Volmer equation has been integrated into a phase-field model, following the process in reference [34]. The order parameter, ξ, is introduced to describe the phase evolution of Li metal: $\xi = 1$ refers to the Li metal, and $\xi = 0$ refers to the electrolyte phase. The phase transformation rate is driven by the electrodeposition rate of Li, expressed as $\frac{\partial \xi}{\partial t} = R_t$. Recall Equation (3-18) for the expression of the modified reaction kinetics. As the system is far from equilibrium, the driving force due to the concentration overpotential (η_c) is relatively small compared with the driving force due to the activation potential (η_a). Due to the solid nature of the system, the driving force from the change of overpotential due to the mechanical action (η_m) is significant. Therefore, it is assume that the

evolution of the phase-field linearly changes with the concentration overpotential, while varies exponentially with the activation and mechanical overpotentials [34]. The phase field equation is described as

$$\frac{\partial \xi}{\partial t} = -L_0(g'(\xi) - k\nabla^2\xi) - L_\eta \acute{h}'(\xi)\left\{\exp\frac{(1-\alpha)F\eta_a}{RT} - c_+\exp\left[\frac{-\alpha F\eta_a - F\eta_m}{RT}\right]\right\} + \delta_N, \quad (3\text{-}21)$$

where L_0 and L_η are the coefficients related to the interfacial energy and reaction, respectively. $h(\xi) = \xi^3(10 - 15\xi + 6\xi^2)$ is an interpolation function applied to describe the reaction at the diffuse interface. $g(\xi) = W\xi^2(1-\xi)^2$ is an arbitrary double well function, where W is the barrier height. k is a gradient coefficient. The driving force of dendrite nucleation, δ_N, represents the driving of Li dendrite due to the trapped electrons in solid electrolyte (See details in Chapter 5).

The phase-field equation is closely tied to electrostatic distribution, the mass transport and the stress equilibrium equations, and they must be solved simultaneously. The diffusion of Li-ion can be described by the classical Nernst-Plank equation, expressed as

$$\frac{\partial c_+}{\partial t} = \nabla \cdot \left[D^{eff}\nabla c_+ + \frac{D^{eff}c_+}{RT}nF\nabla\phi\right] - \frac{c_s}{c_0}\frac{\partial \xi}{\partial t}, \quad (3\text{-}22)$$

where $D^{eff} = h(\xi)D_{Li} + \big(1 - h(\xi)\big)D_e$ is the effective diffusion coefficient. D_{Li} and D_e are diffusion coefficients of Li-ion in Li metal and electrolytes, respectively. The last term on the right-hand side (RHS) of (29) relates to a sink term representing the decrease of Li-ions in the electrolyte due to the Li plating process. c_s = 7.64×10^4 mol m^{-3} is the site density of Li metal, and c_0 is the

bulk concentration. Next, the electrostatic potential is governed by the Poisson's equation with the source term representing the charges annihilation due to the reaction, expressed as

$$\nabla \cdot [\sigma^{eff} \nabla \phi] = I_R, \tag{3-23}$$

where $\sigma^{eff} = h(\xi)\sigma_{Li} + \big(1 - h(\xi)\big)\sigma_e$ is the effective conductivity. The source term, $I_R = nFc_+ \partial\xi/\partial t$, is non-zero at the metal/electrolyte interface where $\partial\xi/\partial t > 0$. The complete details of the model development can be found in reference [34]. Lastly, the stress equilibrium equation is expressed as:

$$\nabla \cdot \boldsymbol{\sigma} = 0, \tag{3-24}$$

where

$$\boldsymbol{\sigma} = \boldsymbol{C^{eff}} \cdot \boldsymbol{\varepsilon^{el}} = \boldsymbol{C^{eff}} \cdot (\boldsymbol{\varepsilon} - \boldsymbol{\varepsilon^0}). \tag{3-25}$$

$\boldsymbol{C^{eff}}(\xi) = h(\xi)\boldsymbol{C}_{Li} + \big(1 - h(\xi)\big)\boldsymbol{C}_e$ is the effective elastic stiffness tensor of the electrolyte. ε^{el} is the elastic strain, and small deformation theory is assumed. ε^0 is an inelastic strain due to the volume expansion of Li metal during the Li deposition process. It can be expressed as $\boldsymbol{\varepsilon^0} = \boldsymbol{K_{ii}}\xi$, where $\boldsymbol{K_{ii}}$ is a constant diagonal matrix. Nonetheless, $\boldsymbol{K_{ii}}$ is unknown; thus, to obtain the value for $\boldsymbol{K_{ii}}$, the calibration process is required. The governing equations are similar to the original electrochemical phase-field model in reference [34], expect for the addition of mechanical effect on the activation overpotential and the stress equilibrium equations.

Chapter 4: A Computational Design of 3D Architecture for Li Dendrite-free Anode

4.1 Introduction and Background

Li metal anode is the ideal electrode material due to its high specific capacity (3860 mA h g^{-1}), low electrochemical potential (-3.04 V vs. standard hydrogen electrode), and its low density (0.53 g cm^{-3}) [45]. Li metal anodes, however, still possess critical challenges that restrict its commercialization as a reliable electrode material. One of the main drawbacks is Li dendrite growth, which leads to the decay of coulombic efficiency, poor cycling performance, and even internal short circuits [46], [47].

Designing a 3D scaffold to host Li metal has been found to be one of the most effective approaches to solve Li dendrite problem. By recalling the Sand's time equation (2-2), reducing the local current density of the Li metal anode will significantly delay for the initiation and growth of Li dendrites ($\tau \sim 1/j^2$). The current density is basically the current over the active area (unit: A/m^2). Thus, if the active surface is large, the local current density can be substantially reduced, thereby the formation of Li dendrite is suppressed. By introducing a 3D structure, whose specific surface area is very high, Li dendrite problem should be significantly mitigated.

Thanks to the advancement of nanotechnology, 3D host structures could be fabricated in almost any shapes. The 3D nanomaterials, such as cellulose nanofibers [48], carbon felt [49] nickel

foam [50], [51], and copper microchannels [52], have been studied as a 3D host for Li metal anodes. Utilizing 3D host structure has shown a great success in improving battery safety and cyclability. However, at high current, the electrode architecture plays a bigger role in the morphological evolution of Li deposition. An excessive buildup of Li plating could occur on a sharp curvature area, introducing "hot spots" for Li dendrite formation [53].

Several studies show that the growth of Li dendrite starts with small nuclei, which result from the non-uniformity of the metal surface [54]–[56]. Due to the accumulation of electric charges on the nucleation tips, the local electric field strength is very strong at these points, attracts the large concentrations of Li-ions in the electrolyte to its sharp surface. Consequently, Li-ions are not evenly distributed, resulting in non-uniform local current density distribution at the electrode surface. Li rapidly grows on the sharp tips of the nuclei where the local current density is concentrated, while Li slowly deposits on the base where the local current density is relatively small [12], [23], [34], [54] causing Li dendrite formation as shown in Figure 4-1. To resolve the root causes of this problem, the ideal anode structure must feature uniform surface curvature to equalize the electric field.

In this dissertation, the well-spaced and uniform curvature nanotube is suggested as a 3D host structure. The ultra-uniform nanotube surface results in equally distributed electric field in the vicinity of the nanotubular wall. Therefore, Li-ions evenly migrate to the nanotubular surface, leading to uniform local current density distribution. Moreover, the spacing between each vertically-aligned nanotube gives direct pathways that promote Li-ion diffusion to the electroactive

areas and also provides confined spaces to accommodate Li growth. These electrode structural properties endow the uniform Li deposition on the nanotubular wall, resulting in the circumferential growth of Li nanotubes during Li plating (Figure 4-1).

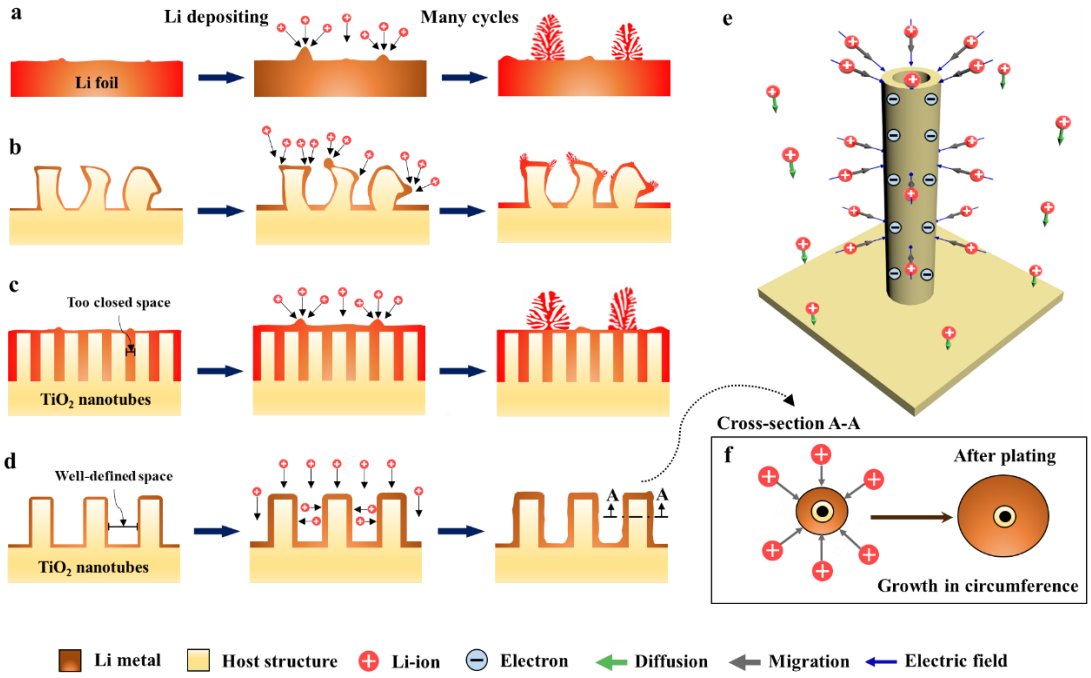

Figure 4-1. Schematic of Li deposition on four different anode structures. Li deposition on (a) Li foil, (b) vertically-aligned structure with non-uniform surface curvature, (c) closed Li nanotubes and (d) spaced Li nanotubes. (e) 3D schematic illustration of Li-ion transport under the influence of diffusion and the uniform electrostatic forces, which guide Li-ions to distribute over the nanotube surface uniformly. (f) 2D cross-section of a Li nanotube illustrating the unique electrodeposition manner, i.e., the circumferential growth of the spaced Li nanotubes [57].

4.2 Theory and Calculation

4.2.1 Phase-field Model

The model accounts for the electrochemical reaction kinetics at the surface of the electrode ($Li^+ + e \rightarrow Li$). The phase-field parameter (ξ), which continuously varies from 0 to 1, is used to

differentiate between the Li metal electrode ($\xi = 1$) and the electrolyte ($\xi = 0$). The morphological evolution of Li plating is governed by Allen-Cahn equation integrating Butler-Vomer kineties, expressed as

$$\frac{\partial \xi}{\partial t} = -L_\sigma(g'(\xi) - \kappa\nabla^2\xi) - L_\eta g'(\xi)\left\{\exp\left[\frac{(1-\alpha)nF\eta_a}{RT}\right] - c_+\exp\left[\frac{-\alpha nF\eta_a}{RT}\right]\right\}, \quad (4\text{-}1)$$

where $h(\xi) = \xi^3(6\xi^2 - 15\xi^3 + 10)$is an interpolating function, $L_\sigma$and L_η are the interface mobility and the reaction-related constant, respectively, η_a is the activation overpotential. The first and second term on the right-hand side (RHS) of (4-1) are related to the driving force due to the interfacial energy and electrochemical reactions, respectively. Equation (4-1) is solved simultaneously with mass and charge conservation equations, which are (3-22) and (3-23), respectively.

4.2.2 Implementation of Phase-field Model

The Li plating was simulated on COMSOL Multiphysics 5.3, employing the finite element method. We chose the mesh with small enough minimum grid spacing to effectively capture the moving interface. For the spaced Li nanotubes, the tube diameter, the tube length and the inter-nanotube space were 90 nm, 650 nm, and 150 nm, respectively (Figure 4-2). For the closed Li nanotubes, the tube spacing was reduced to 50 nm. However, for Li foil, the domain size was 4.0 x 4.0 μm. For initial conditions, the uniform Li nucleation sites were applied over the nanotube surfaces due to the uniform current density distribution near the nanotube walls. However, a few Li metal perturbations, resulting from the large volume change during cycling, were designed on

the Li foil surface. The initial Li-ion concentration in the electrolyte domain is 1.0 M, while the initial Li-ion in the electrode was absent, 0.0 M. The initial electric potential in the electrolyte domain and Li metal were 0.1 V, and 0.0 V, respectively. The Dirichlet boundary conditions for (29) and (30) were only employed at the opposite side of the electrode with the Li-ion concentration of 1.0 M and the electric potential of 0.1 V, respectively, to represent the bulk electrolytes. The electric potential of 0.1 V is chosen based on the magnitude of measured overpotential in electrochemical measurements at the first few cycles.

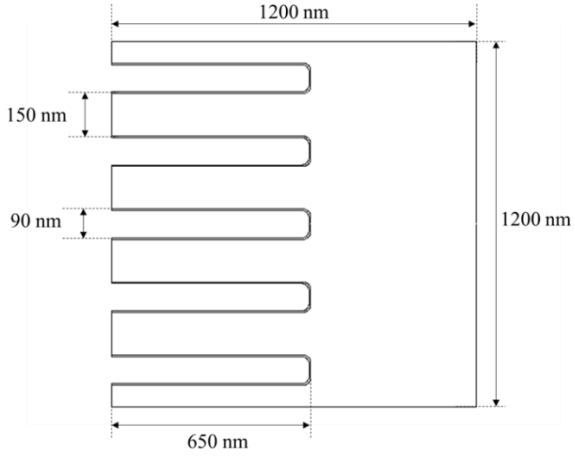

Figure 4-2. 2D nanotube geometry in phase-field simulation [57].

Table 4-1 Simulation parameters used in phase-field electrodeposition modeling.

Parameter	Value	Normalized value
Gradient energy coefficient, κ	1.5 x 10^{-5} (J m^{-1})	0.01
Li-ion diffusion in liquid electrolyte, D^{s}_{Li+}	9.0 x 10^{-10} (m^2 s^{-1})	180
Li-ion diffusion in electrode, D^{e}_{Li+}	9.0 x 10^{-13} (m^2 s^{-1})	0.18
Electrolyte conductivity, σ^s	1 (S m^{-1})	100
Electrode conductivity, σ^e	1 x 10^7 (S m^{-1})	10^9
Interfacial mobility, L_σ	1.33 x 10^{-5} (m^3 J^{-1} s^{-1})	200
Reaction constant, L_η	0.02 (s^{-1})	400

4.2.3 Current Density Distribution Modeling and Implementation

The secondary current distribution, which is a built-in model in COMSOL Multiphysics 5.3, is used to predict the current density and electric potential distributions in the electrolyte. The model assumes that in the electrolyte the charge transfer obeys Ohm's law, that is

$$i = -\sigma \nabla \phi, \tag{4-2}$$

where i is the current density, σ is the conductivity, and ϕ is the electric potential. The model considers the activation overpotential, $\eta_a = \Delta\phi - E^{\Theta}$, where $\Delta\phi$, and $E^{\Theta}$are the potential difference at the interface and the standard half-cell potential, respectively. The Butler-Volmer equation was chosen to describe the relationship between the overpotential and current density at the electrode interface, expressed as

$$j = j_0 \left(\exp\left[\frac{(1-\alpha) z F \eta_a}{RT}\right] - \exp\left[\frac{-\alpha z F \eta_a}{RT}\right] \right), \tag{4-3}$$

where j is the charge transfer current density, j_0 is the exchange current density, α is the cathodic charge transfer coefficient. The current density (j) was simply used to describe the boundary condition related to electrochemical reaction at the electrode surface, $n \cdot i = j$. Lastly, (35) was solved together with Nernst-Planck equation to predict ions movement under migration and diffusion in the dilute electrolyte, which can be written as

$$\frac{\partial c_+}{\partial t} = \nabla \cdot \left[D \nabla c_+ + z \frac{D c_+}{RT} F \nabla \phi \right], \tag{4-4}$$

where c_+, z, and D denote the Li-ion concentration, charge number and diffusion coefficient, respectively. For meshing, the very fine mesh size was applied on the electrode surface where the

gradient of current density likely occurred. A uniform nanotube has the inner and outer radius of 35 and 45 nm (for skeleton), respectively, with the Li metal layer of 10 nm covering the outer surface. A non-uniform nanotube was randomly designed with extremely non-uniform curvatures. For both cases, the length of the tubes was 650 nm. For simplicity, only movement of Li-ions was considered. The Li-ion diffusion coefficient was 0.9×10^{-9} m^2 s^{-1}. The exchange current density (j_0), and cathodic charge transfer coefficient were assumed to be 500 A/m^2, and 0.5, respectively. The electrode surface areas were selected as shown in Figure 4-3, with the designed electric potential of -1.25 V, while the rest of the surfaces were insulated. We considered no ion flux moving in/out the electrolyte boundary, except at the top boundary where a constant Li-ion concentration of 1 M is set. Lastly, for the initial condition, the electrolyte potential, and Li-ion concentration are assumed to 0 V, and 0 M, respectively.

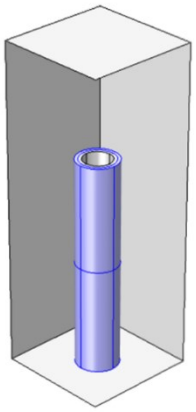

Figure 4-3. 3D geometry of the uniform nanotube used in current density distribution modeling [57].

4.3 Results

4.3.1 Current Density Distribution Model

According to the characteristic of a conducting object, the area of the highest curvature develops the greatest electric field strength out of its surface. In the electrodeposition system, blunt points, edges, and sharply curved areas on the electrode surface produce the most intense local electric fields. This electric field attracts a huge amount of surrounding Li-ions to the sharp points, leading to the inhomogeneous distribution of local current density, and consequently Li dendrite growth. On the contrary, the electric field strength on the electrode surface is homogeneous at the locations where the surface curvature is uniform. Li-ions evenly migrate to the electrode surface, leading to the uniform distribution of local current density, which contributes to the uniform Li deposition. Within, the current density distribution modeling was performed to understand the underlying mechanism of ionic diffusion and migration near the Li nanotubes surface.

Figure 4-4a shows the current density is distributed uniformly over the nanotubular walls, which is attributed to the ultra-uniform nanotube structure. Moreover, Figure 4-4b and c illustrate that at the simulation time, $t_0 = 5$ ms (the time at which the system reaches steady-state), the current density and Li-ion concentration distribution in the electrolyte are homogenously accumulated near the nanotubular wall. On the contrary, with a non-uniform tubular shape, the current density distribution is not uniform over the nanotubular wall due to the inhomogeneous Li-ion concentration at the surface (Figure 4-4d). The current density and Li-ion concentration distribution near the nanotube surface are not as homogenous as the uniform sample (Figure 4-4e and 4-4f). In this case, as evident from Figure 4-4g, the concave curve in the middle of the non-uniform nanotube contributes to uneven current density distribution. Figure 4-4h shows that along

the outer surface of the nanotube (at z = 325 nm), the current density is relatively high at the more curved areas, while the ultra-uniform nanotubular structure exhibits a flat current density profile.

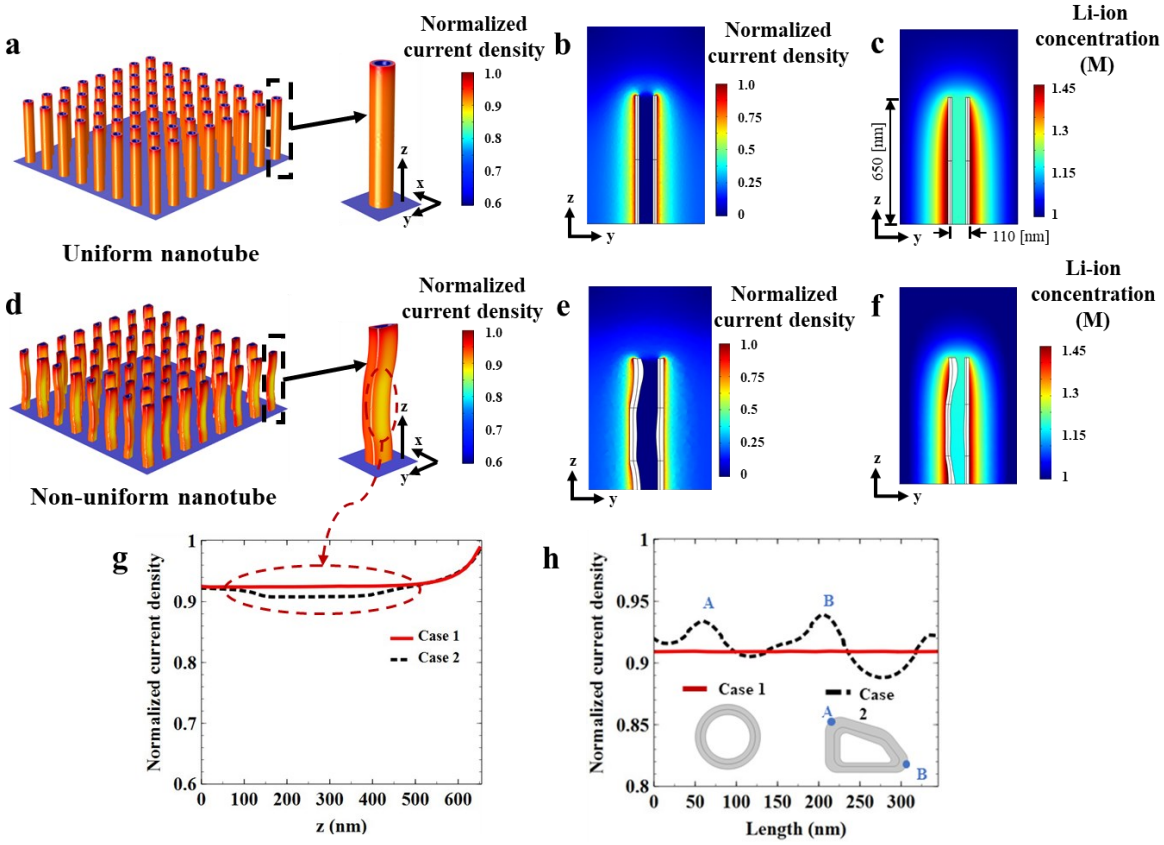

Figure 4-4. Simulation results for current density distribution modeling. a) The current density distribution over the Li nanotubes surfaces with ultra-uniform curvature. 2D plots of b) the normalized current density and c) Li-ion concentration distributions in the electrolytes near the ultra-uniform nanotube wall at the simulation time, t_0 = 5 ms (the time at which the system reaches steady-state). d) The current density distribution over the Li nanotubes surfaces with non-uniform morphology. 2D plots of e) the normalized current density and f) Li-ion concentration distributions in the electrolytes near the non-uniform morphology at the simulation time, t_0. g) A comparison plot of current density distribution on the nanotubes surface along the z-direction. h) A comparison plot of current density distribution along the perimeter of the nanotubes cross-section at z = 325 nm [57].

Nevertheless, sharp edges are inevitable in any tube structure, leading to the highest local current density. However, this problem is insignificant in the case of the nanosized structure because the difference in a degree of curvature between the nanotube body and its edge is insignificant. To elaborate on this theory, we investigated the preference of the nanotubular electrodes compared to the microtubular electrodes. The dimensions of the microtube used herein

are 10 times larger than the ultra-uniform nanotube. The normalized current density along the tube length for the uniform nanotube and microtube at the steady-state is plotted in Figure 4-5. The difference in magnitude of local current density between the tube body and its edge is clearly observed for the microtube, while the current density along the length of the nanotube is almost uniform. In addition, at the time t_0 (the time at which Li-ions evenly distribute on the nanotube surface), Li-ions are only accumulated at the top of the microtube (Figure 4-5b). Interestingly, Li-ions take a greater amount of time to distribute over the microtube surface uniformly (Figure 4-5c). The longer the time it takes for Li-ions to distribute over the electrode surface equally, the higher the chance it has for non-uniform Li deposition. Therefore, an excessive buildup of Li deposition is more likely to occur on the edges of the microtubes than on the nanotubes.

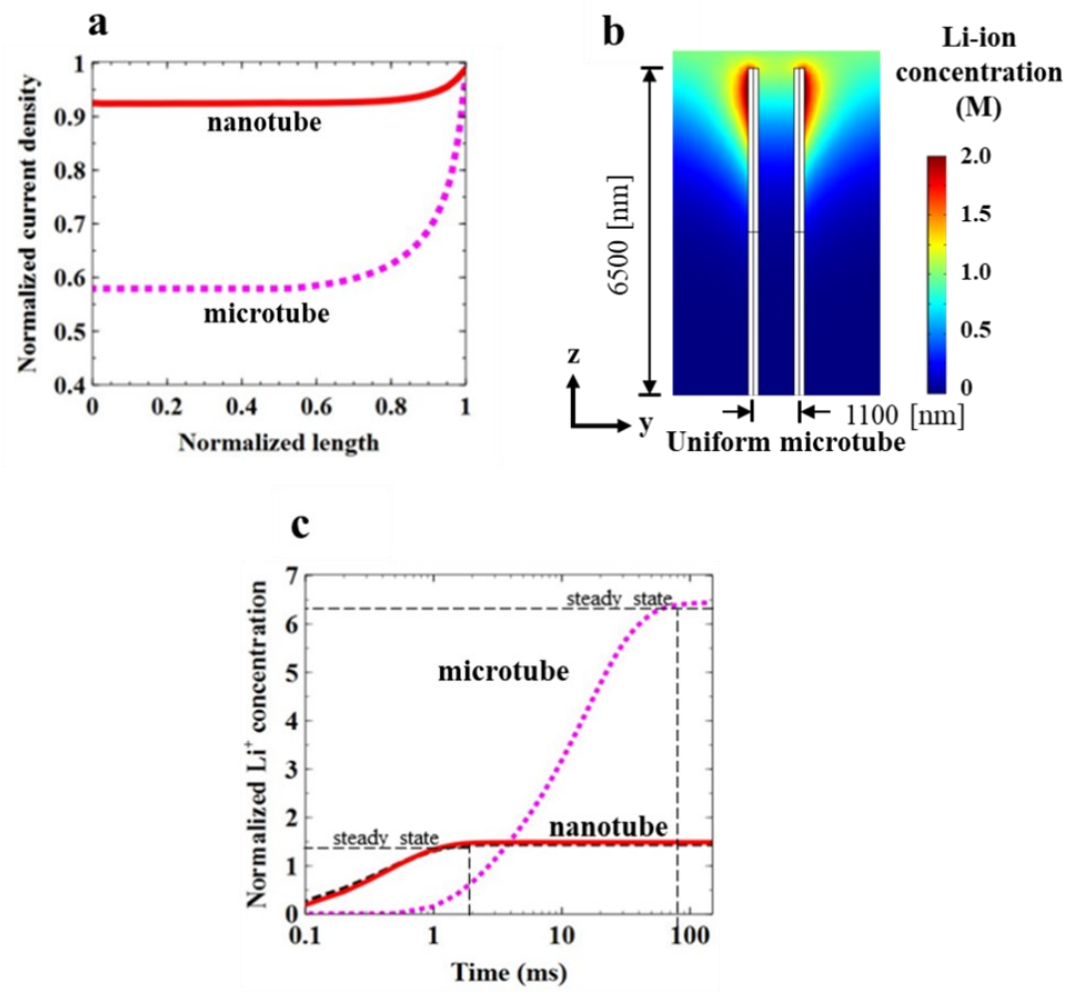

Figure 4-5. The current density simulation results of uniform microtubes sample. a) Plot of normalized current density along the tube length for uniform nanotube and microtube. b) The Li-ion concentration distribution on a 2D cut-plane along the uniform microtube wall at t_0 = 5 ms. c) Plot of time against Li-ion concentration at the middle of the tubes for 2 different cases [57].

4.3.2 Phase-field Model

To further explain the difference between the Li deposition mechanisms for the spaced Li nanotubes, compared to the closed Li nanotubes and Li foil, a nonlinear phase-field model with mass transport and charge conservation equations analysis was performed to simulate the Li deposition. On the Li foil surface, small Li nucleation sites occur at the electrode/electrolyte interface during cycling primarily due to the non-uniformity of the electrode surface. The tips of the nucleation sites induce the large Li-ion concentration [34], leading to the accumulation of local

current density. Li grows rigorously on the tips, thus resulting in the growth of Li dendrites as observed in Figure 4-6. Figure 4-6b illustrates that Li-ions are distributed unevenly, corresponding to the dendritic shape. Figure 4-6c displays that the current density is concentrated only at the dendrite tips. On the contrary, Figure 4-6d shows the uniform Li deposition on the spaced Li nanotubes. In Figure 4-6e, Li-ions are distributed uniformly over the nanotubular surfaces. The spacing between vertically-aligned nanotubes guides Li-ions moving vertically downward into the electroactive surface area. So, the ample amounts of Li-ions, which are ready for further Li deposition on the nanotubular wall, is present in the nanotube spacing. In Figure 4-6f, the current density distribution is homogeneous throughout the nanotubular walls due to uniform surface curvature. As a result, Li metal continues growing uniformly on the nanotube surface and is confined in the inter-nanotube spaces. However, for the closed Li nanotubes, Li deposition mostly happens at the top of the nanotubes, causing a wavy-like surface as shown in Figure 4-6g. Figure 4-6h shows Li-ions are concentrated near the top of the nanotubes. The current density profile follows the irregular surface of the deposited Li metal (Figure 4-6i). These findings imply that further Li deposition would occur on the irregular surface in the direction of the separator without space confinement. The wavy surface of deposited Li together with the accumulation of current density makes the electrode/electrolyte interface susceptible to the Li nucleation sites that eventually cause Li dendrite growth.

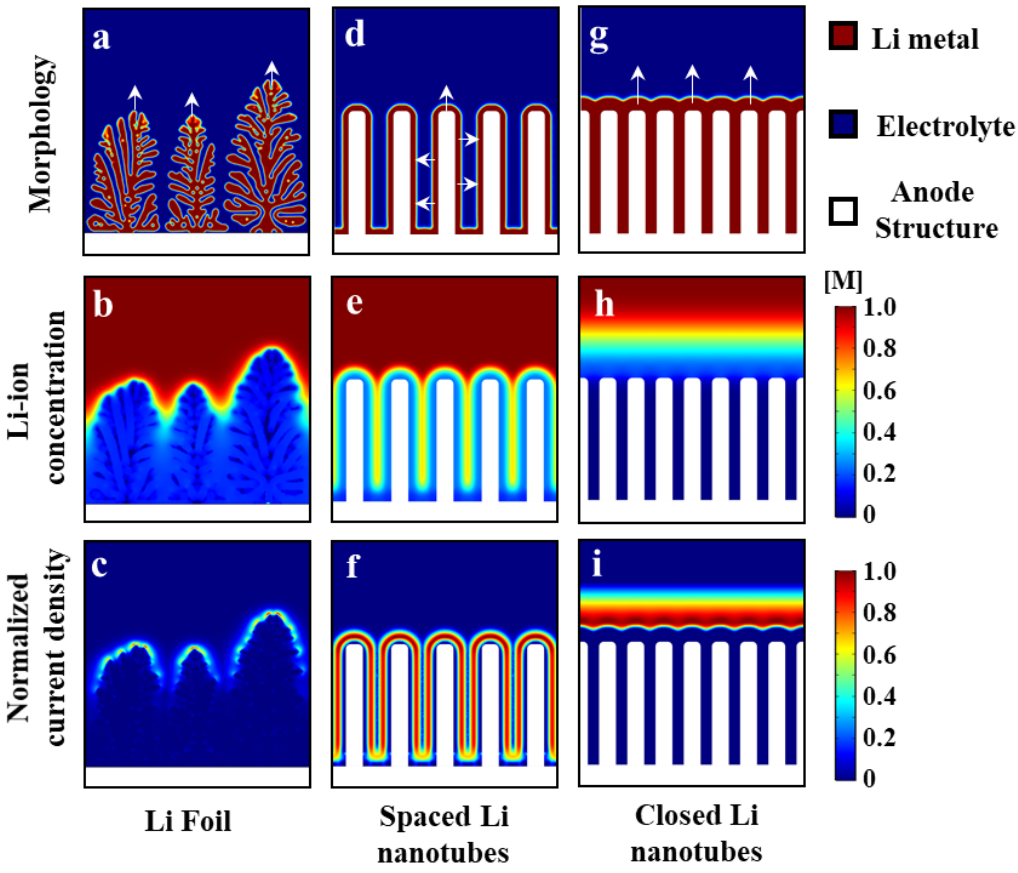

Figure 4-6. The simulated Li deposition morphology on a) Li foil, d) the spaced Li nanotubes and g) the closed Li nanotubes (white arrows indicate the Li growth directions). The normalized Li-ion concentration distribution in the electrolyte near b) Li foil, e) the spaced Li nanotubes and h) the closed Li nanotubes. The normalized local current density profile for c) Li foil, f) the spaced Li nanotubes and i) the Li closed nanotubes [57].

4.4 Experimental Validation

This section discusses the experimental verification of the merits of uniform curvature. The experiment has been performed by collaborators. Below are a summarize of key experimental testing. Full report of experimental works, including fabrication techniques and characterization procedures can be found in Reference [57].

Titanium dioxide (TiO_2) nanotube has been fabricated as a demonstration of 3D host structures that possesses two key characteristics (i) uniform surface curvatures, (ii) appropriate spaces to host Li metal. A structure called Li nanotubes is formed by infiltrating molten Li metal

into TiO_2 nanotube array. To measure the overall performance of the Li nanotubes electrodes, full-cell tests in 1 M LiTFSI in DOL/DME (1:1 v/v) with 2 wt.% lithium nitrate electrolytes were conducted. The spaced Li nanotubes and its Li foil counterpart are used as the anodes in two different cells, with $LiFePO_4$ used as the cathode for both cells. As shown in Figure 4-7a, the cell with the spaced Li nanotubes reveals excellent specific capacity even under the high charging rate (85 mA h g^{-1} at 10 C), which significantly surpasses its Li foil electrode counterpart (10 mA h g^{-1} at 10 C). The cell stability is further investigated using coulombic efficiency at 1 C. The spaced Li nanotubes cell shows great robustness with a coulombic efficiency of ~ 99.85% over 400 cycles (Figure 4-7b). No significant decay is observed over cycling with an average specific capacity of 132 mA h g^{-1}. On the other hand, with the Li foil anode, the specific capacity of the cell decays continuously during cycling from 120 mA h g^{-1} to 95 mA h g^{-1}. The voltage profiles for both cells at 0.5 C, 5 C, and 10 C are shown in Figure 4-7c-e, respectively. As can be observed, the cell with the spaced Li nanotubes shows a flatter voltage plateau at 0.5 C with a lower overpotential for both the charging and discharging cycles, compared to the cell comprised of Li foil anode. At 5 C and 10 C charging rates, the overpotential for the cell with Li foil significantly increases, while the cell with the spaced Li nanotubes still shows a flat voltage plateau, indicating greater electrochemical stability. The large specific capacity and exceptional coulombic efficiency at the high charging rate for the cell with the spaced Li nanotubes, are of great importance in high-energy applications that require fast charging/discharging speed with reliable performance and long-term stability.

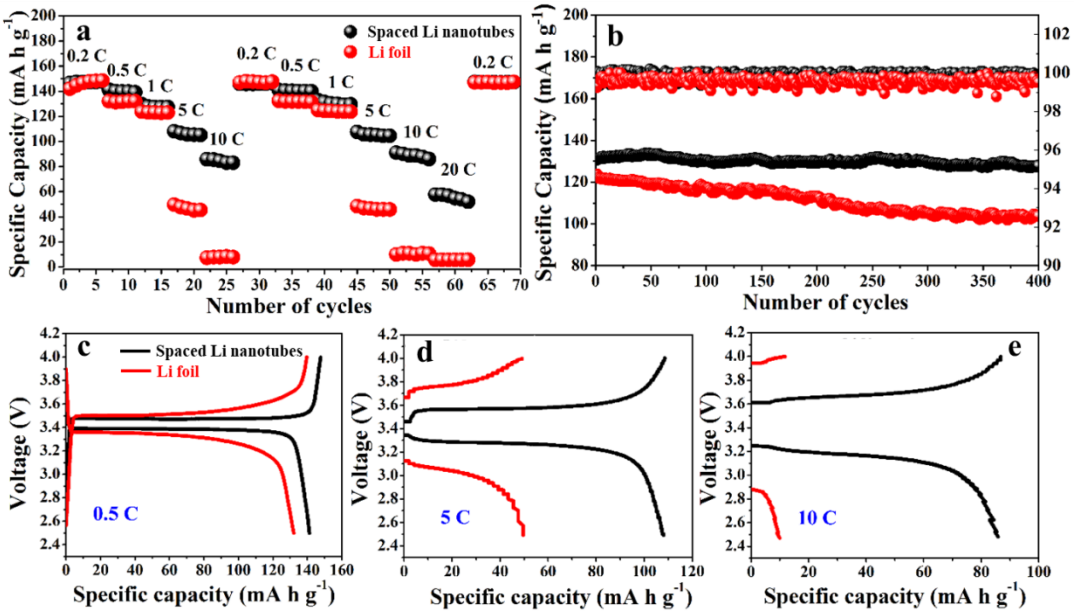

Figure 4-7. Electrochemical performance of full-cell batteries with LiFePO4/ the spaced Li nanotubes and $LiFePO_4$/ Li foil. a) Rate capability at various rates from 0.2 C to 20 C. b) Coulombic efficiency calculated at 1 C. Voltage profile comparison for each cell at c) 2 C, d) 5 C, and e) 10 C [57].

4.5 Conclusion

Two crucial characteristics of 3D host structures that lead to Li dendrite-free batteries are (i) uniform surface curvature and (ii) well-defined spacing. Li nanotube structure, which possess these two important characteristics is taken as an example.

First, uniform surface curvature homogenizes the local current density at the nanotube wall. homogenized current density leads to the uniform Li growth on the nanotube surface without Li dendrites. Also, such a uniform Li deposition behavior is considerably less likely to cause the mechanical rupture of the SEI layer, contributing to high interfacial stability during cycling. This approach to suppress Li dendrite growth is applicable to all types of electrolytes and remains effective in any structures as long as uniform surface curvature of the electrode is present.

Second, the well-defined spacing not only provides direct Li-ion diffusion pathways but also confined spaces. The sufficient space between nanotubes could host the Li deposition on the nanotubular wall, allowing each Li nanotube to steadily grow in circumference during Li plating.

Furthermore, the Li deposition behavior on the spaced Li nanotube is very unique and different from those of other vertically-aligned structures. Li deposits uniformly on the nanotubular wall, causing the lateral thickening in each Li nanotube. In addition, Li deposition direction is parallel to the separator, which helps to alleviate safety concerns. However, in previously reported vertically-aligned structures, the uniform Li deposition cannot be ensured due to the electrode architecture. In copper microchannels [52], for example, Li preferentially deposits on the sharp edges of the micropores and the deposited Li decreases in size from the upper to bottom surface of the microchannels. Moreover, in carbonized wood channels [58], Li grows on the surface of the microchannels, which are irregular due to the wood's nature.

The nanotube spacing impacts the cell stability and performance. Within this research, we demonstrate that, when compared to the spaced Li nanotubes, the closed Li nanotubes less effectively suppress Li dendrite growth, show lower interfacial stability and have inferior cycling stability. In addition, nanotube spacing is also a factor in determining the proper amount of Li metal that can be accommodated inside the structure. In this work, with the tube spacing of ~125 nm, some amounts of molten Li can be infused into the structure. Thus, the corresponding theoretical capacity of the cell somewhat decreases. The theoretical capacity can be improved by widening the nanotube spacing to host more Li metal. However, the reduction of the specific surface area and the large nanotube spacing might not be able to effectively suppress Li dendrite growth. Nevertheless, the effects of different nanotube spacing on the Li deposition morphology and cell performance have not yet been thoroughly investigated. To find an optimum design for the nanotube spacing, more efforts are needed.

Chapter 5: A Computational Study of Li Penetration in Solid Electrolyte

5.1 Introduction and Background

Solid electrolytes (SEs), an alternative to liquid electrolytes, are a potential solution to the Li dendrite problem [59]. SEs, which are made of ceramics, solid polymer, or their composites, have sufficient stiffness, such that they could be a physical barrier to the Li dendrite propagation, which significantly improves aspects related to safety and performance [17], [60]. In theory, High elastic modulus such ceramics materials [17], [61], [62] should be able to effectively suppress Li dendrite, Unfortunately, Li penetration in such promising ceramic SEs as $Li_7La_3Zr_2O_{12}$ (LLZO) is unexpectedly observed in experimental studies [63]–[67]. suggesting that the microstructural impact on the Li penetration behavior is significant. Still, the role of microstructure on the suppression of Li dendrite remains unclear.

In a solid-state system, electrochemistry and mechanics are intimately coupled: the volume expansion of the Li metal anode rises the stress variation at the Li/SE interface and this interfacial stress evolution impacts the electrochemical reaction rate. Specifically, the interfacial compressive stress, considered as a back stress that opposes the Li dendrite, evolves in the vicinity of newly deposited Li metal [17], [68], [69]. However, the inhomogeneity of mechanical properties of the SE due to the presence of microstructural defects could lead to a non-uniform stress distribution along the Li/SE interface, triggering Li nuclei on the Li metal surface (Figure 5-1a) [68]–[72]. In addition to the mechanical perspective, the excess electrons trapped in defects are recently proposed to be a viable cause of the isolated Li nucleation in the bulk SEs [73]–[76]. According

to DFT studies, the stoichiometric surfaces of cubic and tetragonal LLZO, which represent surfaces of microstructural defects, are electronically conductive [74], [75]. The excess electrons can be trapped in these surfaces, lowering the potential in the SE; thus, the reduction of the Li-ion in the bulk SE is possible [73], as illustrated in Figure 5-1a.

Once nucleated, the propagation and growth behaviors of Li dendrite are dominated by the mechanical properties of SE, rather than the electronic properties. Herein, we postulate that when the deposited Li metal is in contact with the soft media, such as GBs, the built-up interfacial compressive stress between Li and the GB is small. The small interfacial compressive stress indicates poor mechanical suppression of Li dendrite. Thus, Li preferentially penetrates along the soft GB, and the Li penetrants are likely confined in the GB regions by stiff grain interiors, as shown in Figure 5-1b. To confirm the above hypothesis, a physic-based theoretical model that explains this complex electro-chemo-mechanical behavior is required.

In this section, the developed electro-chemo-mechanical phase-field model is utilized to unveil the impact of microstructure of SE on the Li penetration behavior. The impacts of microstructural architectures and mechanical properties of the GB on the Li penetration behavior are investigated. Moreover, Li penetration in the standard LLZO system is simulated by involving intrinsic mechanical and electronic properties of SE to explain the phenomenon observed in experiments.

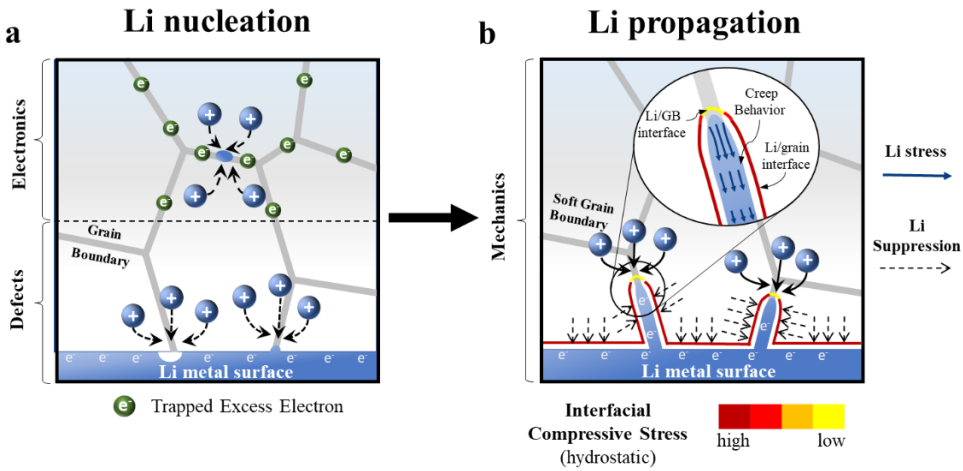

Figure 5-1. Schematic illustration of Li nucleation and propagation mechanisms (a) Li nucleation forms at the interface is due to the presence of defects, while isolated Li nucleation in the SE is caused by the trapped excess electrons in the GB. (b) Li preferentially propagates along the soft GB, at which the interfacial compressive is small, while Li unlikely grows toward the grain interior due to the large interfacial compressive stress [44].

5.2 Theory and Calculation

5.2.1 Phase-field Model

In this electro-chemo-mechanical phase field modeling, ξ, a phase field parameter, is introduced to distinct two phases: Li metal ($\xi = 1$) and SE ($\xi = 0$). The phase evolution of Li metal is driven by the interfacial free energy, the modified Butler-Volmer kinetics, and Li nucleation driving force. Besides, to describe the GB/grain as a diffused interface, we introduce another non-conservable phase-field parameter, φ, to differentiate the GB and the grain: GB ($\varphi = 1$) and grain ($\varphi = 0$). The phase field equations are expressed as

$$\frac{\partial \xi}{\partial t} = -L_0(g'(\xi) - k\nabla^2\xi) - L_\eta h'(\xi)\left\{\exp\frac{(1-\alpha)F\eta_a}{RT} - c_+\exp\left[\frac{-\alpha F\eta_a - F\eta_m}{RT}\right]\right\} + \delta_N, \tag{5-1}$$

$$\frac{\partial \varphi}{\partial t} = -L_0{}^s\frac{\partial F}{\partial \varphi}, \tag{5-2}$$

where L_0 and L_η are constants related to the interfacial mobility and the electrochemical reaction, respectively. δ_N represents the Li dendrite nucleation driving force [74], and is expressed as

$$\delta_N = \begin{cases} 1, & P_N = 1 - \exp(-J\Delta t) > \text{random}\,[0,1] \\ 0, & \text{otherwise} \end{cases}, \tag{5-3}$$

where P_N is a nucleation probability described by a Poisson distribution. More details are provided in the following subsection. Equation (5-1) and (5-2) are solved simultaneously with the mass transport (3-22), charge equilibrium (3-23), and the stress equilibrium equation. Stress evolution at the interface involves complicated contact mechanics [77], [78] creep or viscoplastic behavior of Li metal [79], [80] and the volumetric change of the electrode. To make the problem mathematically tractable, we assume that the inelastic strain due to the volume expansion of Li metal is the only source of the internal stress generation, and the contact mechanics is not considered. The stress equilibrium equation is expressed as,

$$\nabla \cdot \boldsymbol{\sigma} = 0, \tag{5-4}$$

where $\boldsymbol{\sigma} = \boldsymbol{C^{eff}}\,\boldsymbol{\varepsilon^{el}}$ and $\boldsymbol{\varepsilon^{el}} = \boldsymbol{\varepsilon} - \boldsymbol{\varepsilon^0}$. $\boldsymbol{C^{eff}}(\xi) = h(\xi)\boldsymbol{C}_{Li} + \big(1 - h(\xi)\big)\big(h(\varphi)\boldsymbol{C}_{GB} + \big(1 - h(\varphi)\big)\boldsymbol{C}_G\big)$ is the effective elastic stiffness tensor. $\boldsymbol{\varepsilon^{el}}$ is the elastic strain wherein small deformation theory is assumed. The inelastic stain, $\boldsymbol{\varepsilon^0}$, due to the volume expansion of Li metal during the Li deposition process can be expressed as $\boldsymbol{\varepsilon^0} = \boldsymbol{K_{ii}}\xi$, where $\boldsymbol{K_{ii}}$ is a constant diagonal matrix. $\boldsymbol{K_{ii}}$ is obtained by calibrating the resulting stress at the interface to the calculated stress reported in analytical and computational works [77], [81], [82].

5.2.2 Calibration of Eigenstrain Due to the Volume Expansion

Complicated mechanics problems are simplified by assuming that the volume expansion of Li metal is solely the origin of the internal stress generation, and the contact problem is not considered. The values of eigenstrain must reasonably give a similar magnitude of compressive stress to the analytical or computational approaches, which fully account for the mechanics problem. X. Zhang et al. [77] performed contact stress calculations by involving deformation, creep, and volume change of Li metal during the Li depositing/stripping process. The result indicates the maximum contact stress at the Li/SE interface is approximately -5.5 ± 1.1 MPa. In addition, Q. Tu et al. [82] carried out a theoretical study on the impact of the surface irregularity on Li deposition behavior by considering interfacial contact of Li/SE and plastic behavior of Li. The results show the maximum stress could reach -5.8 MPa around the defects. Both studies inform a magnitude of stress at the Li/SE interface is around a few megapascals (≤ 7 MPa). So, we determined $\boldsymbol{K_{ii}}$ values by changing the value of eigenstrain until the magnitude of stress at the Li/SE interface generally agrees with those reported analytical approaches.

5.2.3 Li Dendrite Nucleation Model

Following the work of H.K. Tian et al. [74], the driving force of dendrite nucleation, δ_N, is given by

$$\delta_N = \begin{cases} 1, & P_N = 1 - \exp(-J\Delta t) > \text{random } [0,1] \\ 0, & \text{otherwise} \end{cases}, \tag{5-5}$$

where P_N is a nucleation probability described by a Poisson distribution. J is the Li nucleation rate, which is expressed as

$$J = J_0 \exp\left(-\frac{\sigma_{inhomo}\Delta G}{k_b T}\right), \tag{5-6}$$

where J_0 is a constant related to the nucleation rate. σ_{inhomo} is a correction factor for heterogeneous nucleation. ΔG is the activation energy, which is a function of the chemical potential difference, written in the form of

$$\Delta G = \frac{16\pi\gamma^3 {v_{Li}}^2}{3\Delta\mu^2}, \tag{5-7}$$

where γ is the interfacial energy between the Li precipitates and the SE. v_{Li} is the molar volume of Li metal. The chemical potential difference is the summation of concentration and activation overpotential, expressed as

$$\Delta\mu = F\eta = F(\eta_a + \eta_c) = F(\Delta\emptyset - E^o) - RTln\frac{c_+ c_-}{a_{Li}}, \tag{5-8}$$

where c_- is the normalized electron concentration and defined as $c_- = 1 + \tilde{c_e}$. $\tilde{c_e}$ is the (normalized) trapped excess electron concentration. The activity of Li metal, a_{Li}, is unity and in the bulk SE the normalized concentration of Li-ion (c_+) is unity as well. In the scenario that the trapped electrons concentration $\tilde{c_e} > 0$, the concentration overpotential is rising, and thus, increasing the driving force for Li nucleation.

5.2.4 Model Implementation

The simulations are performed in COMSOL Multiphysics 5.4, which based on finite element method. The tetrahedral mesh is finely tuned in the GB region to ensure smooth calculation during the simulation. Mesh convergence is performed prior to running the simulation.

Here, two geometries are considered: (i) SE with a single grain boundary and (ii) Polycrystalline SE.

SE with a single GB

The simulation is carried out in COMSOL Multiphysics 5.4, employing the finite element analysis. The model involves 5 governing equations, which govern the phase fields order parameters (ξ, φ), Li-ion concentration (c), the electric field (ϕ), and displacement (u), respectively. Figure 5-2 illustrates the geometry and initial and boundary condition for all equations. The applied current density of 1.6 mA cm^{-2} can be correlated to the applied electric potential of 62.5 mV through Ohm's law: $J = \sigma \Delta \emptyset / L$, where L is the length of the electrolyte domain. The initial electric potential in the SE is set 62.5 mV, while the initial electric potential in the electrode is 0 mV. The initial normalized Li-ion concentration in the SE and the electrode domain are 1 and 0, respectively. The initial stress and displacement in both SE and electrode domains are zero. The Dirichlet boundary conditions are applied at the opposite side of the electrode with the normalized Li-ion concentration of 1 and the electric potential of 62.5 mV. In mechanics part, the roller boundaries are applied at the top and bottom. The right boundary is fixed, and the left boundary is subjected to either fixed displacement or stack pressure. Through calibration, the values of K_{11}, K_{22}, and K_{33} were determined to be $2.1\ x\ 10^{-4}$. The rest of model parameters are listed in Table 5-1.

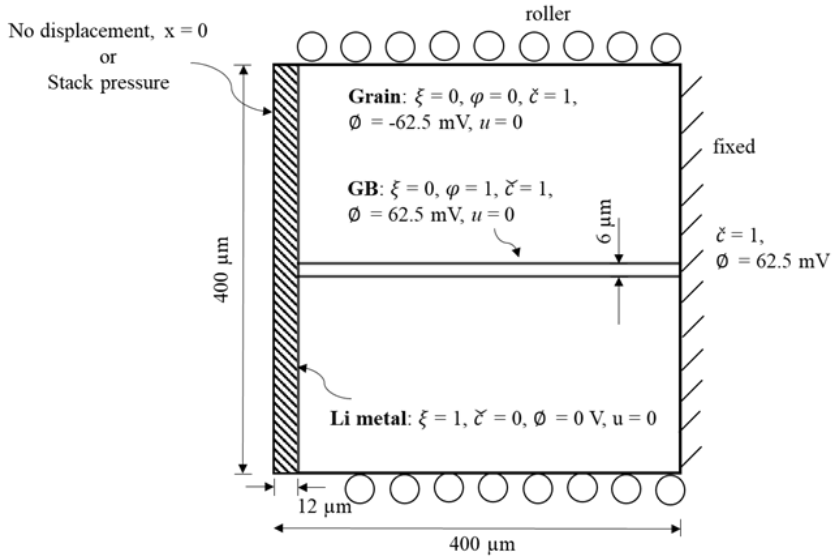

Figure 5-2 The geometry and initial and boundary condition of the Li deposition simulation in SE containing a single GB [44].

Polycrystalline SE

Figure 5-3 shows the geometry and all initial and boundary conditions. The domain sized was 61.25 x 35 µm. The grain structure is randomly generated with the approximate grain size of 7.5 µm. The thickness of the GB and initial Li metal electrode is 0.5 and 1.5 µm, respectively. The current density of 2.0 mA cm^{-2} is applied (correlated to the overpotential of 62.5 mV). The initial and boundary condition details are similar to the previous section. However, the calculated and measured LLZO properties such as ionic conductivity and mechanical property and a new set of parameters are utilized (Table 5-2). The elastic modulus of the grain is 158 GPa, while the elastic modulus of the softening GB is approximately 92 GPa [72]. The trapped electrons concentration of 0.337 mol/L [74], [75] is applied throughout the GB domain. The inelastic strain to the volume expansion, the matrix $\boldsymbol{K_{ii}}$, are $K_{11} = K_{22} = 5\ x\ 10^{-5}$ and $K_{33} = 2x\ 10^{-4}$.

The factor *C* is approximated through the calibration. Here, LLZO properties are utilized. Under such a high current density of 2.0 mA cm^{-2}, the Li dendrite penetration is expected. The *C*

factor is adjusted, such that the resulting Li morphology in LLZO resembles with the existing experimental observation that shows Li dendrites along the GB [63]. Thus, C = 24 is obtained.

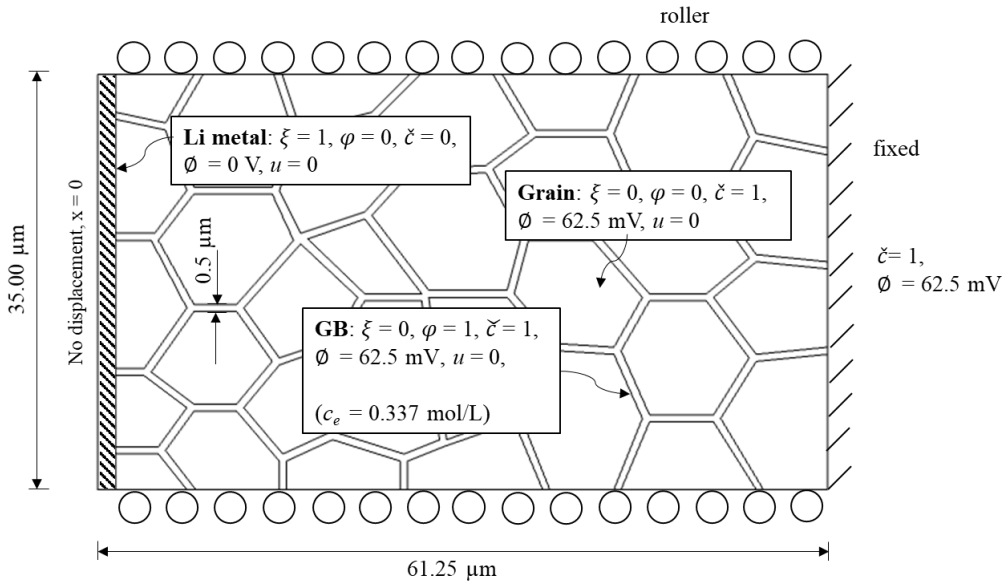

Figure 5-3. The geometry and initial and boundary condition of the Li deposition simulation in polycrystalline LLZO [44].

Table 5-1 Model parameters in simulation of Li deposition in a solid electrolyte (SE) with a single grain boundary. The characteristic values used in normalization are the following: l_0 = 100 x 10^{-6} m, Δt_0 = 4000 s, ΔE_0 = 5 x 10^5 J m^{-1}, c_s = 7.64 x 10^4 mol m^{-3}

	Unit	**Real Value**			**Normalization**	**Normalized Value**		
		Li	**LLZO**	**GB**		**Li**	**LLZO**	**GB**
System Size (l)	μm	400 x 400			$\breve{l} = l/l_0$	4 x 4		
Time step (Δt)	s	0.2			$\breve{\Delta}\mathrm{t} = \Delta\mathrm{t}/\Delta\mathrm{t}_0$	5 x 10^{-5}		
Li-ion diffusion coefficient (D)	m^2 s^{-1}	5.5 x 10^{-15}	5.5 x 10^{-12}	5.5 x 10^{-12}	$\breve{D} = D/({l_0}^2/\Delta\mathrm{t}_0)$	8.2 x 10^{-4}	8.2 x 10^{-1}	8.2 x 10^{-1}
Conductivity (σ)	S m^{-1}	1 x 10^7	0.1	0.1	$\breve{\sigma} = \sigma(RT\Delta\mathrm{t}_0)/(c_0{l_0}^2F^2)$	1.0 x 10^9	10	10
Elastic Modulus (E)	Pa	5.0 x 10^9	50 x 10^9	100 x 10^9	-	-	-	-
Poisson ratio	-	0.3	0.25	0.25	-	0.3	0.25	0.25
Gradient energy coefficient (κ)	J/m	3 x 10^{-5}	-	-	$\breve{\kappa} = \kappa\,/\,(E_0{l_0}^2)$	6.0 x 10^{-3}	-	-
Interfacial mobility (L_σ)	m^3 $(Js)^{-1}$	2.5 x 10^{-6}	0	0	$\widetilde{L_\sigma} = L_\sigma E_0\Delta\mathrm{t}_0$	5.0 x 10^3	0	0
Reaction constant (L_η)	s^{-1}	15.625	-	-	$\widetilde{L_\eta} = L_\eta\Delta\mathrm{t}_0$	6.25x 10^4	-	-
Symmetric factor (α)	-	0.5	-	-	-	0.5	-	-
Stress correction term (C)	-	12.5	-	-	-	12.5	-	-

Table 5-2 Model parameters in simulation of Li deposition in LLZO. The characteristic values used in normalization are the following: l_0= 35 x 10^{-6} m, Δt_0 = 10000 s, ΔE_0 = 5 x 10^5 J m^{-1}, c_s = 7.64 x 10^4 mol m^{-3}.

	Unit	Real Value			Normalization	Normalized Value		
		Li	LLZO	GB		Li	LLZO	GB
System Size (l)	μm	61.25 x 35			$\check{l} = l/l_0$	1.75 x 1.0		
Time step (Δt)	s	10			$\check{\Delta t} = \Delta t/\Delta t_0$	1 x 10^{-4}		
Li-ion diffusion coefficient (D)	m^2 s^{-1}	1 x 10^{-16}	1 x 10^{-13}	1 x 10^{-13}	$\check{D} = D/({l_0}^2/\Delta t_0)$	8.2 x 10^{-4}	8.2 x 10^{-1}	8.2 x 10^{-1}
Conductivity (σ)	S m^{-1}	2 x 10^7	2 x 10^{-2}	2 x 10^{-2}	$\check{\sigma} = \sigma(RT\Delta t_0)/(c_0{l_0}^2F^2)$	10 x 10^9	10	10
Elastic Modulus (E)	Pa	5 x 10^9	92 x 10^9	158 x 10^9	-	-	-	-
Poisson ratio	-	0.3	0.25	0.25	-	0.3	0.25	0.25
Gradient energy coefficient (κ)	J/m	1.1 x 10^{-6}	-	-	$\check{\kappa} = \kappa / (E_0{l_0}^2)$	1.8 x 10^{-3}	-	-
Interfacial mobility (L_σ, L_σ^s)	m^3 $(Js)^{-1}$	4.4 x 10^{-6}	0	0	$\check{L_\sigma} = L_\sigma E_0 \Delta t_0$	2.2 x 10^4	0	0
Reaction constant (L_η)	s^{-1}	27.5	-	-	$\check{L_\eta} = L_\eta \Delta t_0$	2.75x 10^5	-	-
Symmetric factor (α)	-	0.5	-	-	-	0.5	-	-
Stress correction term(C)	-	24	-	-	-	24	-	-
Molar volume ($v_{m,Li}$)	m^3 mol^{-1}	1.3 x 10^{-5}	-	-	-	-	-	
Bulk Li-ion concentration (c_s)	mol m^{-3}	-	42.2 x 10^3	42.2 x 10^3	-	-	-	-
Inelastic strain component K_{11}	-	5 x 10^{-4}	-	-	-	-	-	-
Inelastic strain component K_{22}	-	5 x 10^{-4}	-	-	-	-	-	-
Inelastic strain component K_{33}	-	2 x 10^{-3}	-	-	-	-	-	-
Nucleation parameters								
Nucleation rate pre-factor (J_0)	-	800	-	-	-	-	-	-
correction factor (σ_{inhomo})	-	1	-	-	-	-	-	-
Excess electron concentration (c_e)	mol m^{-3}	-	0	337	$\check{c_e} = c_e/c_{e0}$	-	0	0.337
Interfacial energy (γ)	J m^{-2}	0.05	-	-	-	-	-	-

5.3 Results

5.3.1 Influences of GB Softening

Polycrystalline SE contains GBs, which usually have a relatively low elastic modulus [69], [72], compared to the grain interior. Consequently, during the Li deposition process, built-up of compressive stress at the Li/GB interface is small, resulting in the current focusing and preferential Li deposition in the GB. To clarify this GB softening theory, Li deposition in a SE system with a single GB is simulated. Figure 5-4b shows the geometry of the simulation domain and the mechanical properties in the system. Note that no artificial nucleation site is employed on the interface. The current density of 1.6 mA cm^{-2}, which is large enough to generate the Li dendrites, is applied to drive the electrodeposition. Moreover, the theoretical studies show the internal stress of Li at the Li/SE interface is on the order of a few megapascals.[77], [81], [82]. Thus, through the calibration, the constants related to the inelastic strain were determined to be $K_{ii} = 2.1 \times 10^{-4}$.

The evolution of Li penetrant morphology and stress profile are shown in Figure 5-4c and d, respectively. Initially, the Li metal surface is perfectly uniform. After applying the current density, the first layer of deposited Li distributes uniformly on the Li metal surface. The Li metal electrode expands equally throughout the Li/SE interface, generating the uniform volumetric strain. However, the GB softening leads to a relatively low compressive stress at the Li/GB interface when compared to the stress at the Li/grain interface. At the simulation time t = 20 s, Figure 5-4e shows that the compressive stress in the GB region is approximately 2 times lower than the bulk grain region. This results in the acceleration of Li deposition rate in the GB. At the simulation time t = 200 s, a small Li penetrant is formed in the GB region as Li continues depositing on the interface which undergoes a small compressive stress. At the simulation time t = 400 s, the

formation of Li penetration is fully developed, and the penetration rate increases rigorously at this stage.

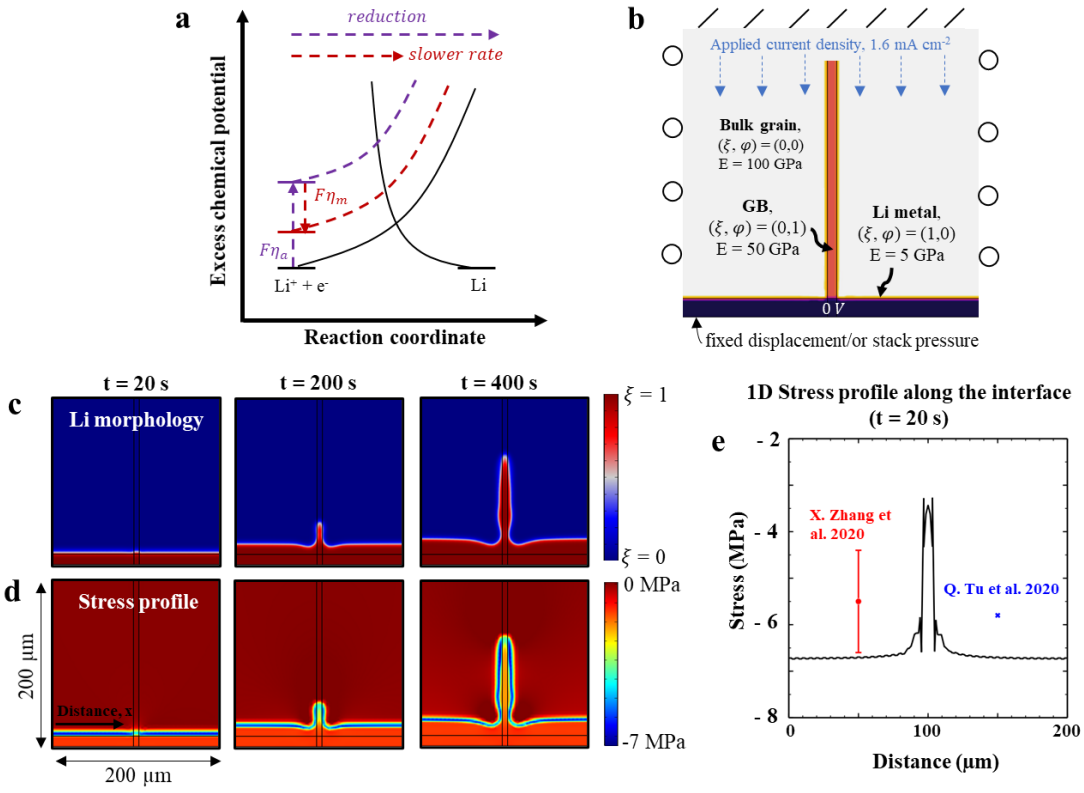

Figure 5-4. (a) The plot of energy barrier against the reaction coordinate for the electrodeposition reaction, $Li^+ + e \leftrightharpoons Li$, under the influence of mechanical stress at the interface. (b) The geometry, initial and boundary conditions, as well as mechanical properties used in Li deposition simulation. The evolution (c) Li morphology and (d) its associated stress distribution under a current density of 1.6 mA cm^{-2}. (e) the plot of resulting stress of Li along the Li/SE interface at the simulation time t = 20 s (black) together with the reported maximal interfacial stress in literatures, X. Zhang et al. [77] and Q. Tu et al. [82], retrieved from reference [44].

5.3.2 Microstructural Dependency

As Li penetrants are formed in the GB region, the microstructure and mechanical properties of GB could play an important role in governing the Li penetration rates and morphologies. In this section, several simulations are performed to illustrate the microstructure architectures and mechanical properties dependency. First, Li deposition behavior in the SE system with various angles between the GB and the Li metal surface is examined. The elastic modulus of the GB and

the grain are fixed at 50 GPa and 100 GPa, respectively. Figure 5-5a shows the size of Li penetrant is the largest when the GB boundary direction is perpendicular to the Li/SE interface. The stress at the Li/GB interface is similar for all cases, which indicates a similar mechanical contribution to the reaction rate (Figure 5-5b). However, the current density (Li deposition rate) decreases with a decrease in angle between the GB and the Li/SE interface. This is because Li tends to deposit in the direction of the electric field, which is the main electrodeposition driving force. When the GB is aligned in the same direction to the electric field, the Li penetration rate is the highest.

Next, Li deposition behavior under the different elastic moduli of the GB is investigated. Figure 5-5c indicates the softer the GB, the larger the size of the Li penetrant. The magnitude of stress at the Li/GB interface decreases with increasing degree of the GB softening. The lower compressive stress leads to the higher current density as shown in Figure 5-5d. Obviously, little to no differences in elastic modulus between the GB and the grain is desirable.

Lastly, the impact of the distancing between each GB on Li penetration rate is studied. The elastic modulus of the GB and the grain are fixed at 50 GPa and 100 GPa, respectively. As the gap between the GBs gets closer, the Li penetration rate decreases as shown in Figure 5-5e. Its underlying mechanism can be traced back to the distribution of Li-ions (Figure 5-5f). When the number of Li penetrants in the GB increases, Li-ions distribute more uniformly, thus slowing down the Li penetration rate. It is evident in Figure 5-5g that the Li-ion profile along the cut line at the tips of Li penetrants is more uniform when the gap between the GBs is small. This result implies that polycrystalline SEs with small grain size (or small distancing between GBs) is preferable.

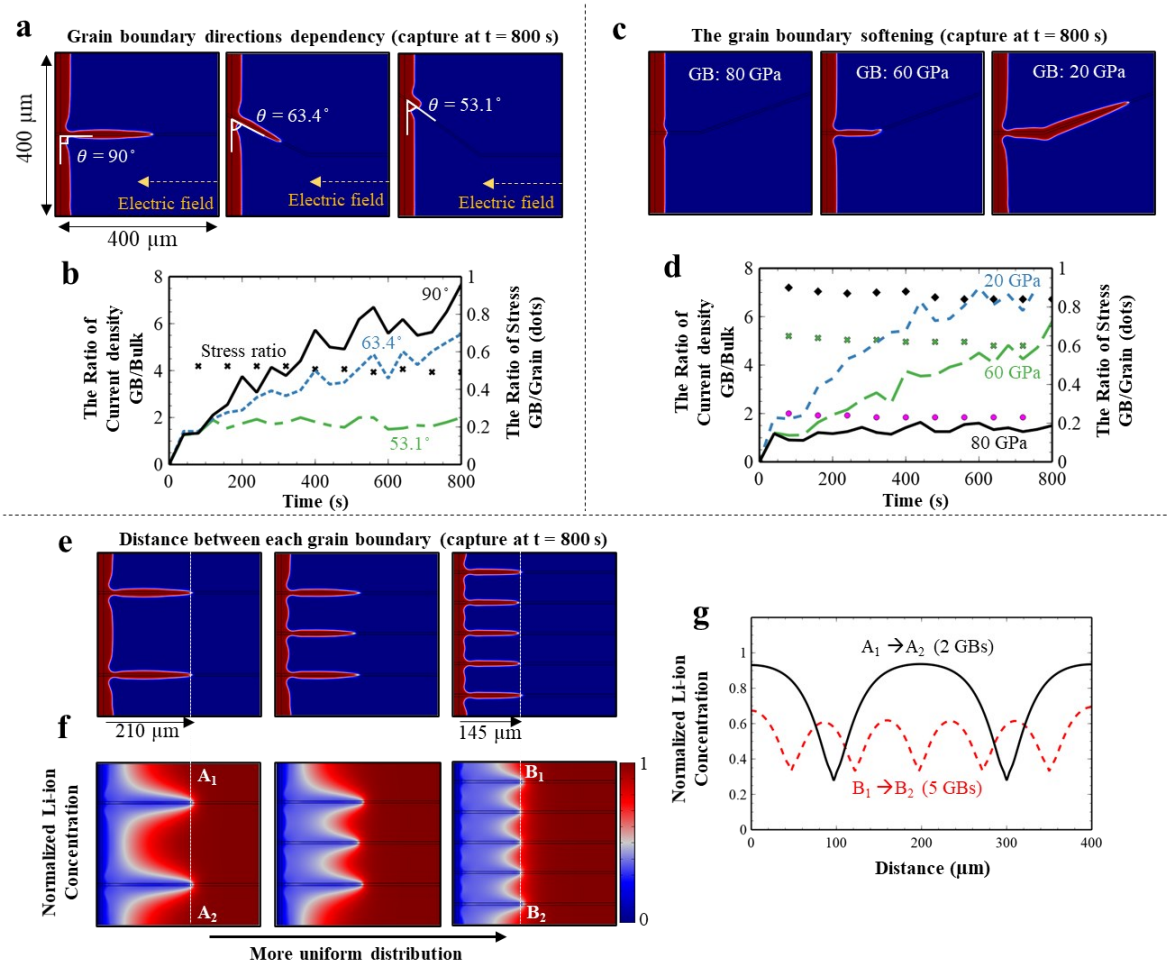

Figure 5-5. a) Li penetrant morphology in the solid electrolyte (SE) system consisting of a single grain boundary (GB) with various angles between the GB and the Li metal surface, captured at time t = 800 s. b) The plot of the ratios of (i) the local current density and (ii) interfacial compressive stress of the GB and the grain as a function of time, showing how the alignment of the GB influences the Li penetration rate. c) Li penetrant morphology in the SE system consisting of a single GB with different degrees of GB softening, captured at time t = 800 s. d) The plot of the ratios of (i) the local current density and (ii) interfacial compressive stress of the GB and the grain as a function of time, illustrating how GB softening impacts the current focusing in the GB. e) Li penetrant morphology and f) Li-ion concentration profile in the SE system consisting multiple GBs with different distancing. g) 1D plot of Li-ion concentration along the cut line A_1- A_2 and B_1- B_2 [44].

5.3.3 Impact of Applied Currents

The current density primarily determines the Li deposition rate. Under a high applied current density of 1.6 mA cm^{-2}, the deposition thickness reaches 30 µm within 400 s with a fully-developed Li penetrant in the GB as illustrated in Figure 5-6a. On the other hand, a low current density of 0.9 mA cm^{-2} leads to a slower rate and a more uniform Li deposition. Figure 5-6b shows

under the high applied current density, the current density at the Li/GB interface is twice of that at the Li/grain interface. In contrast, under the low applied current density, the current density is more uniform throughout the Li/SE interface.

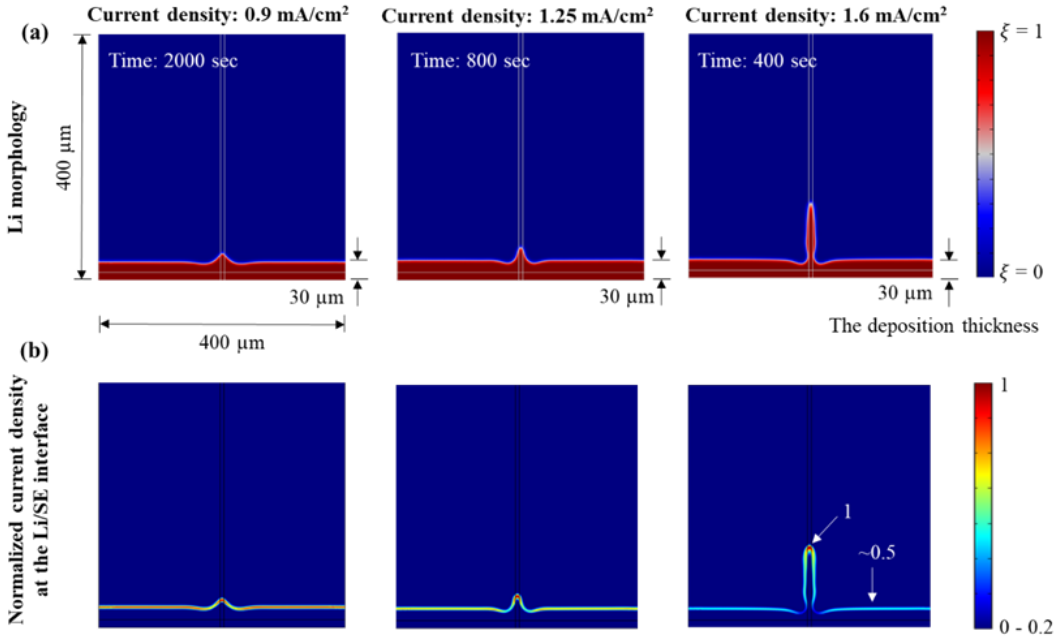

Figure 5-6 (a) Li morphologies under different applied current density captured when the Li deposition thickness reaches 30 μm. (b) The corresponding current density at the Li/SE interface normalized respected to the maximum current density [44].

5.3.4 Impact of Stacking Pressure

Figure 5-7a shows that although the overall Li deposition is reduced under the high stack pressure, the Li penetrant exists in the GB region. Stack pressure essentially adds compressive stress throughout the domain, including the Li/SE interface where the reaction occurs. Thus, the overall electrodeposition rate is slowed down. However, the magnitude of stress at the Li/GB and Li/grain interfaces are still largely different due to the inhomogeneous mechanical properties as shown in Figure 5-7b. Therefore, as long as the GBs or other defects at the interface exist, the Li penetration is possible.

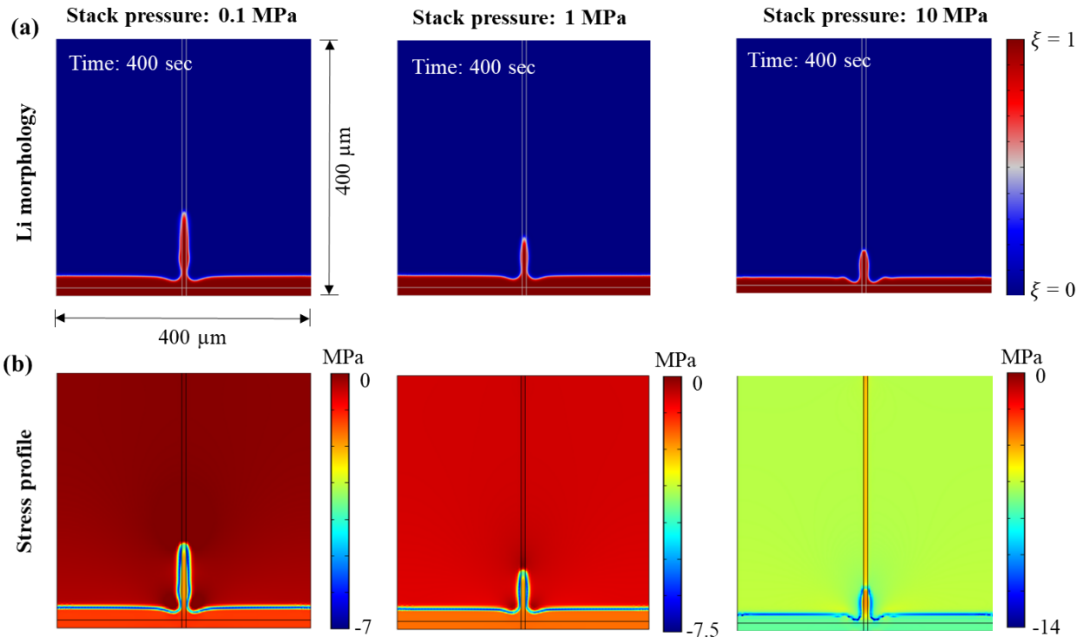

Figure 5-7 (a) Li morphologies under different stack pressure captured at 400 s. (b) The corresponding stress profile [44].

5.3.5 Intergranular Growth of Li Dendrites in LLZO

In this section, the electro-chemo-mechanical phase-field modeling is applied to simulate Li dendrite penetration in a more realistic simulation setup using LLZO. The simulation takes into account both stress and electronic contributions. Measured and calculated properties, including elastic modulus and Li-ion diffusion coefficient of LLZO, are utilized. The polycrystalline structure of LLZO is randomly generated with an approximate grain size of 10 µm. The elastic modulus of the grain is approximately 158 GPa, while the elastic modulus of the GB is 92 GPa [72]. The calculated trapped electrons concentration in the GB of LLZO is $c_e = 0.337$ mol/L [74], [75]. The current density of 1 mA cm^{-2} is applied, which is larger than the reported critical current density in LLZO at room temperature in most literature [63], [76], [83]–[85]. First, the Li deposition simulation is performed to highlight the growth of Li dendrite penetration under the influence of the GB softening. Figure 5-8a shows the evolution of the intergranular growth of Li dendrite in LLZO, which agrees with the experimental observations [63]. Figure 5-8b illustrates

that the compressive stress at the Li/grain interface is large, resulting in significantly impeded Li deposition into the grain. On the other hand, compressive stress at the Li/GB interface is small, leading to the preferable Li deposition location. Figure 5-8c reveals that Li-ions are distributed non-uniformly in the SE domain, further promoting the non-uniform Li deposition behavior.

Moreover, to demonstrate the impact of electronic contribution, the trapped electrons concentration is now considered. Figure 5-8d shows the morphological evolution of the intergranular growth of Li with an additional nucleation site far from the Li/LLZO interface. Theoretically, the Li nucleation probability arises exponentially with increasing excess electrons concentration (Figure 5-8e). The presence of trapped electrons in the GB (0.337 mol/L) raises the nucleation probability throughout the GB domain, as illustrated in Figure 4f. Once an isolated Li nucleation site is generated, Li propagates rapidly in the bulk SE in all directions along the GBs. The occurrence of the isolated Li nucleation leads to a sharp undesirable rise in Li penetration depth, as shown in Figure 5-8g.

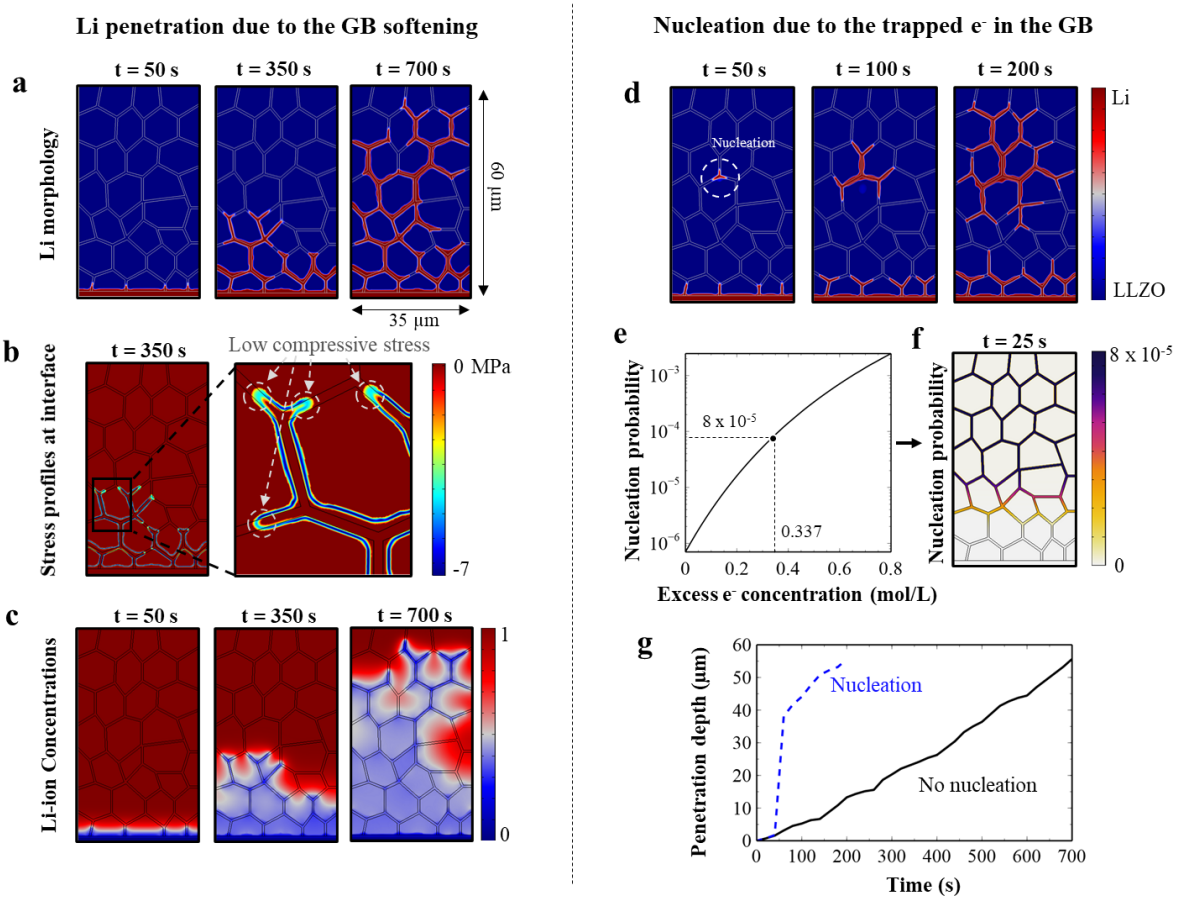

Figure 5-8. (a) The evolution of the Li penetrant morphology in polycrystalline LLZO with elastic modulus of 92 GPa and 158 GPa in the grain boundary (GB) and the grain, respectively. (b) The associated stress profile at t = 350s, which emphasizes the low compressive stress at the Li/GB interface. (c) The evolution of the normalized Li-ion concentration profiles. (d) The evolution of Li deposition morphology in the LLZO with the presence of isolated Li nucleation site due to the trapped electrons concentration. (e) The plot of Li nucleation probability against the trapped electron concentration. (f) The Li nucleation probability in the GB domain. (g) The plot of the Li penetration depth as a function of time for both cases [44].

5.3.6 Phase Map of Li Morphologies

This section aims to thoroughly investigate how the mechanical and electronic properties of the microstructure in the SE influences the Li penetration behavior. High-throughput simulations of Li deposition is carried out by varying the excess electrons concentration and the elastic modulus of the GB, under a constant applied current density of 1.0 mA cm^{-2}. Figure 5-9 represents the phase map of Li deposition morphologies as a function of the ratio between the elastic modulus of the GB and the grain (E_{GB}/E_{Grain}) as well as the trapped electron concentration.

Ideally, the absence of the trapped electrons and the homogeneous mechanical property lead to the uniform Li deposition on the Li metal surface without any sign of Li dendrites (region i). When the GB becomes moderately soft ($E_{GB}/E_{Grain} \sim 0.8$), Li nucleates at the GB junctions. However, the GB is not soft enough to be a favorable growth path for Li metal; therefore, Li grows in the direction parallel to the electric field, penetrating through the grain interior (region iii). Nonetheless, when the GB is soft ($E_{GB}/E_{Grain} < 0.7$), Li tends to deposit in the GB, forming the intergranular growth of Li dendrites (region ii). These simulation results indicate that the softness of the GB is a primary factor that indicates whether Li preferentially penetrates through the GB or the grain interior.

Furthermore, the increase of the trapped electron concentration in the GB rises the possibility of sporadic Li nucleation sites in the SE. The results show the isolated Li nucleation starts to appear when $c_e > 0.15$ mol/L. However, whether or not the continuous Li depositing on these nucleation sites causes dendrite penetration toward the cathode depends on how soft the GB is. For example, under the condition that the mechanical property of the SE is homogenous, the shape of scattered Li in the bulk SE is spherical, which unlikely leads to the short circuit (region v). However, when the GB becomes slightly softer than the grain, Li deposition likely occurs in the GB regions, forming scatter Li filaments in the bulk SE (region iv). Noticeably, in the bulk SE, Li penetrant is easier to form in the GB, compared the Li filament that grows from the root. This is attributed to the abundance of Li-ions (high concentration overpotential) in the bulk SE, which favors the electrodeposition rate. Nevertheless, when the GB is very soft, the rapid Li deposition in the GB tends to connect all Li filaments, forming large a web-like structure of Li dendrites (region ii), which doubtlessly short-circuits the batteries. As expressed, the presence of trapped

electrons just triggers isolated Li nucleation sites. Still, the softness of the GB is what dominates the growth behavior of Li filaments.

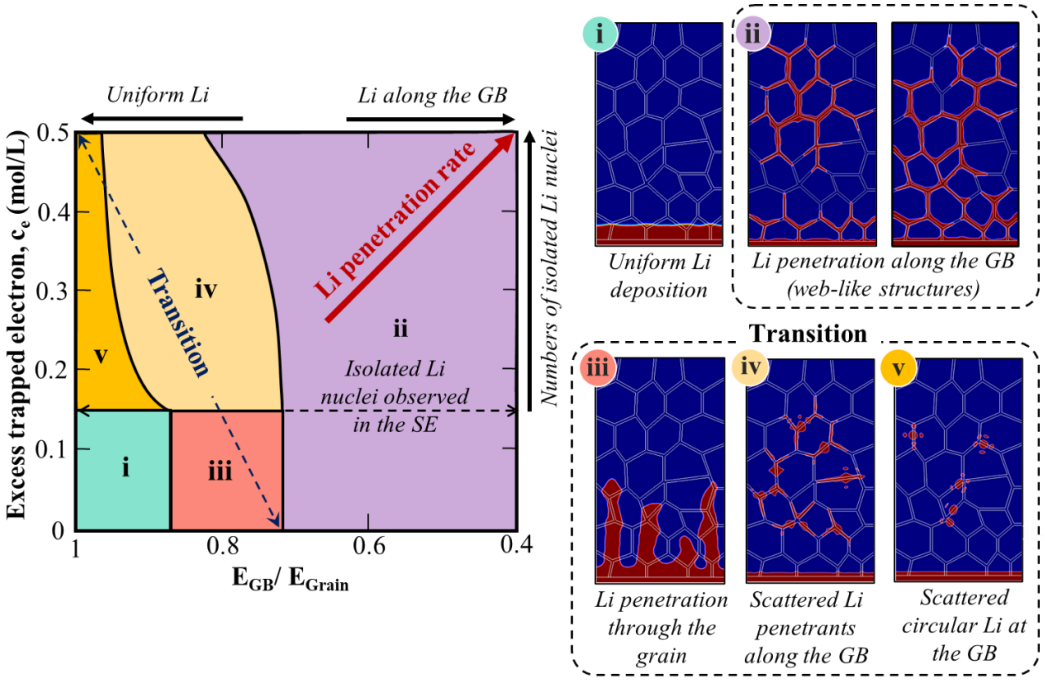

Figure 5-9 The phase map of Li morphologies as a function of elastic modulus mismatch between the GB and grain (E_{GB}/E_{Grain}) and trapped electrons concentration (c_e) in the GB region under an applied current density of 1.0 mA cm^{-2}. The mechanical action dominates the Li penetration growth behavior, while the trapped electron concentration controls the number of isolated Li nucleation sites in the SE [44].

5.4 Conclusion

We develop the electro-mechano-chemical phase-field modeling to reveal the Li nucleation and propagation mechanism in polycrystalline SEs. Our results show intrinsic mechanical and electronic properties of the GB play a role in controlling the Li penetration patterns. Firstly, we confirm that the mechanics/microstructure is the driving force behind the Li nucleation and growth on the Li metal surface. The existence of the GB, a soft media, locally leads to a small interfacial compressive at the Li/GB interface, during Li depositing. Thus, with the low opposing stress, Li preferentially nucleates and penetrates along the soft GB. In addition, we further demonstrate the impact of the microstructural architectures and mechanical properties of the SEs on Li penetration

behavior. Li penetration rate is the highest when (i) the GB is perpendicular to the Li/SE interface, (ii) the GB is very soft, and (iii) the distancing between each GB is large. Later, we employ our model to simulate the intergranular growth of Li in the famous LLZO by considering the electronic and mechanical properties, estimated by the atomic calculations. Li grows along the GB because of GB softening, and the excess trapped electron in the GB triggers an isolated Li nucleation in the bulk SE, which critically raises the Li penetration depth.

Lastly, we performed high-throughput simulations of Li deposition to draw a phase map that provides quantitative information on how the interplay between mechanical and electronic properties regulates Li deposition morphologies. The map can give an idea on what intrinsic property of the SE might be the primary cause of the observed Li penetration patterns. Hence, the further experimental verification can be done feasibly. We hope this fundamental and quantitative understanding of Li penetration mechanism can help facilitate the design of the novel SE materials.

Chapter 6: A Computational Design of Artificial SEI Layers for Li Dendrite-free Anode

6.1 Introduction and Background

The solid electrolyte interface (SEI) is the result of a reaction between Li and the electrolyte solvent, which forms on the surface of the Li metal anode and electrolyte [5], [86]. This is due to the reduction potential of the electrolyte solvent being typically below 1.0 V (vs Li+/Li), causing an immediate reaction once Li is immersed into the electrolyte [86]. The proposed structures of SEI are evolving over time due to the advancements in characterization techniques. The most accepted theory is called the mosaic model, which suggests that the SEI is made up of two parts: an inner inorganic rich and outer organic-rich layer and each layer is a mosaic assembly of different microphases [87]–[89]. However, the naturally formed SEI tends to be unstable because of the random distribution and composition of microphases, which contribute to the inhomogeneous mechanical properties as well as non-uniform Li-ion diffusion behavior into the surface of Li [90]. Therefore, instead of relying on the formation of a naturally formed SEI, an artificial SEI has been introduced to stabilize the Li metal interface [91]. The ideal interfacial layer should possess a high elastic modulus, possess good chemical and mechanical stability, have high ionic conductivity but low electronic conductivity [91]–[93].

Mechanical strength is one of the key property for suppressing Li dendrite, as a breakage in the SEI layer can result in the exposure of fresh Li metal to the electrolyte [94], [95]. This can lead to adverse consequences, such as side reactions, electrode degradation, and locally enhanced growth of Li deposition, which can eventually result in the formation of Li dendrite [94].

Therefore, high toughness or mechanical flexibility of the SEI is desirable. However, the Li metal surface is generally not uniform, and the fabricated SEI may contain defects, which can disturb the uniformity of Li-ion flux and increase susceptibility to Li dendrite formation. The SEI must also have sufficient mechanical stiffness to inhibit the non-uniform growth of Li deposition, similar to the suppression mechanism of the solid electrolytes.

However, to date, the analysis of mechanical stress and deformation in the SEI is in its infancy stage. *In situ* characterization methods such as SEM have revealed that the SEI imposes a compressive stress on Li nuclei, which significantly enough to drive the morphological evolution of deposited Li [96]. The mechanical interaction between the SEI and Li metal are computationally investigated, showing that the uniformity of SEI is the most effective way to enhance the mechanical stability of Li dendrites [97]. In addition, it has been computationally found that the preferential dendrite or cavity spots on the Li metal can cause the localized stress, leading to the rupture of the SEI layer [98]. However, the mechanism of how the SEI mechanically suppress Li dendrite has not yet been fully revealed.

During Li deposition, the insertion of newly deposited Li causes the rise of compressive stress at the Li/SEI interface, locally preventing the Li deposition at the perturbation tip. To satisfy the stress equilibrium, tensile stress develops elsewhere, promoting the Li deposition. The rate of Li deposition at the tip is slowed down, while the rate at other spots is accelerated, leading to the smoothening of the Li metal surface by the mechanical actions from the SEI layer. To confirm this hypothesis, a physic-based theoretical model that explains this complex electro-chemo-mechanical behavior is required. In this work, the electro-chemo-mechanical phase-field model is utilized to study the mechanical interaction between the SEI layer and Li metal. The effects of mechanical

properties such as elastic modulus and fracture strain, are studied, and later, high-throughput simulations are performed to suggest a design for dual-layer structure of the SEI.

6.2 Theory and Calculation

6.2.1 Phase-field Model

In this electro-chemo-mechanical phase field modeling, ξ, a phase field parameter, is introduced to distinct two phases: Li metal (ξ = 1) and electrolyte (ξ = 0). The phase evolution of Li metal is driven by the interfacial free energy, the modified Butler-Volmer kinetics. The impact of interfacial stress at the Li/SEI is incorporated as well. The phase-field equation is expressed as,

$$\frac{\partial \xi}{\partial t} = -L_0(g'(\xi) - k\nabla^2\xi) - L_\eta h'(\xi)\left\{\exp\frac{(1-\alpha)F\eta_a}{RT} - c_+\exp\left[\frac{-\alpha F\eta_a - F\eta_m}{RT}\right]\right\}, \tag{6-1}$$

The phase-field equation must be solved simultaneously with mass transport (3-22) and charge conservation equations (3-23). Stress evolution in the SEI layer is predicted by the stress equilibrium equation, expressed as

$$\nabla \cdot \boldsymbol{\sigma} = 0. \tag{6-2}$$

The source that raises the mechanical stress in the SEI layer is interfacial velocity of the diffuse interface (correlated with the rate of Li deposition), described as

$$v = -\frac{kL_\eta}{\gamma}\left\{\exp\frac{(1-\alpha)F\eta_a}{RT} - c_+\exp\left[\frac{-\alpha F\eta_a - F\eta_m}{RT}\right]\right\}, \tag{6-3}$$

where γ is the interfacial energy per unit area. Once Li is reduced at the electrode surface, the thickness of deposits Li increases, causing the interface to move. However, the local deposition

rate along the interface might not be uniform due to the local distribution of electric field ionic concentration. And this non-uniform velocity (v) is what causes the stress distribution in the SEI layer. And the stress state in the SEI has a direct impact on the local mechanical overpotential η_m and thus deposition rate: tensile stress promotes Li deposition rate, while it is the opposite for compressive stress.

6.2.2 Model Implementation

The simulations are performed in COMSOL Multiphysics 5.4, which based on finite element method. The simulation domain is 800 x 800 nm. The simulation configuration with initial and boundary conditions is shown in Figure 6-1 (not scale). The initial perturbation or surface roughness of 20 nm is introduced on the Li metal surface, serving as Li nuclei. The thickness of the SEI layer is 20 nm. The parameters used in the simulation in this section are listed in Table 6-1. A mesh convergence study is conducted to determine the appropriate mesh size for accurate and efficient simulation results using the finite element method. The triangular mesh with an approximate mesh size of 2 nm is selected for the SEI domain to capture the steep stress gradient in the SEI layer as well as the moving interface from the phase-field model, while a larger mesh size around 8 nm is used for the electrolyte domain to balance computational cost and accuracy.

Table 6-1 Simulation and phase-field parameters.

Parameter	Value	Normalized value
Gradient energy coefficient, κ	9.6 x 10^{-7} (J m^{-1})	0.008
Li-ion diffusion in liquid electrolyte, D_{Li+}^{s}	7.5 x 10^{-10} (m^2 s^{-1})	2.25
Li-ion diffusion in electrode, D_{Li+}^{e}	7.5 x 10^{-13} (m^2 s^{-1})	0.0025
Interfacial mobility, L_σ	6.67 x 10^{-1} (m^3 J^{-1} s^{-1})	2000
Poisson ratio of the SEI	0.2	-
Mechanical correction factor, C	0.1	-

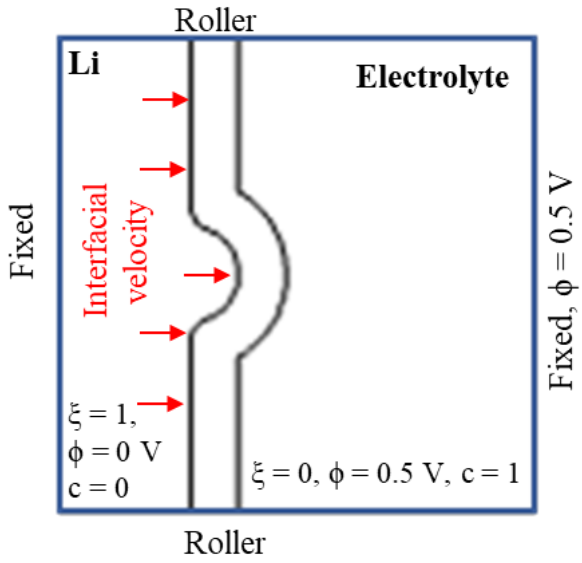

Figure 6-1. The geometry and initial and boundary condition of the Li deposition simulation under the mechanical influence of the SEI layer.

6.3 Results

6.3.1 A Single Layer

It is widely acknowledged that the SEI layer must be both stiff enough to inhibit non-uniform Li growth and flexible enough to withstand large volume change of Li metal during cycling. The aim of this section is to simulate how the SEI mechanically interacts with Li deposition behavior using the developed electro-chemo-mechanical phase-field model. Two materials, mechanically hard oxide Al_2O_3 and soft polymer alucone, are selected for the study. As demonstrated in Figure 6-2a, a hard layer is better at physically suppressing non-uniform Li growth. However, the stress and strain distribution in the layer is significant, with the maximum strain being even larger than the material's fracture strain. Therefore, the hard SEI layer is susceptible to cracking. Conversely, compared to a hard layer, a soft layer, which usually has excellent fracture toughness, is less likely to crack, but it has a poorer ability to block Li dendrites

(Figure 6-2b). Figure 6-2c illustrates that the mechanism of mechanical suppression relies on the interfacial stress. The newly deposited Li at the tip causes the compressive stress to rise, and to maintain stress equilibrium, tensile stress is developed around the base of the perturbation tip. Compressive stress at the tip slows down the Li deposition rate at the tip, while tensile stress accelerates the rate at the bottom of the pit, eventually resulting in a more uniform Li surface. Therefore, the higher the elastic modulus, the better the mechanical suppression ability.

To quantify how much surface roughness has been improved, the percent roughness change has been introduced: $\left(\frac{a-b}{b}\right)100\%$. Parameters A and B are the surface roughness (length from the tip to the base) before and after simulation, Figure 6-2d. If the SEI breaks, the roughness change is considered similar to the case without a mechanical SEI because the SEI can no longer physically block Li dendrites. Figure 6-2e shows the phase map of percent roughness change as a function of elastic modulus and fracture strain in percent. Blue region is preferable, where surface roughness is reduced, while it is the opposite for the red region. Unfortunately, the available materials for SEI fabrication are mostly in the red zone, where surface roughness increases. Soft materials are too soft to suppress Li dendrites, while hard materials are susceptible to crack due to their brittleness. A dual layer, a combination of soft and hard layers, is a possible solution.

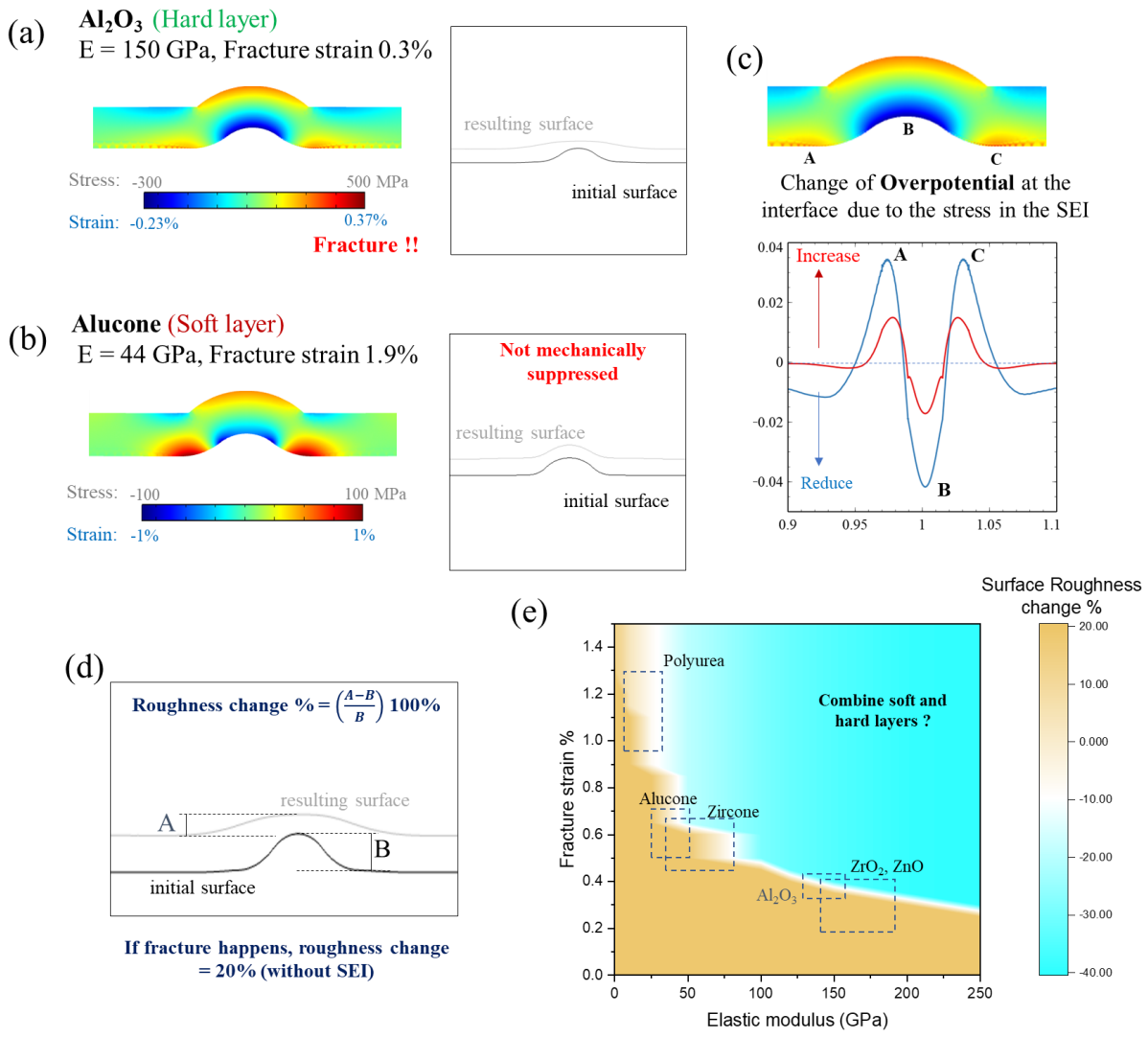

Figure 6-2. Mean stress and strain distribution on the (a) hard Al_2O_3 and (b) soft Alucone interfacial layers, with the morphological change of Li surface before and after simulation. (c) plot of electrochemical overpotential change due to the interfacial stress along the interface. It shows with a higher elastic modulus of the SEI layer, the higher driving force from mechanical actions. (d) Schematic explaining roughness change calculation in this work. (e) the phase-map of the change of surface roughness a function of elastic modulus and fracture strain%.

6.3.2 A Dual Layer- Problem Description

The idea of a dual layer SEI in Li battery technology has already gained significant attention for its potential to improve cyclability and performance [99]–[103]. The aim is to combine the best qualities of inorganic and organic layers. Typically, inorganic layers are strong and stiff, but lack flexibility and ionic conductivity, while organic layers are flexible and have

good ionic conductivity but have low elastic modulus. However, those previous studies primarily focused on synthesizing materials for the SEI or discovering promising SEI materials but have overlooked the design aspect of how to effectively combine the organic and inorganic layers. This section aims to use the developed computational approach to provide design guidelines and answer the question of how to combine soft and hard layers. Design parameters can include materials properties for (i) the soft and (ii) hard layers (such as elastic modulus and fracture stain), (iii) the ratio of thickness between the soft and hard layers, (iv) the total thickness of the layer, and (v) the order of the layer (whether the soft layer comes before the hard layer or vice versa), and they will be considered from a mechanical perspective. Ionic diffusivity and adhesion force will be addressed in future work for the sake of simplicity.

The presence of multiple design parameters presents a challenge in thoroughly analyzing and provide a design recommendation. To simplify the problem and reduce the number of parameters, certain assumptions must be made. From the mechanical aspects, an increase in SEI thickness is desirable as it offers greater stress relief due to the addition of solid material content, reducing the risk of fracture. However, this also leads to lower ionic conductivity and thus increased internal resistance, which negatively impacts the battery performance. The total thickness has to be optimized. As ionic diffusion is not being considered in this work, we simply follow the previous experimental finding that an optimal SEI thickness of 20 nm [100], [104] should be used as a fixed constant for all case studies.

6.3.3 Soft/Hard or Hard/Soft

This section aims to determine the optimal sequence, whether it should be Soft/Hard or Hard/Soft, which will be then used as fixed design parameters for future study cases. Through qualitative analysis of stress and strain distribution, as depicted in Figure 6-2a, it appears that the

maximum strain is likely to occur at the outer side of the SEI or at the SEI/electrolyte interface. Thus, the outer layer should consist of flexible materials capable of withstanding large deformation, while the inner layer should be composed of stiff and strong materials, able to generate a large magnitude of stress at the Li/SEI interface to mechanically suppress the growth of Li dendrite. Therefore, the sequence of layers should be Hard/Soft.

To confirm this optimal sequence, the developed phase-field model for the SEI is performed. The simulation is set up similar to the previous section, with the mechanical property of the 20 nm SEI subdivided into two layers (without considering contact between each layer). The hard and soft materials are Al_2O_3 with E = 150 GPa, and alucone with E = 44 GPa, respectively. Comparison of the mechanical response between two different sequences under the same electrochemical boundary condition is demonstrated in Figure 6-3. When the soft layer is on the outside, deformation is well accommodated, and the maximum strain is less than 0.15%. Conversely, when the hard layer is on the outside, the maximum strain could reach up to 0.25%, making the SEI more susceptible to fracture.

.

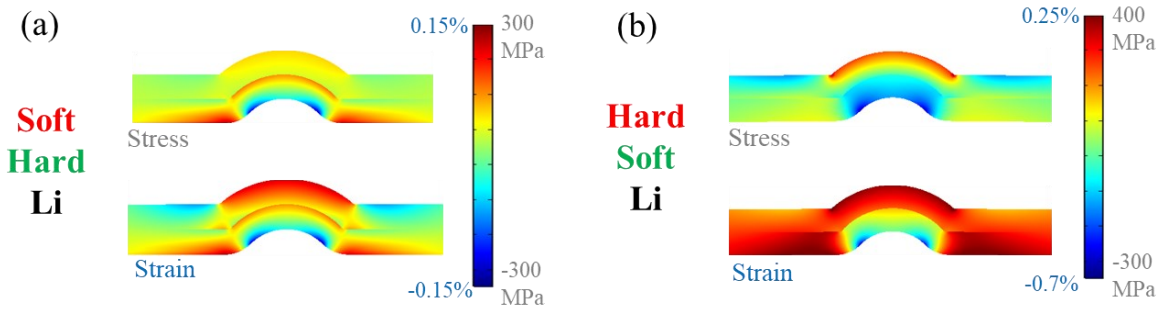

Figure 6-3 Stress and strain distribution in a dual layer hard Al_2O_3 and soft alucone with (a) soft/hard and (b) hard/soft sequences.

Nevertheless, the simulation in Figure 6-3 only considers a one combination of soft/hard layer. To further explore whether having the soft layer on the outside is the preferred configuration, additional parametric studies are performed by varying elastic moduli for soft and hard layers as Four different elastic moduli, E = 5, 25, 75, and 150 GPa, with a 50% ratio of hard layer thickness are considered. The maximum stress and strain, as well as the percent change in surface roughness at the final time step.

Figure 6-4 illustrates the relationship between % roughness change, effective elastic modulus and % fracture strain of the hard layer. The percentage of roughness change is presented in color scale, the yellowish color indicates poor performance, which can be due to either (i) SEI cracking as the fracture strain (which is materials property) is less than the maximum strain (derived from the simulation results), or (ii) SEI not being able to mechanically suppress Li dendrite. This is because we treat roughness change as similar to the case without the SEI when the SEI breaks, as it can no longer physically block Li dendrites. The blueish region represents good performance, where the surface roughness is reduced. The left side of the plot represents the Soft/Hard sequence, and the right side represents the Hard/Soft sequence. The flexibility requirement for the hard layer is lower when the layer sequence is Hard/Soft. For example, when comparing 75/150 and its counterpart 150/75, 75/150 requires at least 0.6% fracture strain, while 150/75 only needs 0.1%. This lower requirement for fracture strain implies that the deformation in the hard layer is small, making the hard layer materials more resilient and less likely to fracture. And this holds true for the rest of soft and hard layers combinations. The conclusion of this section agrees well with the previous experimental work [100], reporting that battery with Hard/Soft (Al_2O_3/alucone) SEI sequence has better electrochemical performance than its counterpart Soft/Hard (alucone/Al_2O_3) SEI.

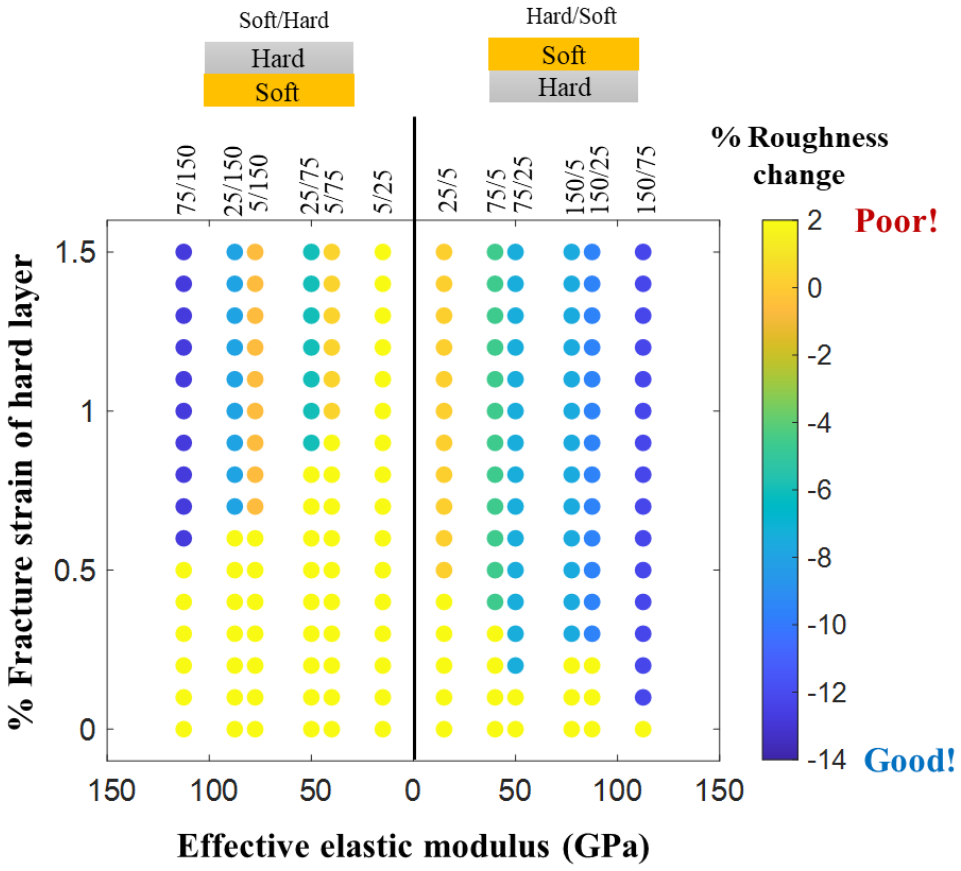

Figure 6-4 The plot of % roughness changes as a function of the effective elastic modulus and % fracture strain of the hard layer. The left side of the plot represents the Soft/Hard sequence, and the right side represents the Hard/Soft sequence. The numbers on the top indicate the elastic modulus of each layer, for instance, 75/150 refers to 75 GPa for the inner layer and 150 GPa for the outer layer, located on the left side, Soft/Hard region. Notably, the effective elastic modulus is identical for 75/150 and 150/75, and their data points are mirrored across the y-axis at x = 0 GPa.

6.3.4 A Design Map

To create a design map for a dual layer, more parametric studies must be carried out. Earlier, it is determined that the preferential sequence is Hard/Soft, and by following the experimental report, the total SEI thickness is assumed 20 nm for optimal performance. In this section, the hard layer is always an inner layer with an average elastic modulus of 150 GPa (typical for most inorganic thin-firm materials), and the total SEI thickness is 20 nm. High-throughput simulation is performed by varying the elastic modulus for soft material (E = 5,25,50, and 75 GPa), and the ratio of hard layer over the total thickness (R = 0.3, 0.4, 0.5, 0.6 and 0.7). The maximum

stress and strain, as well as the percent change in surface roughness, are recorded at the final time step.

Figure 6-5 presents design maps for a dual-layer solid electrolyte interphase (SEI) structure, where the z-axis represents the fracture strain for the hard and soft layers in Figures 32a and 32b, respectively. Figure 32b indicates that the requirement for the fracture strain of the soft layer to prevent rupture is approximately 0.35%, which is not a highly stringent requirement for soft materials as they are expected to possess high flexibility. Consequently, Figure 32a is more critical when suggesting the design as it pertains to the hard layer's ability to withstand the volume change.

As illustrated in Figure 6-5a, reducing the ratio of the hard layer decreases the critical fracture strain required for the hard layer. However, this results in a slight drop in Li dendrite suppression performance due to the reduction of the effective elastic modulus. Moreover, an increase in the elastic modulus of the soft layer not only reduces the required fracture strain of the hard layer, but also improves the Li suppression performance. Nevertheless, it is crucial to note that an increase in stiffness may lead to a decrease in flexibility. Therefore, it is recommended to double-check Figure 6-5b to verify whether the soft layer is susceptible to failure.

While this plot offers a preliminary approach to design the dual SEI layer based on mechanical considerations, it is important to verify the results experimentally, which remains as future work. In order to validate the design map, one can implement a dual SEI layer with Al_2O_3 and alucone as the hard and soft layer, respectively, and vary the thickness ratio (R = 0.3, 0.5, and 0.7). The resulting battery performance can then be compared with the prediction from the plot, which suggests that the performance of the battery follows this order: R= 0.3>0.5>0.7.

However, in this work, the simulations only consider a specific case with a fixed size of the Li perturbation and constant applied voltage, limiting the generalizability of the design map. Future simulations should vary the size of the perturbation and applied voltage to increase the map's generalizability. Additionally, simulations could be extended to account for inhomogeneity of SEI structures and their mechanical properties. Adhesion force between the SEI and Li metal surface should also be considered in stress distribution within the SEI layer to improve the physics in the simulations.

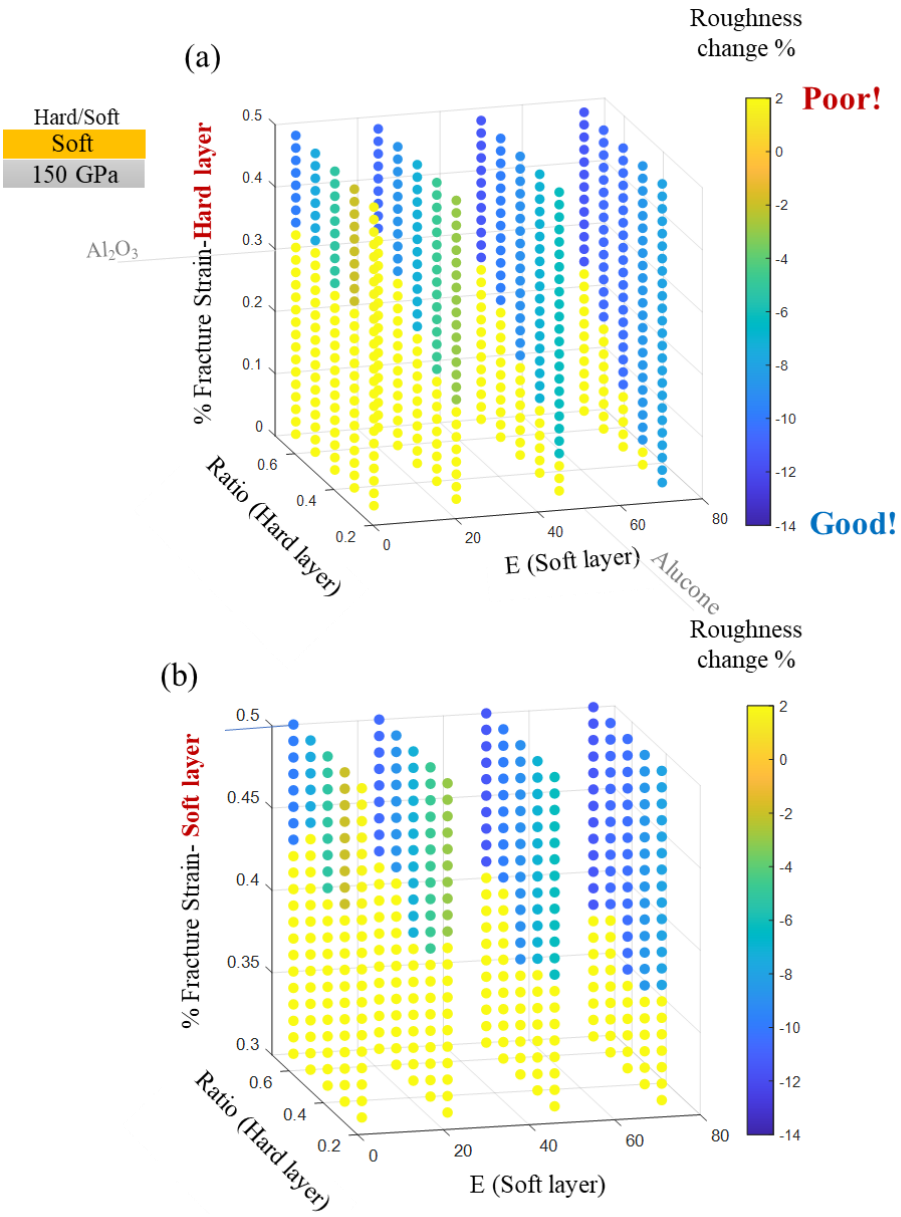

Figure 6-5 3D design maps for a dual-layer SEI structure. The inner layer is fixed as the hard layer with an average elastic modulus of 150 GPa, based on the typical value for most inorganic thin-film materials, to reduce the number of design parameters. The percentage change in roughness is plotted as a function of the elastic modulus of the soft layer, the ratio of the hard layer to the total thickness, and the % fracture strain for (a) the hard layer and (b) the soft layer.

6.4 Conclusion

The electro-chemo-mechanical phase-field model has been extended to predict the mechanical and electrochemical interaction between the SEI layer and the Li metal. The results reveal the mechanism of how the SEI layer mechanically suppresses the growth of Li nuclei. Compressive stress is generated near the tip of the perturbation due to the high curvature effect causing fast growth at the tip, and to satisfy the stress equilibrium equations, tensile stress is developed at the valley (or the base). The interfacial compressive stress impedes the rate at the tip, while the tensile stress accelerates the rate at the base; therefore, the resulting surface is more uniform.

Moreover, the variation of the mechanical properties of the SEI is studied. The simulations show that a hard SEI layer made of inorganic materials can effectively suppress the growth of Li dendrites due to its high stiffness. However, it is also prone to fracture. On the other hand, a soft SEI layer made of organic materials has high mechanical flexibility but does not perform well in suppressing Li dendrites. Therefore, it is recommended to use a combination of both soft and hard layers to achieve the ideal mechanical properties for the SEI layer.

In addition to single layer SEI design, the use of dual layer SEI, composed of soft and hard layers, has been investigated. The design of a dual layer SEI can be complex due to numerous design parameters. To reduce this complexity, a total thickness of 20 nm, which has been found to be optimal in experiments, was assumed. Results of the analysis and simulations suggest that the optimal sequence for the dual layer SEI is Hard/Soft. A design map is then developed to guide the selection of the ratio of the hard layer based on the mechanical properties of the soft and hard materials.

Chapter 7: Conclusion and Perspectives

This dissertation discusses (i) the development of a mechano-electro-chemical phase-field model and (ii) the use of this model to speed up the design process of dendrite-free Li batteries from structural and mechanics perspectives. The following three well-known Li dendrites techniques are examined in this work:

1. 3D host structure: The phase-field model highlights a successful design of the 3D host structure depends on uniform curvature. During charging, ultra-uniform electrode curvature generates the uniform local electric fields that evenly attract Li-ions to the electrode surface, resulting in an even current density distribution, and thus the uniform Li deposition. This concept of uniform curvature should be valid in any scenario, regardless of the types of 3D nanostructure and material composition, as long as the electrode surface is uniform at the nanoscale. Nanoengineering the electrode surface can be difficult, but TiO_2 nanotube arrays serve a good example to confirm this hypothesis. These nanotubes have high surface curvature, are highly-oriented, mechanically strong, and easy to fabricate. Electrochemical testing shows that the performance of a Li metal battery with a host structure of ultra-uniform surface, such as TiO2 nanotubes, is phenomenal.
2. Solid electrolyte: Solid electrolyte is considered a promising solution for preventing Li dendrite because of its high strength to mechanically suppress their growth. However, Li penetration is still observed even in a mechanically hard ceramics electrolyte. To explain and understand this phenomenon, the developed mechano-electro-chemical phase-field model is utilized to understand and explain this phenomenon. It was found that at the

microstructural defects such as grain boundary (GB), have inferior mechanical properties and thus provide a preferential growth path for Li penetration. In addition, these defects also tend to trap electrons, which can reduce Li-ions in the bulk electrolyte and generate isolated Li nuclei. Based on these findings, some suggestions for future experiments include (i) improving the mechanical properties of GB, (ii) introducing a chemical or physical system to block or eliminate dendrites in the GB, or (iii) reducing the number of defects as much as possible.

3. Artificial solid electrolyte interface (SEI): Simulation results demonstrate that a hard (inorganic) SEI layer can mechanically suppress Li dendrite growth due to its high stiffness but is susceptible to fracture. However, a soft (organic) SEI layer has high mechanical flexibility, but poor Li dendrite suppression performance. To achieve the ideal mechanical properties, a dual SEI layer, combining soft and hard layer is recommended. However, finding the best combination based on experiment trial-and-error for dual layers is not cost or time efficient. High-throughput simulation is performed to provide a rough design guideline for experiments. Nevertheless, this work is considered a prototype, serving to demonstrate the process by which the model can aid experiments. To effectively guide experiments, the model itself needs to be further developed to become more robust, and the case study presented here should also be expanded. Furthermore, there may be an opportunity to incorporate machine learning or data-driven model in the framework to reduce computation time and cost and provide further insight in guiding experiments.

References

[1] Y. Yang, S. Bremner, C. Menictas, and M. Kay, "Battery energy storage system size determination in renewable energy systems: A review," *Renew. Sustain. Energy Rev.*, vol. 91, pp. 109–125, 2018, doi: https://doi.org/10.1016/j.rser.2018.03.047.

[2] B. Leard, "Federal Climate Policy 104: The Transportationitle," *Explainer*, 2021. [Online]. Available: https://www.rff.org/publications/explainers/federal-climate-policy-104-the-transportation-sector/#:~:text=The transportation sector accounted for,of transportation emissions is uncertain. [Accessed: 02-Jul-2023].

[3] A. Masias, J. Marcicki, and W. A. Paxton, "Opportunities and Challenges of Lithium Ion Batteries in Automotive Applications," *ACS Energy Lett.*, vol. 6, no. 2, pp. 621–630, 2021, doi: 10.1021/acsenergylett.0c02584.

[4] "Goals for Advanced High-Performance Batteries for Electric Vehicle (EV) Applications," *United State Advanced Battery Consortium*, 2020. [Online]. Available: http://www.uscar.org/guest/article_view.php?articles_id=85.

[5] M. Winter, B. Barnett, and K. Xu, "Before Li Ion Batteries," *Chem. Rev.*, vol. 118, no. 23, pp. 11433–11456, 2018, doi: 10.1021/acs.chemrev.8b00422.

[6] P. Albertus, S. Babinec, S. Litzelman, and A. Newman, "Status and challenges in enabling the lithium metal electrode for high-energy and low-cost rechargeable batteries," *Nat. Energy*, vol. 3, no. 1, pp. 16–21, 2018, doi: 10.1038/s41560-017-0047-2.

[7] J. Bausch, "What are dendrites, and why do they cause fires in lithium batteries?," *Electronic Products*, 2016. [Online]. Available: https://www.electronicproducts.com/what-are-dendrites-and-why-do-they-cause-fires-in-lithium-batteries/. [Accessed: 12-Jun-2022].

[8] M. N.Eisler, "The History of Lithium Ion Batteries Is Explosive," *Future Tense*, 2016. [Online]. Available: https://slate.com/technology/2016/09/the-explosive-history-of-lithium-ion-batteries.html. [Accessed: 12-Jun-2022].

[9] B. Berman, "Battery Experts Provide Deeper Explanations for Chevy Bolt Fires," *Autoweek*, 2021. [Online]. Available: https://www.autoweek.com/news/a38252667/battery-experts-explain-chevy-bolt-fires/. [Accessed: 12-Jun-2022].

[10] X. B. Cheng, R. Zhang, C. Z. Zhao, and Q. Zhang, “Toward safe lithium metal anode in rechargeable batteries: a review,” *Chem. Rev.*, vol. 117, 2017, doi: 10.1021/acs.chemrev.7b00115.

[11] J. N. Chazalviel, “Electrochemical aspects of the generation of ramified metallic electrodeposits,” *Phys. Rev. A*, vol. 42, no. 12, pp. 7355–7367, 1990, doi: 10.1103/PhysRevA.42.7355.

[12] C. Brissot, M. Rosso, J. N. Chazalviel, and S. Lascaud, “Dendritic growth mechanisms in lithium/polymer cells,” *J. Power Sources*, vol. 81, pp. 925–929, 1999, doi: 10.1016/S0378-7753(98)00242-0.

[13] C. Brissot, M. Rosso, J. -N. Chazalviel, and S. Lascaud, “In Situ Concentration Cartography in the Neighborhood of Dendrites Growing in Lithium/Polymer-Electrolyte/Lithium Cells,” *J. Electrochem. Soc.*, vol. 146, no. 12, pp. 4393–4400, 1999, doi: 10.1149/1.1392649.

[14] H. Liu *et al.*, “Recent advances in understanding dendrite growth on alkali metal anodes,” *EnergyChem*, vol. 1, no. 1, p. 100003, 2019, doi: 10.1016/j.enchem.2019.100003.

[15] J. I. Yamaki, S. I. Tobishima, K. Hayashi, K. Saito, Y. Nemoto, and M. Arakawa, “A consideration of the morphology of electrochemically deposited lithium in an organic electrolyte,” *J. Power Sources*, vol. 74, no. 2, pp. 219–227, 1998, doi: 10.1016/S0378-7753(98)00067-6.

[16] X. Wang *et al.*, “Stress-driven lithium dendrite growth mechanism and dendrite mitigation by electroplating on soft substrates,” *Nat. Energy*, vol. 3, no. 3, pp. 227–235, 2018, doi: 10.1038/s41560-018-0104-5.

[17] C. Monroe and J. Newman, “The Impact of Elastic Deformation on Deposition Kinetics at Lithium/Polymer Interfaces,” *J. Electrochem. Soc.*, vol. 152, no. 2, p. A396, 2005, doi: 10.1149/1.1850854.

[18] P. Barai, K. Higa, and V. Srinivasan, “Effect of Initial State of Lithium on the Propensity for Dendrite Formation: A Theoretical Study,” *J. Electrochem. Soc.*, vol. 164, no. 2, pp. A180–A189, 2017, doi: 10.1149/2.0661702jes.

[19] T. Foroozan, S. Sharifi-Asl, and R. Shahbazian-Yassar, “Mechanistic understanding of Li dendrites growth by in- situ/operando imaging techniques,” *J. Power Sources*, vol. 461, no. January, 2020, doi: 10.1016/j.jpowsour.2020.228135.

[20] K. N. Wood *et al.*, “Dendrites and pits: Untangling the complex behavior of lithium metal anodes through operando video microscopy,” *ACS Cent. Sci.*, vol. 2, no. 11, pp. 790–801, 2016, doi: 10.1021/acscentsci.6b00260.

[21] J. Steiger, D. Kramer, and R. Mönig, “Microscopic observations of the formation, growth and shrinkage of lithium moss during electrodeposition and dissolution,” *Electrochim. Acta*, vol. 136, pp. 529–536, 2014, doi: 10.1016/j.electacta.2014.05.120.

[22] L. Kong, Y. Xing, and M. G. Pecht, “In-Situ Observations of Lithium Dendrite Growth,” *IEEE Access*, vol. 6, pp. 8387–8393, 2018, doi: 10.1109/ACCESS.2018.2805281.

[23] P. Bai, J. Li, F. R. Brushett, and M. Z. Bazant, “Transition of lithium growth mechanisms in liquid electrolytes,” *Energy Environ. Sci.*, vol. 9, no. 10, pp. 3221–3229, 2016, doi: 10.1039/c6ee01674j.

[24] B. L. Mehdi *et al.*, “Observation and quantification of nanoscale processes in lithium batteries by operando electrochemical (S)TEM,” *Nano Lett.*, vol. 15, no. 3, pp. 2168–2173, 2015, doi: 10.1021/acs.nanolett.5b00175.

[25] Y. Sun *et al.*, “Boosting the Optimization of Lithium Metal Batteries by Molecular Dynamics Simulations: A Perspective,” *Adv. Energy Mater.*, vol. 10, no. 41, 2020, doi: 10.1002/aenm.202002373.

[26] L. Li *et al.*, “Self-heating-induced healing of lithium dendrites,” 2018.

[27] A. Aryanfar, T. Cheng, A. J. Colussi, B. V. Merinov, W. A. Goddard, and M. R. Hoffmann, “Annealing kinetics of electrodeposited lithium dendrites,” *J. Chem. Phys.*, vol. 143, no. 13, pp. 1–6, 2015, doi: 10.1063/1.4930014.

[28] N. Cheimarios, D. To, G. Kokkoris, G. Memos, and A. G. Boudouvis, “Monte Carlo and Kinetic Monte Carlo Models for Deposition Processes: A Review of Recent Works,” *Front. Phys.*, vol. 9, no. April, 2021, doi: 10.3389/fphy.2021.631918.

[29] A. Aryanfar, D. Brooks, B. V. Merinov, W. A. Goddard, A. J. Colussi, and M. R. Hoffmann, “Dynamics of lithium dendrite growth and inhibition: Pulse charging experiments and monte carlo calculations,” *J. Phys. Chem. Lett.*, vol. 5, no. 10, pp. 1721–1726, 2014, doi: 10.1021/jz500207a.

[30] A. Aryanfar, D. J. Brooks, A. J. Colussi, B. V. Merinov, W. A. Goddard, and M. R. Hoffmann, “Thermal relaxation of lithium dendrites,” *Phys. Chem. Chem. Phys.*, vol. 17, no. 12, pp. 8000–8005, 2015, doi: 10.1039/c4cp05786d.

[31] B. S. Vishnugopi, F. Hao, A. Verma, and P. P. Mukherjee, “Double-Edged Effect of Temperature on Lithium Dendrites,” *ACS Appl. Mater. Interfaces*, vol. 12, no. 21, pp. 23931–23938, 2020, doi: 10.1021/acsami.0c04355.

[32] J. E. Guyer, W. J. Boettinger, J. A. Warren, and G. B. McFadden, “Phase field modeling of electrochemistry. I. Equilibrium,” *Phys. Rev. E - Stat. Nonlinear, Soft Matter Phys.*, vol. 69, no. 2 1, pp. 1–13, 2004, doi: 10.1103/PhysRevE.69.021603.

[33] L. Liang, Y. Qi, F. Xue, S. Bhattacharya, S. J. Harris, and L. Q. Chen, “Nonlinear phase-field model for electrode-electrolyte interface evolution,” *Phys. Rev. E - Stat. Nonlinear, Soft Matter Phys.*, vol. 86, no. 5, pp. 1–5, 2012, doi: 10.1103/PhysRevE.86.051609.

[34] L. Chen *et al.*, “Modulation of dendritic patterns during electrodeposition: A nonlinear phase-field model,” *J. Power Sources*, vol. 300, pp. 376–385, 2015, doi:

10.1016/j.jpowsour.2015.09.055.

[35] V. Yurkiv, T. Foroozan, A. Ramasubramanian, R. Shahbazian-Yassar, and F. Mashayek, “Phase-field modeling of solid electrolyte interface (SEI) influence on Li dendritic behavior,” *Electrochim. Acta*, vol. 265, pp. 609–619, 2018, doi: 10.1016/j.electacta.2018.01.212.

[36] M. Wang, J. B. Wolfenstine, and J. Sakamoto, “Temperature dependent flux balance of the Li/Li7La3Zr2O12 interface,” *Electrochim. Acta*, vol. 296, pp. 842–847, 2019, doi: 10.1016/j.electacta.2018.11.034.

[37] Z. Hong and V. Viswanathan, “Prospect of Thermal Shock Induced Healing of Lithium Dendrite,” *ACS Energy Lett.*, vol. 4, no. 5, pp. 1012–1019, 2019, doi: 10.1021/acsenergylett.9b00433.

[38] W. Mu, X. Liu, Z. Wen, and L. Liu, “Numerical simulation of the factors affecting the growth of lithium dendrites,” *J. Energy Storage*, vol. 26, no. September, p. 100921, 2019, doi: 10.1016/j.est.2019.100921.

[39] R. Zhang, X. Shen, X. B. Cheng, and Q. Zhang, “The dendrite growth in 3D structured lithium metal anodes: Electron or ion transfer limitation?,” *Energy Storage Mater.*, vol. 23, no. February, pp. 556–565, 2019, doi: 10.1016/j.ensm.2019.03.029.

[40] R. Zhang *et al.*, “Dead lithium formation in lithium metal batteries: A phase field model,” *J. Energy Chem.*, vol. 71, pp. 29–35, 2022, doi: https://doi.org/10.1016/j.jechem.2021.12.020.

[41] Q. Wang, G. Zhang, Y. Li, Z. Hong, D. Wang, and S. Shi, “Application of phase-field method in rechargeable batteries,” *npj Comput. Mater.*, vol. 6, no. 1, pp. 1–8, 2020, doi: 10.1038/s41524-020-00445-w.

[42] S. Sarkar and W. Aquino, “Changes in electrodic reaction rates due to elastic stress and stress-induced surface patterns,” *Electrochim. Acta*, vol. 111, pp. 814–822, 2013, doi: 10.1016/j.electacta.2013.08.085.

[43] H. Ma *et al.*, “Eigenstress model for electrochemistry of solid surfaces,” *Sci. Rep.*, vol. 6, no. June, pp. 1–11, 2016, doi: 10.1038/srep26897.

[44] K. Tantratian, H. Yan, K. Ellwood, E. T. Harrison, and L. Chen, “Unraveling the Li Penetration Mechanism in Polycrystalline Solid Electrolytes,” *Adv. Energy Mater.*, vol. 11, no. 13, pp. 1–8, 2021, doi: 10.1002/aenm.202003417.

[45] H. Kim, G. Jeong, Y. U. Kim, J. H. Kim, C. M. Park, and H. J. Sohn, “Metallic anodes for next generation secondary batteries,” *Chem. Soc. Rev.*, vol. 42, no. 23, pp. 9011–9034, 2013, doi: 10.1039/c3cs60177c.

[46] M. Armand and J.-M. Tarascon, “Building better batteries,” *Nature*, vol. 451, no. 7179, pp. 652–657, 2008, doi: 10.1038/451652a.

[47] T. Ohzuku, “Formation of Lithium-Graphite Intercalation Compounds in Nonaqueous Electrolytes and Their Application as a Negative Electrode for a Lithium Ion (Shuttlecock) Cell,” *J. Electrochem. Soc.*, vol. 140, no. 9, p. 2490, 2006, doi: 10.1149/1.2220849.

[48] D. Cao *et al.*, “3D Printed High-Performance Lithium Metal Microbatteries Enabled by Nanocellulose,” *Adv. Mater.*, vol. 31, no. 14, pp. 1–10, 2019, doi: 10.1002/adma.201807313.

[49] S.-S. Chi, X.-G. Qi, Y.-S. Hu, and L.-Z. Fan, “3D Flexible Carbon Felt Host for Highly Stable Sodium Metal Anodes,” *Adv. Energy Mater.*, vol. 8, no. 15, p. 1702764, 2018.

[50] S. Sen Chi, Y. Liu, W. L. Song, L. Z. Fan, and Q. Zhang, “Prestoring Lithium into Stable 3D Nickel Foam Host as Dendrite-Free Lithium Metal Anode,” *Adv. Funct. Mater.*, vol. 27, no. 24, pp. 1–10, 2017, doi: 10.1002/adfm.201700348.

[51] X. Y. Yue *et al.*, “CoO nanofiber decorated nickel foams as lithium dendrite suppressing host skeletons for high energy lithium metal batteries,” *Energy Storage Mater.*, vol. 14, no. May, pp. 335–344, 2018, doi: 10.1016/j.ensm.2018.05.017.

[52] S. H. Wang *et al.*, “Stable Li Metal Anodes via Regulating Lithium Plating/Stripping in Vertically Aligned Microchannels,” *Adv. Mater.*, vol. 29, no. 40, pp. 1–8, 2017, doi: 10.1002/adma.201703729.

[53] G. Yoon, S. Moon, G. Ceder, and K. Kang, “Deposition and Stripping Behavior of Lithium Metal in Electrochemical System: Continuum Mechanics Study,” *Chem. Mater.*, vol. 30, no. 19, pp. 6769–6776, 2018, doi: 10.1021/acs.chemmater.8b02623.

[54] L. Li, S. Li, and Y. Lu, “Suppression of dendritic lithium growth in lithium metal-based batteries,” *Chem. Commun.*, vol. 54, no. 50, pp. 6648–6661, 2018, doi: 10.1039/c8cc02280a.

[55] K. Nishikawa, T. Mori, T. Nishida, Y. Fukunaka, M. Rosso, and T. Homma, “In Situ Observation of Dendrite Growth of Electrodeposited Li Metal,” *J. Electrochem. Soc.*, vol. 157, no. 11, p. A1212, 2010, doi: 10.1149/1.3486468.

[56] M. D. Tikekar, L. A. Archer, and D. L. Koch, “Stabilizing electrodeposition in elastic solid electrolytes containing immobilized anions,” *Sci. Adv.*, vol. 2, no. 7, 2016, doi: 10.1126/sciadv.1600320.

[57] K. Tantratian *et al.*, “Stable Li Metal Anode Enabled by Space Confinement and Uniform Curvature through Lithiophilic Nanotube Arrays,” *Adv. Energy Mater.*, vol. 10, no. 5, pp. 1–9, 2020, doi: 10.1002/aenm.201902819.

[58] Y. Zhang *et al.*, “High-capacity, low-tortuosity, and channel-guided lithium metal anode,” *Proc. Natl. Acad. Sci.*, vol. 114, no. 14, pp. 3584–3589, 2017, doi: 10.1073/pnas.1618871114.

[59] F. Zheng, M. Kotobuki, S. Song, M. O. Lai, and L. Lu, “Review on solid electrolytes for all-solid-state lithium-ion batteries,” *J. Power Sources*, vol. 389, no. February, pp. 198–213, 2018, doi: 10.1016/j.jpowsour.2018.04.022.

[60] L. Fan, S. Wei, S. Li, Q. Li, and Y. Lu, “Recent Progress of the Solid-State Electrolytes for High-Energy Metal-Based Batteries,” *Adv. Energy Mater.*, vol. 8, no. 11, pp. 1–31, 2018, doi: 10.1002/aenm.201702657.

[61] F. Zhang *et al.*, “A review of mechanics-related material damages in all-solid-state batteries: Mechanisms, performance impacts and mitigation strategies,” *Nano Energy*, vol. 70, no. November 2019, p. 104545, 2020, doi: 10.1016/j.nanoen.2020.104545.

[62] D. Cao, X. Sun, Q. Li, A. Natan, P. Xiang, and H. Zhu, “Lithium Dendrite in All-Solid-State Batteries: Growth Mechanisms, Suppression Strategies, and Characterizations,” *Matter*, vol. 3, no. 1, pp. 57–94, 2020, doi: 10.1016/j.matt.2020.03.015.

[63] E. J. Cheng, A. Sharafi, and J. Sakamoto, “Intergranular Li metal propagation through polycrystalline Li6.25Al0.25La3Zr2O12 ceramic electrolyte,” *Electrochim. Acta*, vol. 223, pp. 85–91, 2017, doi: 10.1016/j.electacta.2016.12.018.

[64] S. Ozkan, G. Cha, A. Mazare, and P. Schmuki, “TiO<inf>2</inf>nanotubes with different spacing, Fe<inf>2</inf>O<inf>3</inf>decoration and their evaluation for Li-ion battery application,” *Nanotechnology*, vol. 29, no. 19, 2018, doi: 10.1088/1361-6528/aab062.

[65] E. Kazyak *et al.*, “Li Penetration in Ceramic Solid Electrolytes: Operando Microscopy Analysis of Morphology, Propagation, and Reversibility,” *Matter*, vol. 2, no. 4, pp. 1025–1048, 2020, doi: https://doi.org/10.1016/j.matt.2020.02.008.

[66] H. Ye, S. Xin, Y. X. Yin, and Y. G. Guo, “Advanced porous carbon materials for high-efficient lithium metal anodes,” *Adv. Energy Mater.*, vol. 7, no. 23, pp. 1–9, 2017, doi: 10.1002/aenm.201700530.

[67] K. B. Hatzell *et al.*, “Challenges in Lithium Metal Anodes for Solid-State Batteries,” *ACS Energy Lett.*, vol. 5, no. 3, pp. 922–934, 2020, doi: 10.1021/acsenergylett.9b02668.

[68] P. Barai, A. T. Ngo, B. Narayanan, K. Higa, L. A. Curtiss, and V. Srinivasan, “The Role of Local Inhomogeneities on Dendrite Growth in LLZO-Based Solid Electrolytes,” *J. Electrochem. Soc.*, vol. 167, no. 10, p. 100537, 2020, doi: 10.1149/1945-7111/ab9b08.

[69] P. Barai, K. Higa, A. T. Ngo, L. A. Curtiss, and V. Srinivasan, “Mechanical Stress Induced Current Focusing and Fracture in Grain Boundaries,” *J. Electrochem. Soc.*, vol. 166, no. 10, pp. A1752–A1762, 2019, doi: 10.1149/2.0321910jes.

[70] G. Bucci and J. Christensen, “Modeling of lithium electrodeposition at the lithium/ceramic electrolyte interface: The role of interfacial resistance and surface defects,” *J. Power Sources*, vol. 441, no. September, p. 227186, 2019, doi: 10.1016/j.jpowsour.2019.227186.

[71] A. Mistry and P. P. Mukherjee, “Molar Volume Mismatch: A Malefactor for Irregular

Metallic Electrodeposition with Solid Electrolytes," *J. Electrochem. Soc.*, vol. 167, no. 8, p. 082510, 2020, doi: 10.1149/1945-7111/ab8ecd.

[72] S. Yu and D. J. Siegel, "Grain Boundary Softening: A Potential Mechanism for Lithium Metal Penetration through Stiff Solid Electrolytes," *ACS Appl. Mater. Interfaces*, vol. 10, no. 44, pp. 38151–38158, 2018, doi: 10.1021/acsami.8b17223.

[73] F. Han *et al.*, "High electronic conductivity as the origin of lithium dendrite formation within solid electrolytes," *Nat. Energy*, vol. 4, no. 3, pp. 187–196, 2019, doi: 10.1038/s41560-018-0312-z.

[74] H. K. Tian, Z. Liu, Y. Ji, L. Q. Chen, and Y. Qi, "Interfacial Electronic Properties Dictate Li Dendrite Growth in Solid Electrolytes," *Chem. Mater.*, vol. 31, no. 18, pp. 7351–7359, 2019, doi: 10.1021/acs.chemmater.9b01967.

[75] H. K. Tian, B. Xu, and Y. Qi, "Computational study of lithium nucleation tendency in Li7La3Zr2O12 (LLZO) and rational design of interlayer materials to prevent lithium dendrites," *J. Power Sources*, vol. 392, no. March, pp. 79–86, 2018, doi: 10.1016/j.jpowsour.2018.04.098.

[76] Y. Song *et al.*, "Revealing the Short-Circuiting Mechanism of Garnet-Based Solid-State Electrolyte," *Adv. Energy Mater.*, vol. 9, no. 21, 2019, doi: 10.1002/aenm.201900671.

[77] X. Zhang, Q. J. Wang, K. L. Harrison, S. A. Roberts, and S. J. Harris, "Pressure-Driven Interface Evolution in Solid-State Lithium Metal Batteries," *Cell Reports Phys. Sci.*, vol. 1, no. 2, p. 100012, 2020, doi: 10.1016/j.xcrp.2019.100012.

[78] P. Wang, W. Qu, W. L. Song, H. Chen, R. Chen, and D. Fang, "Electro–Chemo–Mechanical Issues at the Interfaces in Solid-State Lithium Metal Batteries," *Adv. Funct. Mater.*, vol. 29, no. 27, pp. 1–29, 2019, doi: 10.1002/adfm.201900950.

[79] Y. Chen *et al.*, "Li metal deposition and stripping in a solid-state battery via Coble creep," *Nature*, vol. 578, no. 7794, pp. 251–255, 2020, doi: 10.1038/s41586-020-1972-y.

[80] W. S. LePage *et al.*, "Lithium Mechanics: Roles of Strain Rate and Temperature and Implications for Lithium Metal Batteries," *J. Electrochem. Soc.*, vol. 166, no. 2, pp. A89–A97, 2019, doi: 10.1149/2.0221902jes.

[81] X. Zhang, Q. Xiang, S. Tang, A. Wang, X. Liu, and J. Luo, "Long Cycling Life Solid-State Li Metal Batteries with Stress Self-Adapted Li/Garnet Interface," *Nano Lett.*, vol. 20, no. 4, pp. 2871–2878, 2020, doi: 10.1021/acs.nanolett.0c00693.

[82] Q. Tu, L. Barroso-Luque, T. Shi, and G. Ceder, "Electrodeposition and Mechanical Stability at Lithium-Solid Electrolyte Interface during Plating in Solid-State Batteries," *Cell Reports Phys. Sci.*, vol. 1, no. 7, p. 100106, 2020, doi: 10.1016/j.xcrp.2020.100106.

[83] A. Sharafi, H. M. Meyer, J. Nanda, J. Wolfenstine, and J. Sakamoto, "Characterizing the Li-Li7La3Zr2O12 interface stability and kinetics as a function of temperature and current

density," *J. Power Sources*, vol. 302, pp. 135–139, 2016, doi: 10.1016/j.jpowsour.2015.10.053.

[84] W. L. Huang *et al.*, "Can we find solution to eliminate Li penetration through solid garnet electrolytes?," *Mater. Today Nano*, vol. 10, 2020, doi: 10.1016/j.mtnano.2020.100075.

[85] L. Porz *et al.*, "Mechanism of Lithium Metal Penetration through Inorganic Solid Electrolytes," *Adv. Energy Mater.*, vol. 7, no. 20, pp. 1–12, 2017, doi: 10.1002/aenm.201701003.

[86] X. B. Cheng, R. Zhang, C. Z. Zhao, F. Wei, J. G. Zhang, and Q. Zhang, "A review of solid electrolyte interphases on lithium metal anode," *Adv. Sci.*, vol. 3, no. 3, pp. 1–20, 2015, doi: 10.1002/advs.201500213.

[87] H. Wu, H. Jia, C. Wang, J. G. Zhang, and W. Xu, "Recent Progress in Understanding Solid Electrolyte Interphase on Lithium Metal Anodes," *Adv. Energy Mater.*, vol. 11, no. 5, pp. 1–35, 2021, doi: 10.1002/aenm.202003092.

[88] E. Peled, D. Golodnitsky, and G. Ardel, "Advanced Model for Solid Electrolyte Interphase Electrodes in Liquid and Polymer Electrolytes," *J. Electrochem. Soc.*, vol. 144, no. 8, pp. L208–L210, 1997, doi: 10.1149/1.1837858.

[89] P. Lu and S. J. Harris, "Lithium transport within the solid electrolyte interphase," *Electrochem. commun.*, vol. 13, no. 10, pp. 1035–1037, 2011, doi: 10.1016/j.elecom.2011.06.026.

[90] M. Wu, Y. Li, X. Liu, S. Yang, J. Ma, and S. Dou, "Perspective on solid-electrolyte interphase regulation for lithium metal batteries," *SmartMat*, vol. 2, no. 1, pp. 5–11, 2021, doi: 10.1002/smm2.1015.

[91] C. Yan *et al.*, "An Armored Mixed Conductor Interphase on a Dendrite-Free Lithium-Metal Anode," *Adv. Mater.*, vol. 30, no. 45, pp. 1–9, 2018, doi: 10.1002/adma.201804461.

[92] Z. Liu, Y. Qi, Y. X. Lin, L. Chen, P. Lu, and L. Q. Chen, "Interfacial Study on Solid Electrolyte Interphase at Li Metal Anode: Implication for Li Dendrite Growth," *J. Electrochem. Soc.*, vol. 163, no. 3, pp. A592–A598, 2016, doi: 10.1149/2.0151605jes.

[93] Y. Wang and F. Hao, "Interactions Between Solid Electrolyte Interphase and Lithium Dendrite," *J. Electrochem. Energy Convers. Storage*, vol. 19, no. 4, pp. 1–19, 2022, doi: 10.1115/1.4054339.

[94] Y. Gao *et al.*, "Unraveling the mechanical origin of stable solid electrolyte interphase," *Joule*, vol. 5, no. 7, pp. 1860–1872, 2021, doi: 10.1016/j.joule.2021.05.015.

[95] Q. Zhao, S. Stalin, and L. A. Archer, "Stabilizing metal battery anodes through the design of solid electrolyte interphases," *Joule*, vol. 5, no. 5, pp. 1119–1142, 2021, doi: 10.1016/j.joule.2021.03.024.

[96] C.-Y. Tang and S. J. Dillon, “In Situ Scanning Electron Microscopy Characterization of the Mechanism for Li Dendrite Growth,” *J. Electrochem. Soc.*, vol. 163, no. 8, pp. A1660–A1665, 2016, doi: 10.1149/2.0891608jes.

[97] X. Shen, R. Zhang, X. Chen, X. B. Cheng, X. Li, and Q. Zhang, “The Failure of Solid Electrolyte Interphase on Li Metal Anode: Structural Uniformity or Mechanical Strength?,” *Adv. Energy Mater.*, vol. 10, no. 10, pp. 1–8, 2020, doi: 10.1002/aenm.201903645.

[98] F. Hao, A. Verma, and P. P. Mukherjee, “Mechanistic insight into dendrite-SEI interactions for lithium metal electrodes,” *J. Mater. Chem. A*, vol. 6, no. 40, pp. 19664–19671, 2018, doi: 10.1039/c8ta07997h.

[99] W. Cao *et al.*, “Organic-inorganic composite SEI for a stable Li metal anode by in-situ polymerization,” *Nano Energy*, vol. 95, no. January, p. 106983, 2022, doi: 10.1016/j.nanoen.2022.106983.

[100] Y. Zhao *et al.*, “Natural SEI-Inspired Dual-Protective Layers via Atomic/Molecular Layer Deposition for Long-Life Metallic Lithium Anode,” *Matter*, vol. 1, no. 5, pp. 1215–1231, 2019, doi: 10.1016/j.matt.2019.06.020.

[101] H. Liu *et al.*, “Controlling Dendrite Growth in Solid-State Electrolytes,” *ACS Energy Lett.*, vol. 5, no. 3, pp. 833–843, 2020, doi: 10.1021/acsenergylett.9b02660.

[102] J. Wang *et al.*, “In Situ Self-Assembly of Ordered Organic/Inorganic Dual-Layered Interphase for Achieving Long-Life Dendrite-Free Li Metal Anodes in LiFSI-Based Electrolyte,” *Adv. Funct. Mater.*, vol. 31, no. 7, pp. 1–10, 2021, doi: 10.1002/adfm.202007434.

[103] C. Yan *et al.*, “Dual-Layered Film Protected Lithium Metal Anode to Enable Dendrite-Free Lithium Deposition,” *Adv. Mater.*, vol. 30, no. 25, pp. 1–8, 2018, doi: 10.1002/adma.201707629.

[104] E. Jin *et al.*, “Ionic Conductive and Highly-Stable Interface for Alkali Metal Anodes,” *Small*, vol. 18, no. 33, pp. 1–9, 2022, doi: 10.1002/smll.202203045.